Is the near-spherical shape the ”new black” for smoke?

Anna Gialitaki, Alexandra Tsekeri, Vassilis Amiridis, Romain Ceolato, Lucas Paulien, Anna Kampouri, Antonis Gkikas, Stavros Solomos, Eleni Marinou, Moritz Haarig, et al.

To cite this version:

Anna Gialitaki, Alexandra Tsekeri, Vassilis Amiridis, Romain Ceolato, Lucas Paulien, et al.. Is the near-spherical shape the ”new black” for smoke?. Atmospheric Chemistry and Physics, 2020, 20 (22), pp.14005-14021. 10.5194/acp-2020-22 . hal-02776682v2

HAL Id: hal-02776682
https://hal.science/hal-02776682v2

Atmos. Chem. Phys., 20, 14005–14021, 2020
https://doi.org/10.5194/acp-20-14005-2020

Atmospheric Chemistry and Physics
Open Access

Is the near-spherical shape the "new black" for smoke?

Anna Gialitaki[1,2], Alexandra Tsekeri[1], Vassilis Amiridis[1], Romain Ceolato[3], Lucas Paulien[3], Anna Kampouri[1,9], Antonis Gkikas[1], Stavros Solomos[4,1], Eleni Marinou[5,1], Moritz Haarig[6], Holger Baars[6], Albert Ansmann[6], Tatyana Lapyonok[7], Anton Lopatin[8], Oleg Dubovik[7], Silke Groß[5], Martin Wirth[5], Maria Tsichla[1,10], Ioanna Tsikoudi[1,11], and Dimitris Balis[2]

[1]National Observatory of Athens/IAASARS, Athens, Greece
[2]Laboratory of Atmospheric Physics, Physics Department, Aristotle University of Thessaloniki, Thessaloniki, Greece
[3]ONERA, The French Aerospace Lab, Toulouse, France
[4]Research Centre for Atmospheric Physics and Climatology, Academy of Athens, Athens, Greece
[5]Institute of Atmospheric Physics, German Aerospace Center (DLR), Oberpfaffenhofen, Germany
[6]Leibniz Institute for Tropospheric Research (TROPOS), Leipzig, Germany
[7]Laboratoire d'Optique Atmosphérique, CNRS/Université Lille, Villeneuve-d'Ascq, France
[8]GRASP-SAS, Villeneuve-d'Ascq, France
[9]Department of Meteorology and Climatology, School of Geology, Aristotle University of Thessaloniki, Thessaloniki, Greece
[10]Environmental Chemical Processes Laboratory, Department of Chemistry, University of Crete, Crete, Greece
[11]Department of Environmental Physics and Meteorology, University of Athens, Athens, Greece

Correspondence: Anna Gialitaki (togialitaki@noa.gr)

Received: 11 January 2020 – Discussion started: 19 February 2020
Revised: 27 August 2020 – Accepted: 14 September 2020 – Published: 19 November 2020

Abstract. We examine the capability of near-spherical-shaped particles to reproduce the triple-wavelength particle linear depolarization ratio (PLDR) and lidar ratio (LR) values measured over Europe for stratospheric smoke originating from Canadian wildfires. The smoke layers were detected both in the troposphere and the stratosphere, though in the latter case the particles presented PLDR values of almost 18 % at 532 nm as well as a strong spectral dependence from the UV to the near-IR wavelength. Although recent simulation studies of rather complicated smoke particle morphologies have shown that heavily coated smoke aggregates can produce large PLDR, herein we propose a much simpler model of compact near-spherical smoke particles. This assumption allows for the reproduction of the observed intensive optical properties of stratospheric smoke, as well as their spectral dependence. We further examine whether an extension of the current Aerosol Robotic Network (AERONET) scattering model to include the near-spherical shapes could be of benefit to the AERONET retrieval for stratospheric smoke cases associated with enhanced PLDR. Results of our study illustrate the fact that triple-wavelength PLDR and LR lidar measurements can provide us with additional insight when it comes to particle characterization.

---

1 Introduction

Particles originating from biomass burning activities are known to have a significant effect on radiation and climate (Kaufman et al., 2002). The factors affecting the optical properties of smoke are mainly the black carbon fraction and the impact of the ageing processes (Amiridis et al., 2009). Various findings from field measurements suggest that the smoke particles' surface may serve as highly effective cloud nuclei (Ackerman, 2000; Hoose and Möhler, 2012; Koch and Del Genio, 2010; Marinou et al., 2019; Nichman et al., 2019), modifying cloud properties and lifetime and thus indirectly affecting the radiative budget. Their various impacts also depend on their lifetime, since they tend to alternate their properties, i.e. become less absorbing or more hydrophilic due to atmospheric processes (Amiridis et al., 2009; Adachi and Buseck, 2011).

Smoke particles in the atmosphere can be identified with lidar measurements which provide valuable information on the optical properties of aerosols, such as the depolarization of the backscattered light in terms of the particle linear depolarization ratio (PLDR). Spherical particles do not depolarize the incident radiation; hence, the PLDR can be used to derive information on morphologically complex particles such as smoke. Fresh smoke tends to form fluffy, mostly hydrophobic aggregates composed of many small single monomers. As the particles age in the atmosphere, this aggregate structure collapse; the particles become more hydrophilic and are frequently found covered by cells composed of water-soluble components such as sulfates or organic materials (Worringen et al., 2008; Wu et al., 2016). Due to the aforementioned processes, the PLDR of smoke particles may present a large variability related to the age of the particles (Baars et al., 2019), the presence of other aerosol types found inside the smoke layers (Tesche et al., 2009; Groß et al., 2011, 2013) or even the particle water uptake due to different humidity conditions (Cheng et al., 2014). These processes alter smoke particle shape, size and composition, resulting in PLDR values that may vary from 2 % to 10 % at 532 nm for aged and fresh smoke. These values can be even lower/higher in cases of mixtures with low/high depolarizing components, respectively (i.e. marine/dust particles) Müller et al. (2005) carried out an extensive study on the optical properties and the effect of atmospheric ageing of long-range-transported smoke from Siberia and Canada and found that PLDR at 532 nm did not exceed 1 %–3 % for 10 d old plumes. This is comparable to findings by Nicolae et al. (2013), showing that smoke plumes up to 4 d old present PLDR values of almost 4 % at 532 nm. Moreover, measurements conducted in South Africa (Giannakaki et al., 2016) showed that for pure smoke the PLDR values at 355 nm are less than 6 %. On the other hand, smoke PLDR has been found to reach values up to 12 %–14 % at 532 nm if significant concentrations of highly depolarizing components (i.e. soil or dust particles) exist inside lofted smoke layers (Tesche et al., 2009; Veselovskii et al., 2016).

Lately, there has been observational evidence of smoke originating from large-scale fires with PLDR values that exceed the typical range. For example, in Sugimoto et al. (2010), values of 12 %–15 % at 532 nm are presented for both tropospheric and stratospheric smoke plumes reaching from Mongolia to Nagasaki and Tsukuba in 2007. Nisantzi et al. (2014) reported values of 9 %–18 % at 532 nm for smoke originating from Turkish fires and observed above Cyprus after 1–4 d of transport. A spectral dependence of smoke PLDR with decreasing values from UV to near-IR wavelength was presented for the first time by Burton et al. (2015). The measurements were performed above Denver, Colorado, with an airborne High Spectral Resolution Lidar (HSRL) instrument during the DISCOVER-AQ (Deriving Information on Surface Conditions from Column and Vertically Resolved Observations Relevant to Air Quality) field mission. This particular smoke plume was found at 8 km height, originating from Pacific Northwest wildfires, and exhibited PLDR values of 20 %, 9.3 % and 1.8 % at 355, 532 and 1064 nm, respectively.

In the past, many studies have used simpler or more complicated particle shape models in order to reproduce the lidar measurements of smoke. In Kahnert (2017), the PLDR of black carbon aggregates covered by a coating of sulfates was simulated by two different models: a closed cell model (i.e. each monomer in the aggregate is coated separately) and a coated aggregate model (i.e. the whole aggregate is coated). Their analysis showed that for thicker coating the coated cell model of volume-equivalent radius of 0.3 to 0.4 µm can provide PLDR values of the order of 15 % at 532 nm. Mishchenko et al. (2016) and Liu and Mishchenko (2018) used rather complex morphologies for smoke particles in order to reproduce the PLDR values measured by Burton et al. (2015). Amongst others, these morphologies included (a) a fractal aggregate partially embedded in a spherical sulfate cell, (b) two externally mixed spherical sulfate cells, each hosting an aggregate (models 6 and 11 in Fig. 1 in Liu and Mishchenko (2018) and (c) a high-density aspherical soot core, encapsulated in a circumscribing spheroid cell (with axial ratio of 0.9 to 1.2; model 4 in Fig. 2 in Mishchenko et al., 2016). All these morphologies reproduced successfully the smoke optical properties measured by Burton et al. (2015). Moreover, Luo et al. (2018) used 20 different configurations of coated fractal aggregates and showed that for a relatively small fractal dimension (i.e. relatively fresh aggregates), and for small black carbon fractions (i.e. densely coated aggregates; configuration C in Fig. 2 in Luo et al., 2018), the PLDR values can reach up to 40 %, 15 % and 6 % at 355, 532 and 1064 nm, respectively. Ishimoto et al. (2019) used fractal aggregates and artificial surface tension induced on the particles to mimic the effect of coating by water-soluble materials forming around the particles. This study present results for both the PLDR and the lidar ratio (LR), which is indicative of the composition of the particles. In Liu and Mishchenko (2019), tar-ball aggregates were used to model exceptionally strong PLDR as those measured by Burton et al. (2015). The aforementioned studies highlighted the fact that in order to reproduce significant PLDR values (higher than 20 % at 532 nm), the fractals need to be coated (i.e. shapes of "type-B, size 11, $Vr = 20$" shown in Fig. 4 of Ishimoto et al., 2019). We should point out though that most of the aforementioned studies refer to monodispersed particles, and averaging over size could possibly suppress some of the observed features.

In the spotlight of the large-scale Canadian fires of 2017, the discussion regarding the high PLDR values and their spectral dependence for smoke has been opened also for stratospheric smoke. These wildfires inserted large amounts of smoke to the lower stratosphere by explosive pyrocumulonimbus activity (Khaykin et al., 2018). In fact, the smoke load in the stratosphere was found to be comparable to that of a moderate volcanic eruption (Peterson et al., 2018). The smoke plumes encircled the Northern Hemisphere in nearly 20 d, reaching Europe in less than 10 d. Above Europe, their properties were intensively studied by the European Aerosol Research Lidar Network (EARLINET; Pappalardo et al., 2014). Multi-wavelength lidar measurements in central (Ansmann et al., 2018; Haarig et al., 2018; Hu et al., 2019) and southern Europe (Sicard et al., 2019) revealed high PLDR values at 355 and 532 nm and a strong spectral dependence from the UV to the near-IR wavelength. However, despite the extensive analysis of this event, the microphysical characterization of the stratospheric smoke particles is not yet adequate and further analysis is imperative to draw conclusions. Most of the microphysical properties reported for the stratosphere are retrieved from lidar measurements using inversion algorithms and assumed scattering models that are applied in EARLINET (e.g. Dubovik et al., 2006; Veselovskii et al., 2002). For example, the derived microphysical properties presented in Haarig et al. (2018) and Hu et al. (2019) are based on the lidar backscatter and extinction coefficient profiles that were used as inputs to inversion schemes. However, the observed PLDR values could not be reproduced by these studies due to the assumed shapes.

In contrast to prior studies, for our investigation for the stratospheric smoke originating from the Canadian wildfires, we do not adopt morphologically complex shapes of bare or coated smoke aggregates, which are associated with excessive computations. Instead, we propose a much simpler model of compact near-spherical particles. Our starting point and main assumption is that the particle near-spherical shape can be highly depolarizing, as shown in the work of Mishchenko and Hovenier (1995) and Bi et al. (2018). Our analysis shows that for the Canadian stratospheric smoke observed above Europe in August 2017, the PLDR and LR measurements along with their spectral dependence can be successfully reproduced with the proposed model of compact near-spherical particles. The size and refractive index of the particles are estimated as well and seem to agree well with past observations for aged smoke. We further examine the capability of this model to be used on an operational level and in particular as an extension to the Aerosol Robotic Network (AERONET) operational aerosol retrieval (Dubovik et al., 2006), since it provides a much simpler and faster solution with respect to more complicated shapes for stratospheric smoke particles (e.g. Mishchenko et al., 2016; Ishimoto et al., 2019).

Our paper is organized as follows: in Sect. 2, we discuss the methodology followed for the retrieval of the microphysical properties of stratospheric smoke by constructing look-up tables of PLDR and LR at 355, 532 and 1064 nm, assuming (a) near-spherical shapes and (b) more complicated Chebyshev particle shapes. In Sect. 3, we provide a brief description of the Canadian wildfires during August 2017, describing the mechanism that introduced the smoke particles into the lower stratosphere and the route of the smoke plume from Canada to Europe. The lidar measurements performed over Leipzig, Germany, are presented in this section. In Sect. 4, we provide the results of our microphysical retrieval. The discussion of these results and the future perspectives of our work are found in Sect. 5. Conclusions are summarized in Sect. 6.

2 Construction of look-up tables

For the retrieval of the smoke microphysical properties from the measured PLDR and LR at 355, 532 and 1064 nm, we constructed appropriate look-up tables using near-spherical shapes and more complicated shapes (i.e. Chebyshev particles), along with a range of size distributions and refractive indices based on values reported in the literature for smoke particles (Dubovik et al., 2002; Müller, 2005; Müller et al., 2007a; Nicolae et al., 2013; Giannakaki et al., 2016). For the construction of the look-up tables, we used the T-matrix code (Mackowski and Mishchenko, 1996; Mishchenko and Travis, 1998). The T-matrix outputs are used to calculate PLDR and LR as shown in Eqs. (1) and (2):

$$\mathrm{PLDR}(\lambda) = \frac{P_{11}(180^\circ) - P_{22}(180^\circ)}{P_{11}(180^\circ) + P_{22}(180^\circ)} \tag{1}$$

$$\mathrm{LR}(\lambda) = \frac{4\pi C_{\mathrm{ext}}(\lambda)}{C_{\mathrm{sca}}(\lambda) P_{11}(180^\circ)}, \tag{2}$$

where P_{ij} are the elements of the scattering matrix, C_{ext} and C_{sca} are the extinction and scattering cross sections, and λ is the wavelength (Fig. 1).

2.1 Near-spherical shapes

We modelled the near-spherical shapes using spheroid particles with different axial ratios ε. The axial ratio of a spheroid is defined as the ratio of the ellipse rotational axis (a) to the axis perpendicular to the rotational axis (b) as $\varepsilon = a/b$. If $\varepsilon > 1$, then the spheroid is characterized as prolate, whereas if $\varepsilon < 1$, the spheroid is characterized as oblate (Mishchenko et al., 2002; Dubovik et al., 2006). To describe the spheroidal shape in the spherical coordinate system we use Eq. (3) where r is the radius of the volume-equivalent sphere and θ, φ are the zenith and azimuth angles, respectively.

$$r(\theta,\varphi) = a\left[\sin^2\theta + \frac{a^2}{b^2}\cos^2\theta\right]^{-1/2} \tag{3}$$

For the present study, we used ε values from 0.6 to 1.55. Figure 2 presents some examples of the near-spherical shapes used, embedded in a perfectly spherical shell to demonstrate their deviation from the perfect sphere.

We assumed that the shape distribution of the near-spherical particles is a monomodal, normal distribution $n_{\mathrm{s}}(\varepsilon)$ as shown in Eq. (4), with σ_{s} the sigma of the distribution fixed to 0.05 and ε_{s} the mean axial ratio (Table 1). We also assume that the shape distribution does not change with particle size. The fixed width of the shape distribution σ_{s} is necessary for the reduction of the retrieval complexity. Its small

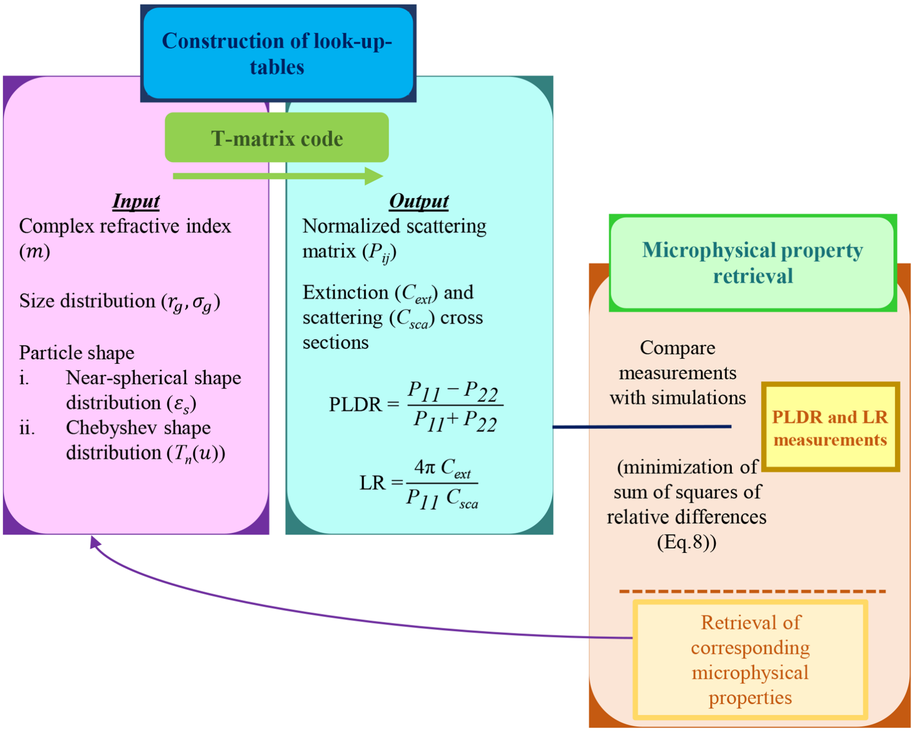

Figure 1. Overview of the methodology followed for the retrieval of the microphysical properties of the stratospheric smoke particles, using the PLDR and LR measurements at 355, 532 and 1064 nm: first, we construct appropriate look-up tables of PLDR and LR values for near-spherical and Chebyshev particles using T-matrix calculations, and then we search in the look-up tables for the solution that provides the best fit (minimization of Eq. 8) of the PLDR and LR measurements.

value is used to avoid the wash-out of the characteristic optical properties which are shown for a relatively narrow axial ratio range for near-spherical particles (e.g. Bi et al., 2018).

$$n_{\mathrm{s}}(\varepsilon) = \frac{1}{\sqrt{2\pi}\,\sigma_{\mathrm{s}}} \exp\left(-\frac{(\varepsilon - \varepsilon_{\mathrm{s}})^2}{2\sigma_{\mathrm{s}}}\right) \tag{4}$$

The size distributions considered for the near-spherical particles are monomodal and lognormal with mean geometric radius r_{g} and geometric standard deviation σ_{g}, as shown in Eq. (5). The grid used for r_{g} is 0.1–0.7 µm, while σ_{g} is fixed at 0.4. The fixed width of the size distribution σ_{g} is again a simplification we used in order to reduce the retrieval complexity, considering that this parameter does not greatly affect the lidar-derived optical properties (e.g. Burton et al., 2016). Choosing a lognormal size distribution over any other plausible type of distribution is not expected to alter our results significantly (Hansen and Travis, 1974).

$$n(r) = \frac{1}{\sqrt{2\pi}\, r\sigma_{\mathrm{g}}} \exp\left[-\frac{1}{2}\left(\frac{\ln\left(r/r_{\mathrm{g}}\right)}{\sigma_{\mathrm{g}}}\right)^2\right] \tag{5}$$

Moreover, a wavelength-independent complex refractive index m was assumed, with real part (mrr) varying from 1.35 to 1.85 and imaginary part (mri) varying from 0.005 to 0.5 (Dubovik et al., 2002; Müller et al., 2005; Nicolae et al., 2013; Giannakaki et al., 2016). An overview of the values used for the generation of the look-up tables for the near-spherical particles is presented in Table 1.

Table 1. The parameters used for the generation of the look-up tables of the near-spherical and Chebyshev particles.

Parameter	Range
r_{g} (µm) (step); r_{eff} (µm) (step)	0.1–0.7 (0.05); 0.15–1.05 (0.07)
σ_{g} (fixed)	0.4
mrr (step)	1.4–1.75 (0.05)
mri (step)	0.005–0.045 (0.005) and 0.05–0.5 (0.05)
ε_{s} (step)	0.6–1.55 (0.05)
σ_{s} (fixed)	0.05
u (step), T_2	±0.25, ±0.20, 0.15, ±0.05 (0.05)
u (step), T_4	±0.25, ±0.20, 0.15, ±0.05 (0.05)

2.2 Chebyshev particles

In order to investigate whether particles of more complicated shapes than the near-spherical shape can reproduce both the PLDR and LR measurements of stratospheric smoke, we also constructed look-up tables for smoke particles resembling “Chebyshev particles” using the T-matrix code. Chebyshev particles (Fig. 3) are produced by the deformation of a sphere

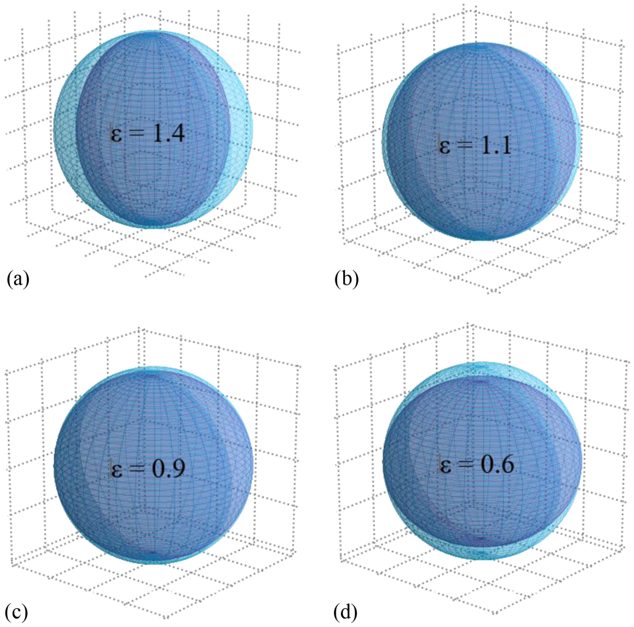

Figure 2. Examples of spheroids used (in dark blue colour), embedded in a perfectly spherical shell (in light blue colour), to visualize their deviation from the perfect sphere. **(a, b)** Prolate spheroids with **(a)** $\varepsilon = 1.4$ and **(b)** $\varepsilon = 1.1$, and **(c, d)** oblate spheroids with **(c)** $\varepsilon = 0.9$ and **(d)** $\varepsilon = 0.6$.

by means of a Chebyshev polynomial. In the spherical coordinates system, their shape is described as shown in Eq. (6), where r_0 is the radius of the perfect sphere, u is the deformation parameter, and $T_n(\cos\theta)$ is the Chebyshev polynomial of degree n (Mishchenko and Travis, 1998).

$$r(\theta,\varphi) = r_0\left(1 + uT_n(\cos\theta)\right), \quad |u| < 1 \tag{6}$$

Only Chebyshev polynomials of the second (T_2) and fourth (T_4) degree were used, with deformation parameter values of $u = \pm0.05, \pm0.10, \pm0.15, \pm0.20, \pm0.25$ and $u = \pm0.05, \pm0.10, \pm0.15$, respectively. We considered the same refractive indices as the ones used for the generation of the look-up tables of the near-spherical particles, while for the size distribution we used also monomodal, lognormal distributions. Table 1 summarizes the properties used for the construction of the look-up tables for Chebyshev particles.

3 Description of the dispersion and vertical distribution of smoke

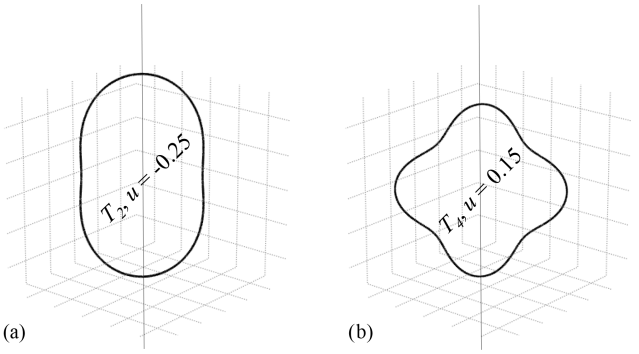

Figure 3. Examples of the Chebyshev particles used. **(a)** Chebyshev particle of the second degree (T_2) with deformation parameter $u = -0.25$ and **(b)** Chebyshev particle of the fourth degree (T_4) with deformation parameter $u = 0.15$.

The extreme pyroconvection (Fromm et al., 2010) that was recorded in the area of British Columbia (western Canada) during summer 2017, resulted in particularly strong updrafts that penetrated and released large amounts of smoke particles into the lower stratosphere (Peterson et al., 2018). Here, we use an ensemble of satellite observations from MODIS (Moderate Resolution Imaging Spectroradiometer) aboard Terra and Aqua, OMPS (Ozone Mapping and Profiler Suite) aboard the Suomi National Polar-orbiting Partnership (Suomi-NPP) and CALIOP (Cloud-Aerosol Lidar with Orthogonal Polarization) aboard the Cloud-Aerosol Lidar and Infrared Pathfinder Satellite Observation (CALIPSO) to identify the dispersion and vertical distribution of the plume above Canada. The combination of these observations is shown in Fig. 4, where True Color images from MODIS are overlaid with the fire active regions and thermal anomalies (red dots) from Suomi-NPP, and CALIPSO (green lines) overpasses on 8 and 15 August 2017.

Figures 5 and 6 show the backscatter coefficient and PLDR curtain plots at 532 nm from CALIPSO measurements. Based on these observations, smoke plumes were found above the regions of fire activity starting from the beginning of August (Fig. 4a), when the plumes remained in the troposphere, below 5–6 km (39–45° N, 123–125° W) (Fig. 5a, dashed red lines), exhibiting low PLDR values of the order of 3 %–4 % (Fig. 5b) at 532 nm. Then, on 12 August 2017, the unprecedented buoyancy force caused by the strong fire activity started lifting the plumes up towards the tropopause, while already on 15 August 2017 smoke covered a large part of northern Canada (Fig. 4b). CALIPSO observations on 15 August reveal that the plume lies in the stratosphere at 11–14 km height (63–69° N, 89–94° W) (Fig. 6a, dashed red lines) and PLDR values exceed 15 % at 532 nm (Fig. 6b).

Due to the altitude of the smoke plume, one could attribute such PLDR values to the beginning of ice formation. Indeed, radiosonde temperature profiles from two stations located underneath the smoke plume (green stars in Fig. 4b) reveal that the temperature above 11 km drops below −40 °C, at which point homogeneous ice formation can occur (Wallace and Hobbs, 2006). However, the PLDR values of cirrus clouds are usually no less than 40 % at 532 nm (Chen et al., 2002; Noel et al., 2002; Voudouri et al., 2020), whereas the values observed in this case are mostly between 15 % and

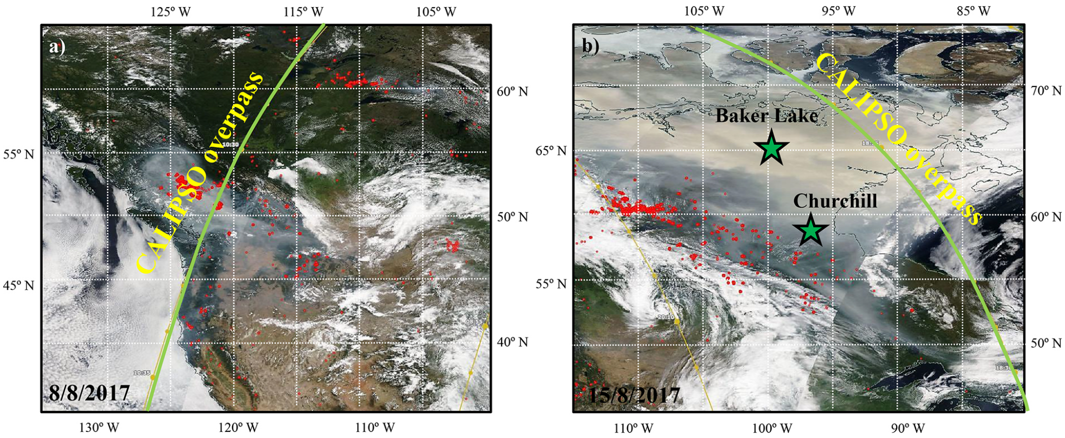

Figure 4. Corrected surface reflectance from MODIS, superimposed with active fire regions and thermal anomalies (red dots) and CALIPSO ascending and descending overpasses (green lines). Red circles denote the position of the smoke plume on **(a)** 8 August 2017 and **(b)** 15 August 2017. Green stars denote stations located underneath the smoke plume that perform regular radiosonde measurements. Maps are generated from NASA Worldview Snapshots.

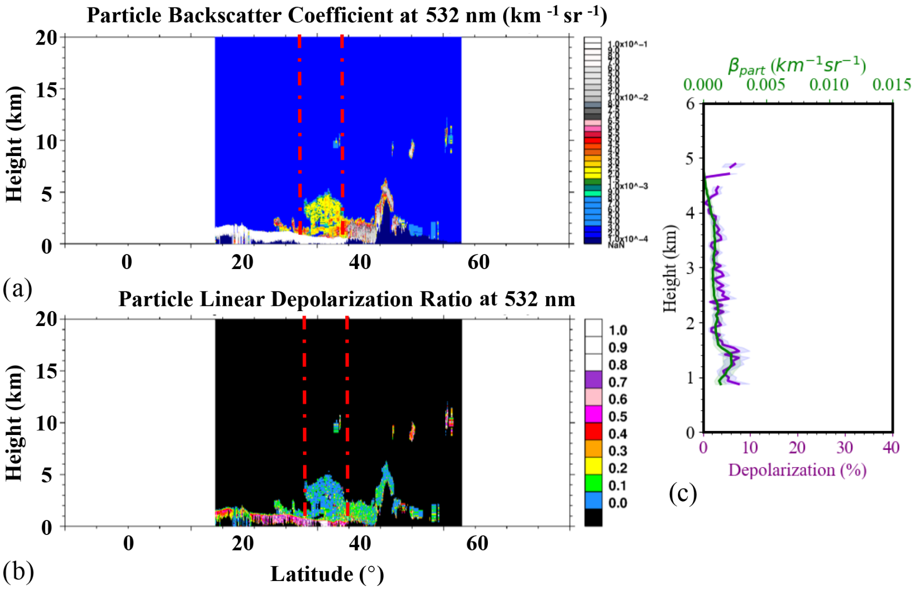

Figure 5. CALIPSO backscatter coefficient ($\mathrm{km}^{-1}\,\mathrm{sr}^{-1}$) and PLDR (%) that correspond to the nighttime overpass on 8 August 2017, 10:27–10:41 UTC, shown in Fig. 4a. **(a)** The smoke plume is located between 39° and 45° latitude, below 6 km in altitude. Dashed red lines denote the spatial averaging applied for the retrieval of optical properties shown in panel **(c)**. **(b)** PLDR values at 532 nm do not exceed values of 3 %–4 % at the height of the plume.

25 % at 532 nm, and remain so during the months of August and September following the stratospheric injection (Baars et al., 2019; Hu et al., 2019). Further analysis of CALIOP data provides a mean (median) value of the backscatter-related Ångström exponent (BAE) at 532/1064 nm of 0.9 (0.9) with a standard deviation of 1.07. For cirrus clouds, BAE values close to zero are expected, although, as indicated by the large standard deviation, CALIPSO data are highly noisy at these altitudes. A recent study by Yu et al. (2019) also showed that the largest fraction of stratospheric smoke particles consisted of organic carbon (98 % compared to 2 % for black carbon). Particles of such high organic carbon content serve poorly as ice nuclei (Kanji et al., 2017; Phillips et al., 2013). Although the possibility of small ice crystals formed inside the smoke layers cannot be excluded (largely due to the absence of in situ measurements), the aforementioned characteristics indicate that this plume consists primarily of smoke particles rather than ice crystals.

Inside the lower stratosphere, unaffected by the intensive tropospheric interactions, smoke particles started drift-

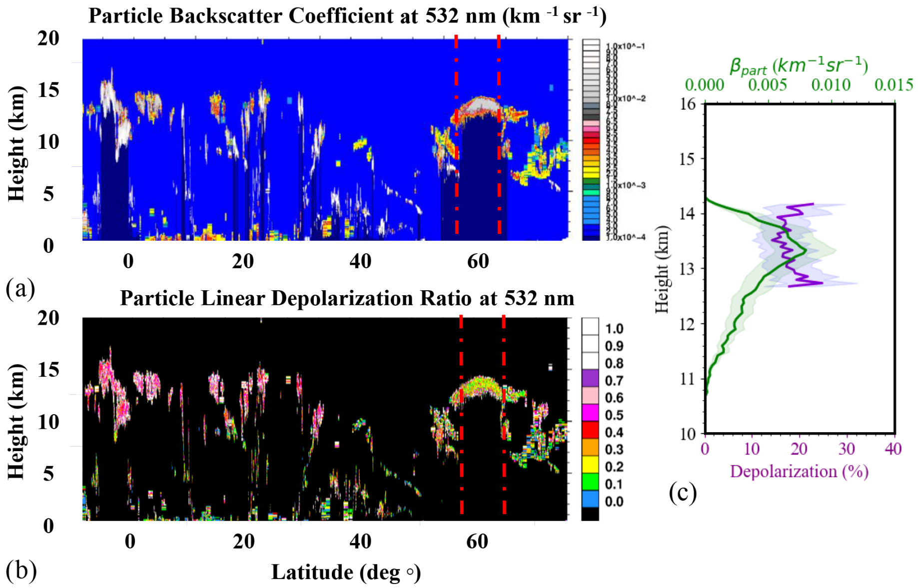

Figure 6. Same as Fig. 5 but for the daytime overpass of CALIPSO on 15 August 2017, 18:22–18:35 UTC, shown in Fig. 4b. **(a)** The smoke plume is now above the local tropopause at approximately 14 km, between 60° and 75° latitude. Dashed red lines denote the spatial averaging applied for the retrieval of optical properties shown in the right plot. **(b)** PLDR values at 532 nm (**c**, purple line) exceed 17 % at the height of the plume. (Note that the altitude range for this plot is from 10 to 16 km, whereas in Fig. 5b it is from 0 to 6 km.)

ing, following a northeasterly direction and first appeared over Europe approximately after mid-August (Khaykin et al., 2018; Ansmann et al., 2018; Hu et al., 2019).

Interestingly, even after 2 months of the initial stratospheric smoke injection, the plume seems to have sustained its high depolarization capability. During this period, the smoke plume has already encircled the Northern Hemisphere and it was detected by airborne lidar measurements performed above the Atlantic near the west coast of Ireland (Fig. 7b). Lidar observations showed PLDR values in the range of 10 %–14 % at 532 nm between 10 and 12 km (Fig. 7a). These observations were conducted in the framework of Wave-driven ISentropic Exchange (WISE) mission organized by the German Aerospace Centre (DLR) and support the high depolarization values detected for months over Europe by EARLINET, as shown in Fig. 7 in Baars et al. (2019).

Lidar measurements in Leipzig

The highest smoke load over EARLINET was been reported in Leipzig, Germany (Ansmann et al., 2018; Baars et al., 2019). Measurements at the Leibniz Institute of Tropospheric Research (TROPOS) were performed with the BERTHA (Backscatter Extinction lidar-Ratio Temperature Humidity profiling Apparatus) multi-wavelength polarization Raman lidar system. The system measures the total and cross-polarized components of the elastic backscattered light at 355, 532 and 1064 nm, which are used to derive the PLDR at these wavelengths. It is also able to perform independent measurements of the aerosol extinction coefficient at 387, 607 nm and (after optic rearrangement) at 1058 nm and thus has the ability to provide the LR profiles at 355, 532 and 1064 nm (Haarig et al., 2017). On 22 August 2017, the profiles of the stratospheric smoke backscatter and extinction coefficients at 355, 532 and 1064 nm and the smoke PLDR at 355 and 532 nm were derived from 2.5 h averaging of the lidar signals between 20:45 and 23:17 UTC. The PLDR value at 1064 nm was calculated using a 40 min averaging between 23:50 and 00:30 UTC (Haarig et al., 2018). The gap between the end of the first measurement and the beginning of the second corresponds to the necessary time for the rearrangement of BERTHA optics. To ensure the high quality of depolarization measurements, the $\Delta \pm 45$ depolarization calibration method proposed by Freudenthaler et al. (2009) was followed, while the effect of different parameters on the depolarization measurements of the BERTHA lidar system has been carefully assessed and is presented in detail in Haarig et al. (2017).

Layer-integrated values of PLDR and LR for the stratospheric smoke layer are shown in Fig. 8 and Table 2 along with their associated uncertainties. The derived LRs are typical for aged Canadian smoke at 355 nm (40 ± 16 sr) and 532 nm (66 ± 12 sr) (Müller et al., 2005; 2007b). Low signal-to-noise ratio at the plume height prevented detailed retrievals of the particle extinction coefficient at 1058 nm. Thus, for the LR values at 1064 nm, only few measurement points could be derived (Haarig et al., 2018). This yields a LR value of 92 ± 27 sr at 1064 nm. The increasing tendency of the LR from the UV to the visible part of the spectrum has

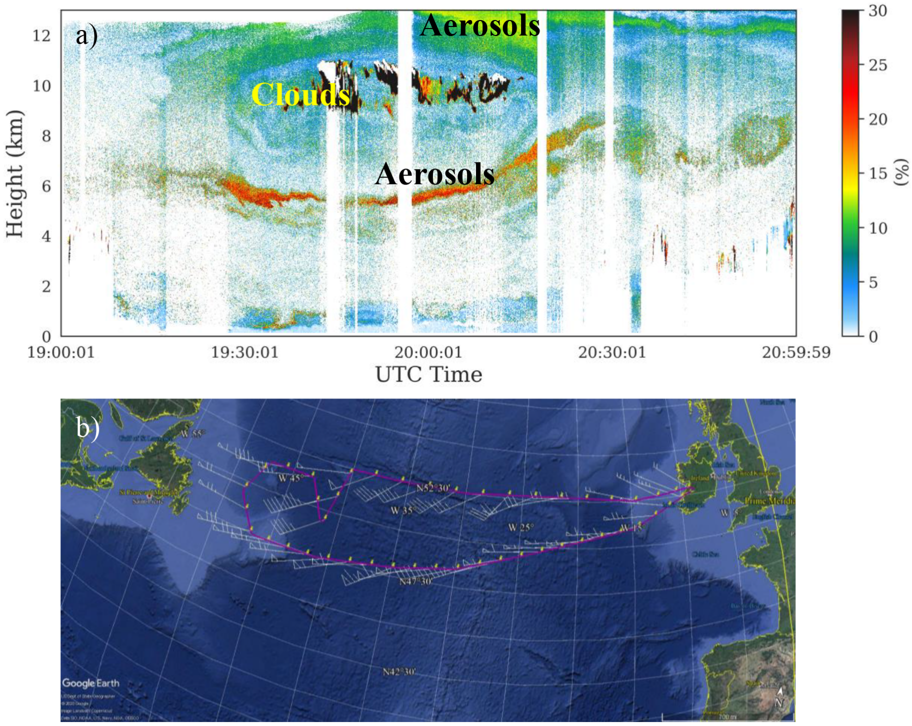

Figure 7. Time–height airborne lidar observations of the PLDR at 532 nm **(a)**. Measurements were performed over the Atlantic Ocean, between 19:00 and 21:00 UTC on 7 October 2017 by the DLR High Altitude and Long Range Research Aircraft (HALO) in the framework of the WISE mission. The track of the aircraft is shown in panel **(b)**, superimposed on the Google Earth map.

been also reported before for aged Canadian smoke (Müller et al., 2005, 2007b). Measurements reported in Haarig et al. (2018) suggest that there is an increase also at the near-IR wavelength, although there are currently no other available measurements of the LR of smoke particles at this wavelength. On the other hand, the PLDR values of stratospheric smoke are much larger than those usually reported in the past for tropospheric smoke. The layer-integrated PLDR value at 355 nm is 22.4 ± 2.5 %, decreasing to 18.4 ± 1.2 % at 532 nm and 4 ± 2.3 % at 1064 nm. The uncertainties in PLDR values include both the systematic errors and the standard deviation of the measurements.

These results are in agreement with the PLDR values measured above Lille and Palaiseau for the period of 24 to 31 August 2017 (Hu et al., 2019). To the best of our knowledge, up to now, the majority of observations of such smoke PLDR values refer to smoke particles found in the stratosphere (i.e. Ohneiser et al., 2020). The sole exception is the case study reported by Burton et al. (2015) (see also Table 2).

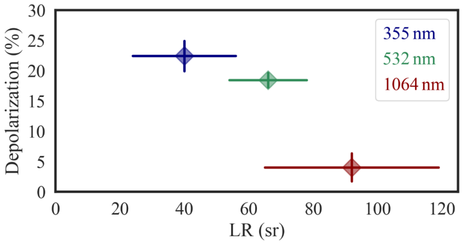

Figure 8. Intensive optical properties of the smoke particles found in the stratosphere, as measured on 22 August, in Leipzig, Germany. The LR mean values are plotted against the PLDR mean values, along with the corresponding errors. A typically increasing behaviour of LR for aged Canadian smoke is observed at 355 and 532 nm, while for the PLDR the effect is the opposite: the surprisingly large, layer-integrated mean values drop from the UV to the near-IR wavelength.

4 Smoke microphysical retrieval

4.1 Near-spherical particles

First, we present the smoke microphysical retrieval considering the near-spherical shape for the smoke particles, as described in Sect. 2.2. All the possible solutions are selected from the pre-calculated T-matrix look-up tables, based on Eq. (7). For each measured PLDR and LR, at each wavelength λ, the simulated value must be within the corresponding measurement error e:

$$\left|\delta_\lambda^{\mathrm{M}} - \delta_\lambda^{\mathrm{S}}\right| \le e\left(\delta_\lambda^{\mathrm{M}}\right) \text{ and } \left|\mathrm{LR}_\lambda^{\mathrm{M}} - \mathrm{LR}_\lambda^{\mathrm{S}}\right| \le e, \left(\mathrm{LR}_\lambda^{\mathrm{M}}\right) \qquad (7)$$

Table 2. LR and PLDR layer-integrated mean values at 355, 532 and 1064 nm for the stratospheric smoke layer, on 22 August 2017, in Leipzig, Germany (Haarig et al., 2018). Also shown are the multi-wavelength observations of PLDR and LR reported in previous and later studies for stratospheric or tropospheric smoke particles exhibiting high PLDR values.

	PLDR_{355} (%)	PLDR_{532} (%)	PLDR_{1064} (%)	LR_{355} (sr)	LR_{532} (sr)	LR_{1064} (sr)
Haarig et al. (2018)	22.4 ± 2.5	18.4 ± 1.2	4 ± 2.3	40 ± 16	66 ± 12	92 ± 27
Burton et al. (2015)	20.3 ± 3.6	9.3 ± 1.5	1.8 ± 0.2			
Hu et al. (2019)	23 ± 3	20 ± 3	5 ± 1	35 ± 6	54 ± 9	
	24 ± 4	18 ± 3	4 ± 1	45 ± 9	56 ± 12	
	28 ± 8	18 ± 3	5 ± 1	34 ± 12	58 ± 20	
Ohneiser et al. (2020)	23 ± 4.6	14 ± 1.4		83 ± 24.9	102 ± 20.4	
	20 ± 4	14 ± 1.4		53 ± 15.9	76 ± 15.2	
	26 ± 5.2	15 ± 1.5		97 ± 29.1	104 ± 20.8	

where “M” denotes measured PLDR and LR at wavelength $\lambda = 355$, 532 and 1064 nm, and “S” denotes the corresponding simulations. The solution is selected amongst the possible solutions based on the minimization criteria of Eq. (8) (see also Fig. 1).

$$\sum_{\lambda=355,532,1064}\left(\left(\frac{\delta_\lambda^{\mathrm{M}}-\delta_\lambda^{\mathrm{S}}}{e\left(\delta_\lambda^{\mathrm{M}}\right)}\right)^2+\left(\frac{\mathrm{LR}_\lambda^{\mathrm{M}}-\mathrm{LR}_\lambda^{\mathrm{S}}}{e\left(\mathrm{LR}_\lambda^{\mathrm{M}}\right)}\right)^2\right)=\min \quad (8)$$

Following this methodology, for the near-spherical particles, 10 possible solutions were found to reproduce the measurements within the measurement uncertainty. These are listed in Table 3 along with the resulting cost functions calculated with Eq. (8). For these solutions, the mean axial ratio ε_s of the particles covers the range of 1.1 to 1.4, while the range of the mean geometric radius r_g is 0.25 µm (respective effective radius: $r_\mathrm{eff} = 0.4$ µm) up to 0.45 µm ($r_\mathrm{eff} = 0.7$ µm). For the complex refractive index m, the mri does not exceed the value of $i0.03$, while the mrr takes values from 1.35 to 1.55. The minimization of the cost function (Eq. 8) is achieved for near-spherical particles with $\varepsilon_\mathrm{s} = 1.4$, $m = 1.55+i0.025$ and $r_\mathrm{g} = 0.25$ µm, suggesting a strong accumulation mode for the size distribution of the particles, with sufficiently small mri so as the characteristic enhancement in PLDR does not wash out due to the strong absorption (Bi et al., 2018). All possible solutions as well as the solution that minimizes the cost function are presented in Figs. 9 and 10.

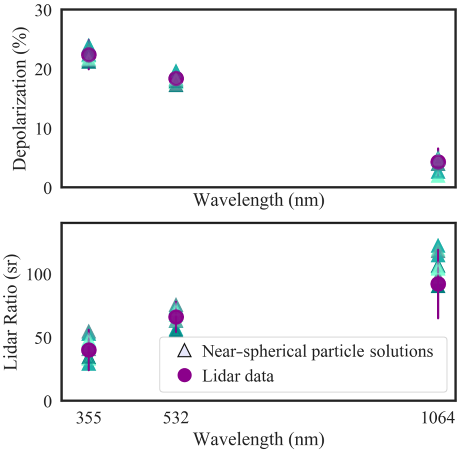

Figure 9. The reproduction of the measured PLDR and LR values, considering near-spherical particles. Purple circles correspond to measurements performed on 22 August 2017, in Leipzig, Germany, while purple lines correspond to the measurement uncertainties. Different light blue colour triangles denote simulations performed with the T-matrix code, assuming near-spherical particles. Each light blue triangle corresponds to a different solution found to reproduce the measurements within their uncertainties, as given in Table 3. For these solutions, the mean axial ratio ε_s ranges from 1.1 to 1.4, the mean geometric radius r_g ranges from 0.25 to 0.45 µm, and the wavelength-independent complex refractive index m ranges from 1.35 to 1.55 for the real part (mrr) and from 0.005 to 0.03 for imaginary part (mri).

4.2 Chebyshev particles

For Chebyshev particles of the second (T_2) and fourth degree (T_4) used herein, the search in the constructed look-up tables provided the solutions listed in Table 4. For all the solutions, deformation parameter for Chebyshev particles of the second degree ranges from $u = -0.25$ to 0.15, while for particles of the fourth degree only one solution was found with $u = -0.1$. These u values suggest small deviations from sphericity, meaning that these morphologies also resemble near-spherical shapes (see also Fig. 3). Only for two cases the size of the particles was found to be larger than the size of the near-spherical-shaped particles. In particular, the range of r_g was from 0.15 µm ($r_\mathrm{eff} = 0.2$ µm) to 0.55 µm ($r_\mathrm{eff} = 0.8$ µm). The complex refractive index in some cases exceeds the corresponding values for near-spherical particles. The range of the mri is from 0.005 to 0.055, and the range of the mrr is from 1.35 to 1.8. The minimization of the cost function

Table 3. Calculated properties of near-spherical particles that reproduce the PLDR and LR at 355, 532 and 1064 nm, as reported in Haarig et al. (2017). Also shown is the corresponding cost function of each solution. The solution that minimizes the cost function (Eq. 8) is highlighted in bold.

				Measurements – Leipzig (22 August 2017)						
				$PLDR_{355}$	$PLDR_{532}$	$PLDR_{1064}$	LR_{355}	LR_{532}	LR_{1064}	
				22.4 ± 1.5	41 ± 16	18.4 ± 0.6	66 ± 12	4.3 ± 0.7	92 ± 27	
				Simulations – near-spherical particles						
r_g	ε_s	mri	mrr	$PLDR_{355}$	$PLDR_{532}$	$PLDR_{1064}$	LR_{355}	LR_{532}	LR_{1064}	Cost function
0.45	1.1	0.005	1.35	23.19	17.73	2.08	33.03	67.37	118.96	2.54
0.50	1.1	0.005	1.35	23.85	19.53	2.80	29.08	56.02	121.76	4.02
0.35	1.2	0.020	1.45	23.21	17.22	3.89	43.14	62.77	106.10	1.48
0.35	1.2	0.025	1.45	23.10	17.29	3.85	54.30	75.10	117.69	3.25
0.30	1.3	0.025	1.50	22.21	18.08	4.90	43.17	62.97	104.92	0.48
0.30	1.3	0.030	1.50	22.35	18.31	4.87	52.55	73.40	114.38	1.74
0.25	1.4	0.020	1.55	21.15	17.87	4.86	33.99	55.01	90.12	1.49
0.25	**1.4**	**0.025**	**1.55**	**21.38**	**18.09**	**4.78**	**40.60**	**62.91**	**96.87**	**0.37**
0.25	1.4	0.030	1.55	21.61	18.31	4.70	48.15	71.64	103.84	0.81

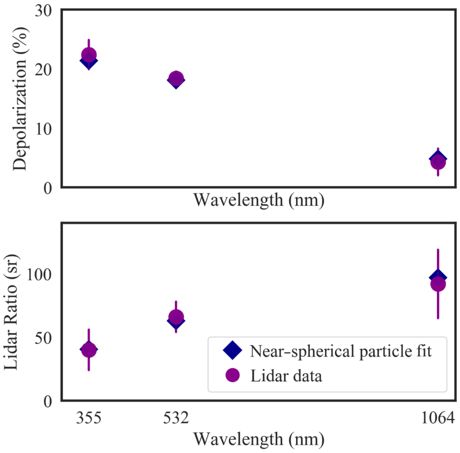

Figure 10. Same as Fig. 8 but only for the solution found to minimize the cost function of Eq. (8). Again, purple circles and lines correspond to measurements and measurements uncertainties on 22 August 2017, in Leipzig, Germany, while dark blue diamonds correspond to simulations assuming near-spherical particles of mean axial ratio $\varepsilon_s = 1.4$, mean geometric radius $r_g = 0.25\,\mu m$ and a wavelength-independent complex refractive index $m = 1.55 + i0.025$ (this is the solution highlighted in bold in Table 3).

(Eq. 8) is achieved for Chebyshev particles of the second degree with $u = -0.25$ (resembling an oblate near-spherical particle), complex refractive index $m = 1.65 + i0.03$ and mean geometric radius $r_g = 0.2\,\mu m$ (Fig. 11). For Chebyshev particles of the fourth degree, the sole solution presented values of $u = -0.1$, $m = 1.35 + i(0.01)$ and $r_g = 0.55\,\mu m$ (Fig. 12).

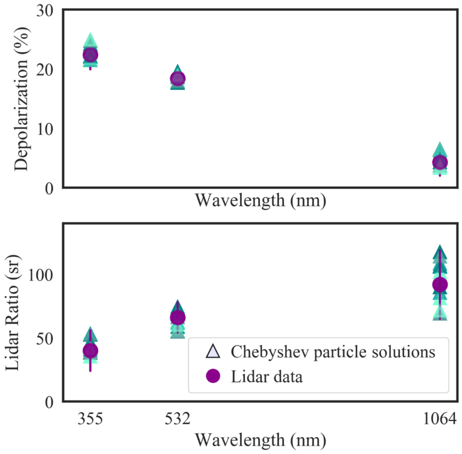

Figure 11. The reproduction of the measured PLDR and LR values, considering Chebyshev particles of the second degree (T_2). Purple circles correspond to measurements performed on 22 August 2017, in Leipzig, Germany, while purple lines correspond to the measurement uncertainties. Different light blue colour triangles denote simulations performed with the T-matrix code, assuming Chebyshev particles of the second degree (T_2). Each light blue triangle corresponds to a different solution found to reproduce the measurements within their uncertainties, as given in Table 4. For these solutions, the deformation parameter u ranges from -0.25 to 0.15, the mean geometric radius r_g ranges from 0.2 to 0.5 µm, and the wavelength-independent complex refractive index m takes values of 1.4 to 1.8 for mrr and 0.015 to 0.055 for mri.

Table 4. Calculated properties of Chebyshev particles of the second (T_2) and fourth (T_4) degree that reproduce the PLDR and LR at 355, 532 and 1064 nm, as reported in Haarig et al. (2017). Also shown is the corresponding cost function of each solution. The solution that minimizes the cost function (Eq. 8) is highlighted in bold.

r_g	ε_s	mri	mrr	PLDR_{355}	PLDR_{532}	PLDR_{1064}	LR_{355}	LR_{532}	LR_{1064}	Cost function
Simulations – Chebyshev particles of the second degree										
0.50	−0.05	0.015	1.4	22.59	18.05	3.30	43.95	62.86	114.13	1.08
0.35	−0.10	0.020	1.45	23.94	19.03	4.31	41.38	61.94	105.71	1.04
0.35	−0.10	0.025	1.45	24.18	19.10	4.27	52.32	74.01	117.19	2.76
0.25	−0.20	0.030	1.60	21.47	18.59	6.42	38.73	54.84	94.68	1.90
0.25	−0.20	0.035	1.60	21.44	18.86	6.35	45.44	62.15	101.45	1.43
0.25	−0.20	0.040	1.60	21.44	19.11	6.26	52.96	70.14	108.40	2.37
0.25	0.10	0.045	1.60	22.96	17.65	4.99	45.19	58.42	106.28	1.32
0.25	0.10	0.050	1.60	23.08	17.81	4.93	52.22	65.98	113.89	1.63
0.20	−0.25	0.025	1.65	21.80	19.11	5.13	35.10	55.73	80.98	1.53
0.20	**−0.25**	**0.030**	**1.65**	**21.97**	**19.30**	**5.00**	**40.35**	**61.97**	**85.27**	**0.86**
0.20	−0.25	0.035	1.65	22.13	19.48	4.88	46.27	68.68	89.57	1.09
0.15	0.15	0.050	1.80	24.68	18.82	3.66	38.08	55.30	68.87	2.58
0.15	0.15	0.055	1.80	24.87	18.94	3.59	41.63	59.64	71.03	2.16
Simulations – Chebyshev particles of the fourth degree										
0.55	−0.10	0.01	1.35	23.02	17.73	5.07	44.13	67.51	122.24	1.82

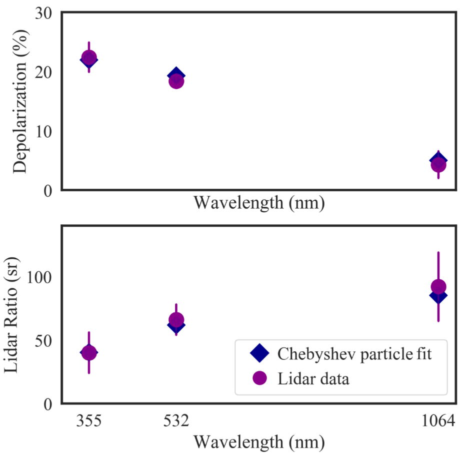

Figure 12. Same as Fig. 11 but only for the solution found to minimize the cost function of Eq. (8). Again, purple circles and lines correspond to measurements and measurement uncertainties on 22 August 2017, in Leipzig, Germany, while dark blue diamonds correspond to simulations assuming Chebyshev particles of the second degree (T_2) that resemble oblate near-spherical particles, with deformation parameter $u = -0.25$, mean geometric radius $r_g = 0.2\,\mu\mathrm{m}$ and a wavelength-independent complex refractive index $m = 1.65 + i0.03$ (this is the solution highlighted in bold in Table 4).

4.3 More case studies

Although the available literature on the PLDR and LR values of stratospheric smoke is for now limited, we see that we can reproduce all reported PLDR and LR values listed in Table 2 using the near-spherical shape model (Figs. S4–S9). All cases listed in Table 2 are associated with pyrocumulonimbus activity. As already mentioned, the case studies of Burton et al. (2015), Hu et al. (2019) and Haarig et al. (2018) refer to Canadian smoke, while the most recent case study presented by Ohneiser et al. (2020) refers to the Australian wildfires of 2019–2020. Tables S4–S9 present the properties of near-spherical particles and Chebyshev particles that reproduce the PLDR and LR observations reported in the aforementioned studies. Results are in line with the results presented for Haarig et al. (2017).

We note here that all the retrievals indicate fine particles, with mean geometric radius that does not exceed the value of 0.55 µm. The simulations presented by Bi et al. (2018; Fig. 2) suggest that for the near-spherical particles the measured spectral dependence of PLDR (steeply decreasing from the UV to the near-IR wavelength) could not be reproduced by coarse particles. Thus, the possibility of an optically significant coarse mode would have to be investigated with a different shape model. In any case though, the retrieved fine mode is in good agreement with in situ measurements of aged smoke particles (i.e. Dahlkötter et al., 2014). The presence of a pronounced accumulation mode is also suggested by the extinction-related Ångström exponent (EAE) measured in Leipzig (-0.3 ± 0.4 at 355/532 nm and 0.85 ± 0.3

at 532/1064 nm). According to Eck et al. (1999), a strong spectral slope in EAE can be associated with a prominent accumulation mode of the size distribution for smoke particles.

5 Discussion

Potential of the near-spherical model for AERONET products

Up to now, the use of near-spherical particles is found to well reproduce the lidar measurements of smoke optical properties, as well as their wavelength dependence. In this section, we further extend our study to examine the potential of using the near-spherical-shape model with Sun-photometer measurements on an operational level. Our main idea is whether the AERONET non-spherical scattering model could be extended to include also near-spherical particles for stratospheric smoke. In the current AERONET retrieval scheme, non-spherical particles are modelled as spheroids with axial ratios of 0.33–0.7 and 1.44–2.99, thus omitting the near-spherical particles. These ranges of axial ratios were selected towards an optimized retrieval for dust particles (Dubovik et al., 2006).

As an indication of the limitation of the current AERONET non-spherical model on reproducing the stratospheric smoke cases, we refer to AERONET version 2 morning observations (05:42 UTC) from the Lindenberg site on 23 August 2017 (180 km from Leipzig) and version 3 noon observations (11:03 UTC) from Punta Arenas on 8 January 2020. For these two cases, the Sun-photometer measurements should be affected by the presence of stratospheric smoke as shown in Haarig et al. (2018) and Ohneiser et al. (2020). The corresponding AERONET retrievals present residual errors higher than 5 %, which marks the threshold of a successful AERONET retrieval (Holben et al., 2006). For the first case over Lindenberg site, the retrievals were rejected from the quality assured level-2 AERONET products, while they were absent from the latest version of AERONET (version 3).

The following analysis shows possible benefits for the AERONET retrievals of stratospheric smoke from including the near-spherical model in the retrieval scheme. Towards this end, we show that the AERONET non-spherical model is limited in reproducing the phase function (P_{11}) of particles with near-spherical shapes. We should note here that this is only a first-level approximation of the full solution, since we do not account for the multiple scattering along the column of the Sun-photometer measurements, but rather assume only single scattering.

In the following, we tried to reproduce the P_{11} of the near-spherical stratospheric smoke particles presented herein, using the P_{11} calculated with the AERONET non-spherical model. For the latter, we used the pre-calculated AERONET kernels (Dubovik et al., 2006) for a large suite of refractive indices and size distributions (Table 5). The comparison is performed for the Sun-photometer wavelengths of 440, 670, 870 and 1020 nm. Figure 13a shows the P_{11} at 440 nm calculated for the near-spherical stratospheric smoke particles (purple line in the plots) and the comparison with the P_{11} at 440 nm calculated using the AERONET non-spherical model (blue lines) with $r_g = 0.25$ µm and all refractive indices listed in Table 5. The complete set of calculations (for all r_g and refractive indices listed in Table 5 and for AERONET wavelengths of 670, 870 and 1020 nm) is provided in Figs. S14–S69. Figure 13 shows also the degree of linear polarization ($-P_{12}/P_{11}$) (Fig. 13b) and the values of P_{22}/P_{11} (Fig. 13c). These plots are provided to show the potential of polarized measurements in better discerning the features of near-spherical particles (as is the case with the PLDR measurements).

Table 5. Parameters used for the calculations of the optical properties of smoke particles, using the non-spherical model of AERONET, in Figs. 12 and 13.

r_g (µm)	0.1, 0.15, 0.2, 0.25, 0.3, 0.4, 0.5, 0.8, 1.0, 1.5, 2.0, 2.5, 3.0, 4.0
mrr	1.35, 1.40, 1.44, 1.50, 1.54, 1.60, 1.65, 1.69
mri	10^{-8}, 0.0005, 0.015, 0.07, 0.11, 0.3, 0.5

In order to quantify the residual (Err) of the fitting, we use Eq. (9) (https://aeronet.gsfc.nasa.gov, last access: 15 July 2020):

$$\mathrm{Err} = \sqrt{\frac{\sum_{i=1}^{n} (\ln f^* - \ln f)^2}{N}} \cdot 100 = \%\,\mathrm{error}, \tag{9}$$

where $\ln f^*$ denotes P_{11} values calculated with the near-spherical model, $\ln f$ denotes the P_{11} values calculated with the AERONET non-spherical model, and N is the number of values, in terms of wavelengths and scattering angles. Err is calculated considering the four AERONET wavelengths at 440, 670, 870 and 1020 nm and the scattering angles from 0 to 150°, which indicate the measurement geometry of the AERONET Sun photometers.

The residuals for fitting the phase function of the near-spherical particles with the AERONET non-spherical model are presented in Fig. 14. The minimum Err is 9.4 %, whereas the limit of a successful AERONET retrieval is 5 % (Holben et al., 2006), indicating the limitations of the AERONET non-spherical model in reproducing the phase function of near-spherical smoke particles. Similar results for the Err considering only the wavelengths at 440, 670, 870 and 1020 nm are provided Figs. S10–S13.

Again, we should emphasize the fact that the residual threshold of 5 % denotes the multiple-scattered light, which may mask the differences seen in the single-scattering properties in Figs. 13 and 14. In order to have a clear understanding of whether the near-spherical shape model could in fact improve the AERONET retrieval for stratospheric smoke,

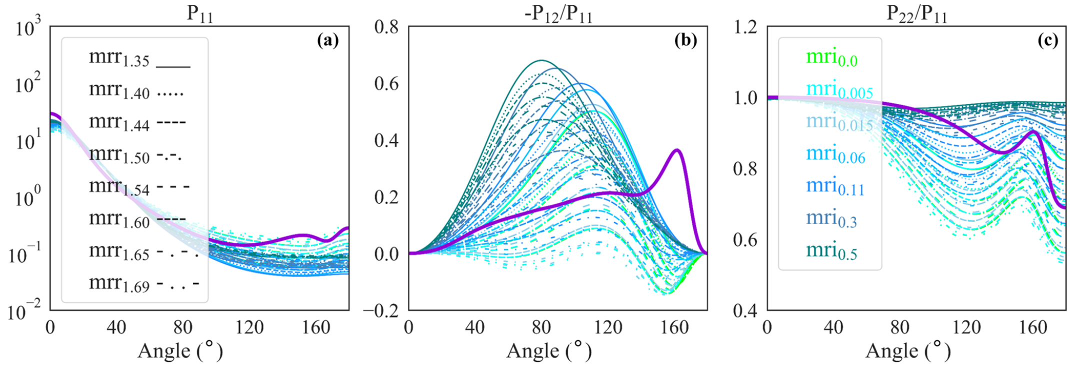

Figure 13. Comparison of the optical properties at $\lambda = 440$ nm for near-spherical particles (purple line) and the particles considered in the AERONET non-spherical model (blue lines). **(a)** P_{11} (phase function), **(b)** $-P_{12}/P_{11}$ (degree of linear polarization), **(c)** P_{22}/P_{11}. Purple lines in the plots show calculations considering the near-spherical particle properties derived for the stratospheric smoke particles from the Canadian fires, with mean axial ratio $\varepsilon_s = 1.4$, monomodal, lognormal size distribution with $r_g = 0.25$ µm, $\sigma_g = 0.4$ and complex refractive index $m = 1.55 - i0.03$. Blue lines in the plots show calculations using the AERONET non-spherical model, monomodal, lognormal size distributions with $r_g = 0.25$ µm and refractive indices of mrr = 1.35, 1.40, 1.44, 1.50, 1.54, 1.60, 1.65 and 1.69 for the real part (different line styles in the plot) and mri = 0.0, 0.005, 0.015, 0.06, 0.11, 0.3 and 0.5 for the imaginary part (different line colours in the plot).

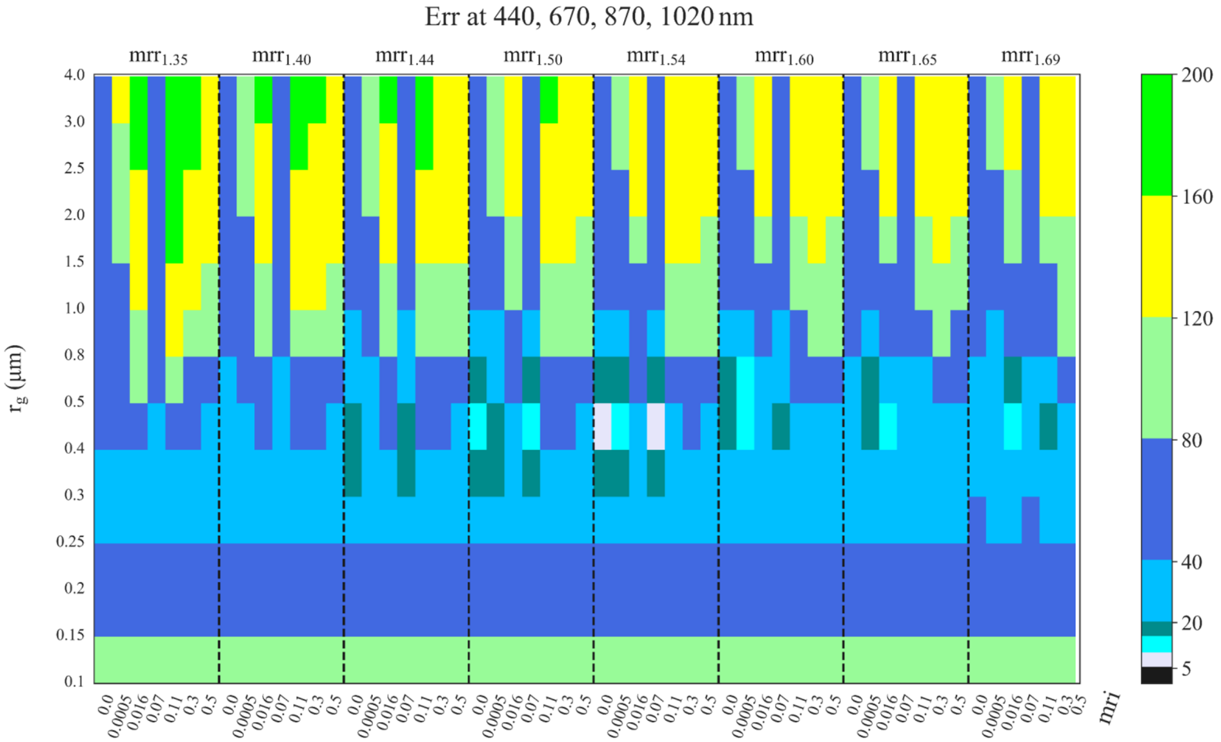

Figure 14. The residual error (Err) of fitting the phase functions at 440, 670, 870 and 1020 nm of the near-spherical particles presented in the paper, with the phase functions calculated with the AERONET non-spherical model for radius r_g and complex refractive index m shown on the y and x axes, respectively.

further analysis is imperative. For example, although a large range of the parameters affecting the retrieval and combination of these parameters were used, there are always other possible combinations that were not accounted for. To draw any strong conclusions, one would have to perform a numerical inversion of the stratospheric smoke measurements and investigate the corresponding residuals. This is part of our future work, continuing the characterization of stratospheric smoke particles with the combination of Sun-photometer and lidar measurements.

6 Conclusions

The unique optical properties of transported stratospheric smoke, originating from the pyrocumulonimbus activity of the large Canadian fires in 2017, were reproduced using T-matrix simulations and assuming near-spherical shapes for smoke. This is consistent with results of past studies showing that near-spherical particles produce PLDR values that can reach up to 100 % depending also on their size and composition (Bi et al., 2018) and that smoke particles in particular, when heavily coated or even encapsulated with weakly absorbing materials, can produce large depolarization with a noticeable spectral dependence (Mishchenko et al., 2016; Ishimoto et al., 2019). As a next step, we examined whether the AERONET retrieval could possibly be benefited by taking into account the near-spherical shape for stratospheric smoke. Sun-photometer measurements from Lindenberg and Punta Arenas revealed that for the current algorithm configuration, AERONET retrievals for stratospheric smoke cases are associated with high residual errors (higher than 5 %) and are eventually rejected. The extension of the AERONET scattering model to include the near-spherical shapes could possibly improve the retrieval for these cases that seem to become frequent. Our analysis does not intend to generalize on the performance of the AERONET retrieval on tropospheric biomass burning cases. It is focused on the stratospheric smoke cases related to pyrocumulonimbus activity.

In conclusion, studying the stratospheric smoke from the Canadian wildfire activity provided us with the great opportunity to show the potential of remote sensing measurements in investigating and deducing new optical and microphysical properties for the stratospheric smoke particles. Our analysis also highlighted the need for coordinated ground-based lidar network measurements, such as the ones provided by EARLINET, as an exploratory tool in investigating unknown processes in the stratosphere.

Data availability. The satellite products used in this study are the CALIPSO 5 km aerosol profile product (Vaughan et al., 2019) publicly available at the AERIS/ICARE database (ICARE data and services center, 2019); the MODIS Corrected Reflectance (True Color) images (Gumley et al., 2010) publicly available from NASA Worldview (NASA Worldview snapshots application center, 2019). The HALO-DLR aircraft lidar observations (level-2 data of depolarization and water vapour mixing ratio profiles) used in this study are available via the HALO database (https://halo-db.pa.op.dlr.de/, last access: 15 July 2020) (DLR, 2020). The AERONET version 3 data are available at https://aeronet.gsfc.nasa.gov/ (last access: 15 July 2020) (NASA, 2020). The pre-calculated AERONET kernels used in this work are publicly available at https://code.grasp-open.com/open/spheroid-package (last access: 15 July 2020) (GRASP OPEN, 2020). All datasets created during the calculation of the scattering properties of near-spherical and Chebyshev particles can be accessed through the ReACT-NOA database upon request to the corresponding author.

Supplement. The supplement related to this article is available online at: https://doi.org/10.5194/acp-20-14005-2020-supplement.

Author contributions. VA, AT and AG conceived the presented idea. VA and AT supported AG on the analysis, manuscript preparation and figure design. AT guided and supervised AG on the scattering model calculations and results interpretation. RC and LP performed the analysis on fractal aggregates scattering properties and provided AG with the results (not shown in the final paper). AG, AK and SS analysed the Microwave Limb Sounder (MLS) water vapour data and performed FLEXible PARTicle dispersion model (FLEXPART) runs to support the dispersion of the smoke and volcanic plumes (not shown in the paper). EM, MT and IT prepared the CALIPSO data and figures. MH, HB and AA collected and analysed Leipzig lidar measurements. TL, AL and OD supported AG to confirm T-matrix results for near-spherical particles. SG and MW performed the DLR HALO airborne lidar measurements and the corresponding analysis. DB advised AG on the interpretation of the results of this study. All authors provided critical feedback and helped shape the research, analysis and manuscript.

Competing interests. The authors declare that they have no conflict of interest.

Special issue statement. This article is part of the special issue “EARLINET aerosol profiling: contributions to atmospheric and climate research”. It does not belong to a conference.

Acknowledgements. The authors would like to thank Michael Mishchenko for making the T-matrix codes available (https://www.giss.nasa.gov/staff/mmishchenko/t_matrix.html, last access: 15 July 2020). We are grateful to EARLINET (https://www.earlinet.org/, last access: 15 July 2020) and ACTRIS (https://www.actris.eu, last access: 15 July 2020) for the data collection, calibration, processing and dissemination. We are grateful to the AERIS/ICARE Data and Services Center for providing access to the CALIPSO data used and their computational centre (http://www.icare.univ-lille1.fr/, last access: 15 July 2020). We thank the NASA/LaRC/ASDC for making available the CALIPSO products. The authors are grateful to the NASA EOS Aura MLS team for providing free access to the MLS water vapour data (https://mls.jpl.nasa.gov/, last access: 15 July 2020). We acknowledge the use of imagery from the Worldview Snapshots application (https://wvs.earthdata.nasa.gov/, last access: 15 July 2020), part of the Earth Observing System Data and Information System (EOSDIS). We acknowledge the PANhellenic GEophysical observatory of Antikythera (PANGEA) data centre for supporting all computations for the development of datasets for the calculation of the scattering properties of near-spherical and Chebyshev particles.

Financial support. The research leading to these results was supported through the European Research Council (ERC) under the European Community’s Horizon 2020 research and innovation framework programme – ERC grant agreement no. 725698 (D-

TECT). Anna Gialitaki acknowledges support of this work by the project “PANhellenic infrastructure for Atmospheric Composition and climatE chAnge” (MIS 5021516), which is implemented under the action “Reinforcement of the Research and Innovation Infrastructure”, funded by the operational programme “Competitiveness, Entrepreneurship and Innovation” (NSRF 2014–2020) and co-financed by Greece and the European Union (European Regional Development Fund). Eleni Marinou was funded by a DLR VO-R young investigator group and the Deutscher Akademischer Austauschdienst (grant no. 57370121). The NOA team acknowledges the support of the Stavros Niarchos Foundation (SNF).

Review statement. This paper was edited by Eduardo Landulfo and reviewed by three anonymous referees.

References

Ackerman, A. S.: Reduction of Tropical Cloudiness by Soot, Science, 288, 1042–1047, https://doi.org/10.1126/science.288.5468.1042, 2000.

Adachi, K. and Buseck, P. R.: Atmospheric tar balls from biomass burning in Mexico, J. Geophys. Res.-Atmos., 116, D05204, https://doi.org/10.1029/2010JD015102, 2011.

Amiridis, V., Balis, D. S., Giannakaki, E., Stohl, A., Kazadzis, S., Koukouli, M. E., and Zanis, P.: Optical characteristics of biomass burning aerosols over Southeastern Europe determined from UV-Raman lidar measurements, Atmos. Chem. Phys., 9, 2431–2440, https://doi.org/10.5194/acp-9-2431-2009, 2009.

Ansmann, A., Baars, H., Chudnovsky, A., Mattis, I., Veselovskii, I., Haarig, M., Seifert, P., Engelmann, R., and Wandinger, U.: Extreme levels of Canadian wildfire smoke in the stratosphere over central Europe on 21–22 August 2017, Atmos. Chem. Phys., 18, 11831–11845, https://doi.org/10.5194/acp-18-11831-2018, 2018.

Baars, H., Ansmann, A., Ohneiser, K., Haarig, M., Engelmann, R., Althausen, D., Hanssen, I., Gausa, M., Pietruczuk, A., Szkop, A., Stachlewska, I. S., Wang, D., Reichardt, J., Skupin, A., Mattis, I., Trickl, T., Vogelmann, H., Navas-Guzmán, F., Haefele, A., Acheson, K., Ruth, A. A., Tatarov, B., Müller, D., Hu, Q., Podvin, T., Goloub, P., Veselovskii, I., Pietras, C., Haeffelin, M., Fréville, P., Sicard, M., Comerón, A., Fernández García, A. J., Molero Menéndez, F., Córdoba-Jabonero, C., Guerrero-Rascado, J. L., Alados-Arboledas, L., Bortoli, D., Costa, M. J., Dionisi, D., Liberti, G. L., Wang, X., Sannino, A., Papagiannopoulos, N., Boselli, A., Mona, L., D’Amico, G., Romano, S., Perrone, M. R., Belegante, L., Nicolae, D., Grigorov, I., Gialitaki, A., Amiridis, V., Soupiona, O., Papayannis, A., Mamouri, R.-E., Nisantzi, A., Heese, B., Hofer, J., Schechner, Y. Y., Wandinger, U., and Pappalardo, G.: The unprecedented 2017–2018 stratospheric smoke event: decay phase and aerosol properties observed with the EARLINET, Atmos. Chem. Phys., 19, 15183–15198, https://doi.org/10.5194/acp-19-15183-2019, 2019.

Bi, L., Lin, W., Liu, D., and Zhang, K.: Assessing the depolarization capabilities of nonspherical particles in a super-ellipsoidal shape space, Opt. Express, 26, 1726–1742, https://doi.org/10.1364/OE.26.001726, 2018.

Burton, S. P., Hair, J. W., Kahnert, M., Ferrare, R. A., Hostetler, C. A., Cook, A. L., Harper, D. B., Berkoff, T. A., Seaman, S. T., Collins, J. E., Fenn, M. A., and Rogers, R. R.: Observations of the spectral dependence of linear particle depolarization ratio of aerosols using NASA Langley airborne High Spectral Resolution Lidar, Atmos. Chem. Phys., 15, 13453–13473, https://doi.org/10.5194/acp-15-13453-2015, 2015.

Burton, S. P., Chemyakin, E., Liu, X., Knobelspiesse, K., Stamnes, S., Sawamura, P., Moore, R. H., Hostetler, C. A., and Ferrare, R. A.: Information content and sensitivity of the $3\beta+2\alpha$ lidar measurement system for aerosol microphysical retrievals, Atmos. Meas. Tech., 9, 5555–5574, https://doi.org/10.5194/amt-9-5555-2016, 2016.

Chen, W.-N., Chiang, C.-W., and Nee, J.-B.: Lidar ratio and depolarization ratio for cirrus clouds, Appl. Optics, 41, 6470–6476, https://doi.org/10.1364/AO.41.006470, 2002.

Cheng, Z., Wang, S., Fu, X., Watson, J. G., Jiang, J., Fu, Q., Chen, C., Xu, B., Yu, J., Chow, J. C., and Hao, J.: Impact of biomass burning on haze pollution in the Yangtze River delta, China: a case study in summer 2011, Atmos. Chem. Phys., 14, 4573–4585, https://doi.org/10.5194/acp-14-4573-2014, 2014.

Dahlkötter, F., Gysel, M., Sauer, D., Minikin, A., Baumann, R., Seifert, P., Ansmann, A., Fromm, M., Voigt, C., and Weinzierl, B.: The Pagami Creek smoke plume after long-range transport to the upper troposphere over Europe – aerosol properties and black carbon mixing state, Atmos. Chem. Phys., 14, 6111–6137, https://doi.org/10.5194/acp-14-6111-2014, 2014.

DLR – Deutsches Zentrum für Luft- und Raumfahrt: HALO database, available at: https://halo-db.pa.op.dlr.de/, last access: 15 July 2020.

Dubovik, O., Holben, B., Eck, T. F., Smirnov, A., Kaufman, Y. J., King, M. D., Tanré, D., and Slutsker, I.: Variability of Absorption and Optical Properties of Key Aerosol Types Observed in Worldwide Locations, J. Atmos. Sci., 59, 590–608, https://doi.org/10.1175/1520-0469(2002)059<0590:VOAAOP>2.0.CO;2, 2002.

Dubovik, O., Sinyuk, A., Lapyonok, T., Holben, B. N., Mishchenko, M., Yang, P., Eck, T. F., Volten, H., Muñoz, O., Veihelmann, B., Sorokin, M., and Slutsker, I.: Application of spheroid models to account for aerosol particle nonsphericity in remote sensing of desert dust, J. Geophys. Res.-Atmos., 111, D11208, https://doi.org/10.1029/2005JD006619, 2006.

Eck, T. F., Holben, B. N., Reid, J. S., Dubovik, O., Smirnov, A., O’Neill, N. T., Slutsker, I., and Kinne, S.: Wavelength dependence of the optical depth of biomass burning, urban, and desert dust aerosols, J. Geophys. Res.-Atmos., 104, 31333–31349, https://doi.org/10.1029/1999JD900923, 1999.

Freudenthaler, V., Esselborn, M., Wiegner, M., Heese, B., Tesche, M., Ansmann, A., MüLLER, D., Althausen, D., Wirth, M., Fix, A., Ehret, G., Knippertz, P., Toledano, C., Gasteiger, J., Garhammer, M., and Seefeldner, M.: Depolarization ratio profiling at several wavelengths in pure Saharan dust during SAMUM 2006, Tellus B, 61, 165–179, https://doi.org/10.1111/j.1600-0889.2008.00396.x, 2009.

Fromm, M., Lindsey, D. T., Servranckx, R., Yue, G., Trickl, T., Sica, R., Doucet, P., and Godin-Beekmann, S.: The Untold Story of Pyrocumulonimbus, B. Am. Meteorol. Soc., 91, 1193–1210, https://doi.org/10.1175/2010BAMS3004.1, 2010.

Giannakaki, E., Van Zyl, P. G., Müller, D., Balis, D., and Komppula, M.: Optical and microphysical characterization of aerosol layers over South Africa by means of multi-wavelength depolarization and Raman lidar measurements, Atmos. Chem. Phys., 16, 8109–8123, https://doi.org/10.5194/acp-16-8109-2016, 2016.

GRASP OPEN: Platform for GRASP Open Source Code, available at: https://code.grasp-open.com/users/sign_in, last access: 15 July 2020.

Groß, S., Tesche, M., Freudenthaler, V., Toledano, C., Wiegner, M., Ansmann, A., Althausen, D., and Seefeldner, M.: Characterization of Saharan dust, marine aerosols and mixtures of biomass-burning aerosols and dust by means of multi-wavelength depolarization and Raman lidar measurements during SAMUM 2, Tellus B, 63, 706–724, https://doi.org/10.1111/j.1600-0889.2011.00556.x, 2011.

Groß, S., Esselborn, M., Weinzierl, B., Wirth, M., Fix, A., and Petzold, A.: Aerosol classification by airborne high spectral resolution lidar observations, Atmos. Chem. Phys., 13, 2487–2505, https://doi.org/10.5194/acp-13-2487-2013, 2013.

Gumley, L., Descloitres, J., and Schmaltz, J.: Creating Reprojected True Color MODIS Images: A Tutorial, Version 1.0.2, University of Wisconsin-Madison and NASA Goddard Space Flight Center, 17 pp., available at: https://cdn.earthdata.nasa.gov/conduit/upload/946/MODIS_True_Color.pdf (last access: 12 August 2019), 2010.

Haarig, M., Ansmann, A., Althausen, D., Klepel, A., Groß, S., Freudenthaler, V., Toledano, C., Mamouri, R.-E., Farrell, D. A., Prescod, D. A., Engelmann, R., and Baars, H.: Triple-wavelength depolarization-ratio profiling of Saharan dust over Barbados during SALTRACE in 2013 and 2014, Atmos. Chem. Phys., 17, 10767–10794, https://doi.org/10.5194/acp-17-10767-2017, 2017.

Haarig, M., Ansmann, A., Baars, H., Jimenez, C., Veselovskii, I., Engelmann, R., and Althausen, D.: Depolarization and lidar ratios at 355, 532, and 1064 nm and microphysical properties of aged tropospheric and stratospheric Canadian wildfire smoke, Atmos. Chem. Phys., 18, 11847–11861, https://doi.org/10.5194/acp-18-11847-2018, 2018.

Hansen, J. E. and Travis, L. D.: Light scattering in planetary atmospheres, Space Sci. Rev., 16, 527–610, https://doi.org/10.1007/BF00168069, 1974.

Holben, B. N., Eck, T. F., Slutsker, I., Smirnov, A., Sinyuk, A., Schafer, J., Giles, D., and Dubovik, O.: AERONET's Version 2.0 quality assurance criteria, in: Proc. SPIE, Remote Sensing of the Atmosphere and Clouds, 6408Q, https://doi.org/10.1117/12.706524, 2006.

Hoose, C. and Möhler, O.: Heterogeneous ice nucleation on atmospheric aerosols: A review of results from laboratory experiments, Atmos. Chem. Phys., 12, 9817–9854, https://doi.org/10.5194/acp-12-9817-2012, 2012.

Hu, Q., Goloub, P., Veselovskii, I., Bravo-Aranda, J.-A., Elisabeta Popovici, I., Podvin, T., Haeffelin, M., Lopatin, A., Dubovik, O., Pietras, C., Torres, B., and Chen, C.: Long-range-transported Canadian smoke plumes in the lower stratosphere over northern France, Atmos. Chem. Phys., 19, 1173–1193, https://doi.org/10.5194/acp-19-1173-2019, 2019.

Ishimoto, H., Kudo, R., and Adachi, K.: A shape model of internally mixed soot particles derived from artificial surface tension, Atmos. Meas. Tech., 12, 107–118, https://doi.org/10.5194/amt-12-107-2019, 2019.

Kahnert, M.: Optical properties of black carbon aerosols encapsulated in a shell of sulfate: comparison of the closed cell model with a coated aggregate model, Opt. Express, 25, 24579, https://doi.org/10.1364/OE.25.024579, 2017.

Kanji, Z. A., Ladino, L. A., Wex, H., Boose, Y., Burkert-Kohn, M., Cziczo, D. J., and Krämer, M.: Overview of Ice Nucleating Particles, Meteorol. Monogr., 58, 1.1–1.33, https://doi.org/10.1175/AMSMONOGRAPHS-D-16-0006.1, 2017.

Kaufman, Y. J., Tanré, D., and Boucher, O.: A satellite view of aerosols in the climate system, Nature, 419, 215–223, https://doi.org/10.1038/nature01091, 2002.

Khaykin, S. M., Godin-Beekmann, S., Hauchecorne, A., Pelon, J., Ravetta, F., and Keckhut, P.: Stratospheric Smoke With Unprecedentedly High Backscatter Observed by Lidars Above Southern France, Geophys. Res. Lett., 45, 1639–1646, https://doi.org/10.1002/2017GL076763, 2018.

Koch, D. and Del Genio, A. D.: Black carbon semi-direct effects on cloud cover: review and synthesis, Atmos. Chem. Phys., 10, 7685–7696, https://doi.org/10.5194/acp-10-7685-2010, 2010.

Liu, L. and Mishchenko, M. I.: Scattering and radiative properties of morphologically complex carbonaceous aerosols: A systematic modeling study, Remote Sens., 10, 1634, https://doi.org/10.3390/rs10101634, 2018.

Liu, L. and Mishchenko, M. I.: Modeling study of scattering and absorption properties of tar-ball aggregates, Appl. Optics, 58, 8648–8657, https://doi.org/10.1364/AO.58.008648, 2019.

Luo, J., Zhang, Y., and Zhang, Q.: A model study of aggregates composed of spherical soot monomers with an acentric carbon shell, J. Quant. Spectrosc. Ra., 205, 184–195, https://doi.org/10.1016/j.jqsrt.2017.10.024, 2018.

Mackowski, D. W. and Mishchenko, M. I.: Calculation of the T matrix and the scattering matrix for ensembles of spheres, J. Opt. Soc. Am. A, 13, 2266–2278, https://doi.org/10.1364/JOSAA.13.002266, 1996.

Marinou, E., Tesche, M., Nenes, A., Ansmann, A., Schrod, J., Mamali, D., Tsekeri, A., Pikridas, M., Baars, H., Engelmann, R., Ewald, F., and Amiridis, V.: Retrieval of ice-nucleating particle concentrations from lidar observations and comparison with UAV in situ measurements, Atmos. Chem. Phys., 19, 11315–11342, https://doi.org/10.5194/acp-19-11315-2019, 2019.

Mishchenko, M. I. and Hovenier, J. W.: Depolarization of light backscattered by randomly oriented nonspherical particles, Opt. Lett., 20, 1356–1358, https://doi.org/10.1364/OL.20.001356, 1995.

Mishchenko, M. I. and Travis, L. D.: Capabilities and limitations of a current FORTRAN implementation of the T-matrix method for randomly oriented, rotationally symmetric scatterers, J. Quant. Spectrosc. Ra., 60, 309–324, https://doi.org/10.1016/S0022-4073(98)00008-9, 1998.

Mishchenko, M. I., Travis, L. D., and Lacis, A. A.: Scattering, absorption and emission of light by small particles, Cambridge University Press, Cambridge, 2002.

Mishchenko, M. I., Dlugach, J. M., and Liu, L.: Linear depolarization of lidar returns by aged smoke particles, Appl. Optics, 55, 9968–9973, https://doi.org/10.1364/AO.55.009968, 2016.

Müller, D.: Raman lidar observations of aged Siberian and Canadian forest fire smoke in the free troposphere over Germany in 2003: Microphysical particle characterization, J. Geophys. Res., 110, D17201, https://doi.org/10.1029/2004JD005756, 2005.

Müller, D., Ansmann, A., Mattis, I., Tesche, M., Wandinger, U., Althausen, D., and Pisani, G.: Aerosol-type-dependent lidar ratios observed with Raman lidar, J. Geophys. Res., 112, D16202, https://doi.org/10.1029/2006JD008292, 2007a.

Müller, D., Mattis, I., Ansmann, A., Wandinger, U., Ritter, C., and Kaiser, D.: Multiwavelength Raman lidar observations of particle growth during long-range transport of forest-fire smoke in the free troposphere, Geophys. Res. Lett., 34, L05803, https://doi.org/10.1029/2006GL027936, 2007b.

NASA: AERONET, available at: https://aeronet.gsfc.nasa.gov/, last access: 15 July 2020.

Nichman, L., Wolf, M., Davidovits, P., Onasch, T. B., Zhang, Y., Worsnop, D. R., Bhandari, J., Mazzoleni, C., and Cziczo, D. J.: Laboratory study of the heterogeneous ice nucleation on black-carbon-containing aerosol, Atmos. Chem. Phys., 19, 12175–12194, https://doi.org/10.5194/acp-19-12175-2019, 2019.

Nicolae, D., Nemuc, A., Müller, D., Talianu, C., Vasilescu, J., Belegante, L., and Kolgotin, A.: Characterization of fresh and aged biomass burning events using multiwavelength Raman lidar and mass spectrometry, J. Geophys. Res.-Atmos., 118, 2956–2965, https://doi.org/10.1002/jgrd.50324, 2013.

Nisantzi, A., Mamouri, R. E., Ansmann, A., and Hadjimitsis, D.: Injection of mineral dust into the free troposphere during fire events observed with polarization lidar at Limassol, Cyprus, Atmos. Chem. Phys., 14, 12155–12165, https://doi.org/10.5194/acp-14-12155-2014, 2014.

Noel, V., Chepfer, H., Ledanois, G., Delaval, A., and Flamant, P. H.: Classification of particle effective shape ratios in cirrus clouds based on the lidar depolarization ratio, Appl. Optics, 41, 4245, https://doi.org/10.1364/AO.41.004245, 2002.

Ohneiser, K., Ansmann, A., Baars, H., Seifert, P., Barja, B., Jimenez, C., Radenz, M., Teisseire, A., Floutsi, A., Haarig, M., Foth, A., Chudnovsky, A., Engelmann, R., Zamorano, F., Bühl, J., and Wandinger, U.: Smoke of extreme Australian bushfires observed in the stratosphere over Punta Arenas, Chile, in January 2020: optical thickness, lidar ratios, and depolarization ratios at 355 and 532 nm, Atmos. Chem. Phys., 20, 8003–8015, https://doi.org/10.5194/acp-20-8003-2020, 2020.

Pappalardo, G., Amodeo, A., Apituley, A., Comeron, A., Freudenthaler, V., Linné, H., Ansmann, A., Bösenberg, J., D'Amico, G., Mattis, I., Mona, L., Wandinger, U., Amiridis, V., Alados-Arboledas, L., Nicolae, D., and Wiegner, M.: EARLINET: towards an advanced sustainable European aerosol lidar network, Atmos. Meas. Tech., 7, 2389–2409, https://doi.org/10.5194/amt-7-2389-2014, 2014.

Peterson, D. A., Campbell, J. R., Hyer, E. J., Fromm, M. D., Kablick, G. P., Cossuth, J. H., and DeLand, M. T.: Wildfire-driven thunderstorms cause a volcano-like stratospheric injection of smoke, npj Clim. Atmos. Sci., 1, 30, https://doi.org/10.1038/s41612-018-0039-3, 2018.

Phillips, V. T. J., Demott, P. J., Andronache, C., Pratt, K. A., Prather, K. A., Subramanian, R., and Twohy, C.: Improvements to an Empirical Parameterization of Heterogeneous Ice Nucleation and Its Comparison with Observations, J. Atmos. Sci., 70, 378–409, https://doi.org/10.1175/JAS-D-12-080.1, 2013.

Sicard, M., Granados-Muñoz, M. J., Alados-Arboledas, L., Barragán, R., Bedoya-Velásquez, A. E., Benavent-Oltra, J. A., Bortoli, D., Comerón, A., Córdoba-Jabonero, C., Costa, M. J., Sola, Y., and Yela, M.: Ground/space, passive/active remote sensing observations coupled with particle dispersion modelling to understand the inter-continental transport of wildfire smoke plumes, Remote Sens. Environ., 232, 111294, https://doi.org/10.1016/j.rse.2019.111294, 2019.

Sugimoto, N., Tatarov, B., Shimizu, A., Matsui, I., and Nishizawa, T.: Optical characteristics of forest-fire smoke observed with two-wavelength Mie-scattering lidars and a high-spectral-resolution lidar over Japan, Sci. Online Lett. Atmos., 6, 93–96, https://doi.org/10.2151/sola.2010-024, 2010.

Tesche, M., Ansmann, A., Müller, D., Althausen, D., Engelmann, R., Freudenthaler, V., and Groß, S.: Vertically resolved separation of dust and smoke over Cape Verde using multiwavelength Raman and polarization lidars during Saharan Mineral Dust Experiment 2008, J. Geophys. Res., 114, D13202, https://doi.org/10.1029/2009JD011862, 2009.

Vaughan, M., Garnier, A., Josset, D., Avery, M., Lee, K.-P., Liu, Z., Hunt, W., Pelon, J., Hu, Y., Burton, S., Hair, J., Tackett, J. L., Getzewich, B., Kar, J., and Rodier, S.: CALIPSO lidar calibration at 1064 nm: version 4 algorithm, Atmos. Meas. Tech., 12, 51–82, https://doi.org/10.5194/amt-12-51-2019, 2019.

Veselovskii, I., Kolgotin, A., Griaznov, V., Müller, D., Wandinger, U., and Whiteman, D. N.: Inversion with regularization for the retrieval of tropospheric aerosol parameters from multiwavelength lidar sounding, Appl. Optics, 41, 3685–3699, https://doi.org/10.1364/AO.41.003685, 2002.

Veselovskii, I., Goloub, P., Podvin, T., Bovchaliuk, V., Derimian, Y., Augustin, P., Fourmentin, M., Tanre, D., Korenskiy, M., Whiteman, D. N., Kolgotin, A., and Dubovik, O.: Retrieval of optical and physical properties of African dust from multiwavelength Raman lidar measurements during the SHADOW campaign in Senegal, Atmos. Chem. Phys., 16, 7013–7028, https://doi.org/10.5194/acp-16-7013-2016, 2016.

Voudouri, K. A., Giannakaki, E., Komppula, M., and Balis, D.: Variability in cirrus cloud properties using a PollyXT Raman lidar over high and tropical latitudes, Atmos. Chem. Phys., 20, 4427–4444, https://doi.org/10.5194/acp-20-4427-2020, 2020.

Wallace, J. M. and Hobbs, P. V.: Atmospheric Science: An Introductory Survey: Second Edition, Elsevier Academic Press, Amsterdam, Boston, 1–488, https://doi.org/10.1016/C2009-0-00034-8, 2006.

Worringen, A., Ebert, M., Trautmann, T., Weinbruch, S., and Helas, G.: Optical properties of internally mixed ammonium sulfate and soot particles – a study of individual aerosol particles and ambient aerosol populations, Appl. Optics, 47, 3835, https://doi.org/10.1364/AO.47.003835, 2008.

Wu, Y., Cheng, T., Zheng, L., and Chen, H.: Optical properties of the semi-external mixture composed of sulfate particle and different quantities of soot aggregates, J. Quant. Spectrosc. Ra., 179, 139–148, https://doi.org/10.1016/j.jqsrt.2016.03.012, 2016.

Yu, P., Toon, O. B., Bardeen, C. G., Zhu, Y., Rosenlof, K. H., Portmann, R. W., Thornberry, T. D., Gao, R. S., Davis, S. M., Wolf, E. T., de Gouw, J., Peterson, D. A., Fromm, M. D., and Robock, A.: Black carbon lofts wildfire smoke high into the stratosphere to form a persistent plume, Science, 365, 6453, https://doi.org/10.1126/science.aax1748, 2019.

Supplement of Atmos. Chem. Phys., 20, 14005–14021, 2020
https://doi.org/10.5194/acp-20-14005-2020-supplement

Supplement of

Is the near-spherical shape the “new black” for smoke?

Anna Gialitaki et al.

Correspondence to: Anna Gialitaki (togialitaki@noa.gr)

Table S1. The retrieved microphysical properties of near-spherical particles, along with their Particle Linear Depolarization Ratio (PLDR) and Lidar Ratio (LR) values at 355, 532 and 1064 nm, that reproduce the PLDR and LR reported in Haarig et al., (2017). Also shown is the corresponding cost function of each solution. The solution that minimizes the cost function (Eq. 8 in the manuscript) is highlighted in blue.

Measurements – Leipzig (22 August 2017)										
				PLDR$_{355}$	PLDR$_{532}$	PLDR$_{1064}$	LR$_{355}$	LR$_{532}$	LR$_{1064}$	
				22.4 ± 1.5	41 ± 16	18.4 ± 0.6	66 ± 12	4.3 ± 0.7	92 ± 27	
				Simulations – Near-Spherical particles						
r_g	ε_s	mri	mrr	PLDR$_{355}$	PLDR$_{532}$	PLDR$_{1064}$	LR$_{355}$	LR$_{532}$	LR$_{1064}$	Cost function
0.45	1.1	0.005	1.35	23.189	17.733	2.082	33.032	67.368	118.959	2.538
0.50	1.1	0.005	1.35	23.853	19.529	2.800	29.078	56.023	121.761	4.020
0.35	1.2	0.020	1.45	23.205	17.223	3.894	43.144	62.774	106.101	1.480
0.35	1.2	0.025	1.45	23.104	17.290	3.855	54.299	75.096	117.685	3.250
0.30	1.3	0.025	1.50	22.207	18.081	4.901	43.173	62.971	104.923	0.477
0.30	1.3	0.030	1.50	22.349	18.306	4.846	52.548	73.395	114.380	1.745
0.25	1.4	0.020	1.55	21.152	17.871	4.861	33.992	55.011	90.118	1.488
0.25	**1.4**	**0.025**	**1.55**	**21.382**	**18.096**	**4.784**	**40.596**	**62.914**	**96.868**	**0.374**
0.25	1.4	0.030	1.55	21.613	18.309	4.699	48.147	71.642	103.835	0.807

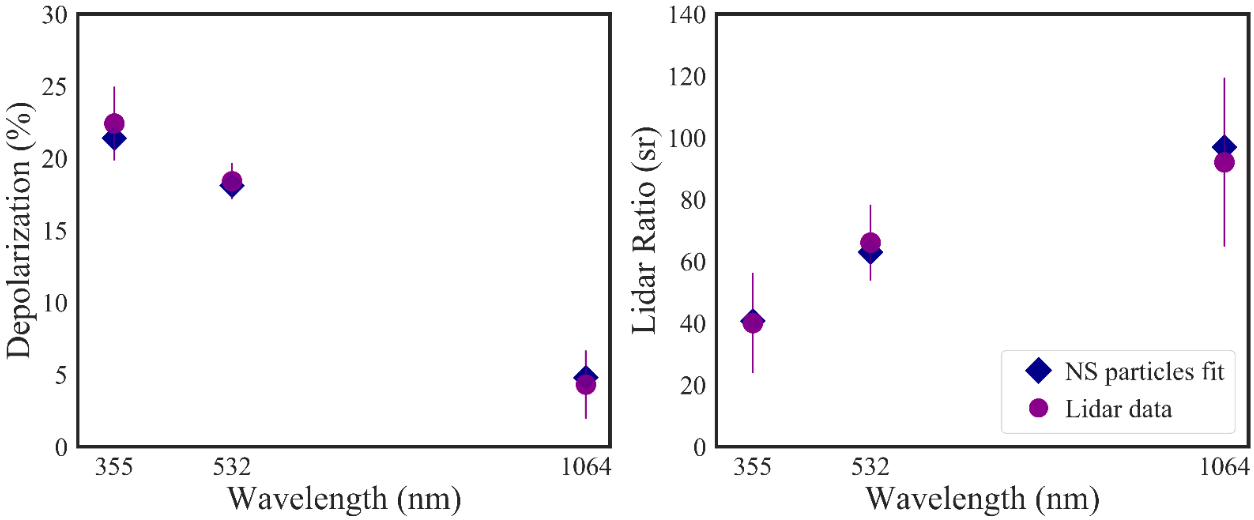

Figure S1. The reproduction of the measured PLDR and LR values, considering near-spherical particles. Purple circles correspond to measurements performed on 22 August 2017, at Leipzig, Germany, while purple lines correspond to the measurement uncertainties. Blue diamonds correspond to simulations performed with the T-matrix code, assuming near-spherical particles, for the values of mean axial ratio ε_s= 1.4, mean geometric radius r_g = 0.25 μm and a wavelength-independent complex refractive index m = 1.55 + i0.025.

Table S2. The retrieved microphysical properties of Chebychev particles of second degree, along with their PLDR and LR values at 355, 532 and 1064 nm, that reproduce the PLDR and LR reported in Haarig et al., (2017). Also shown is the corresponding cost function of each solution. The solution that minimizes the cost function (Eq. 8 in the manuscript) is highlighted in blue.

Simulations – Chebyshev particles of 2nd degree

r_g	u	mri	mrr	PLDR$_{355}$	PLDR$_{532}$	PLDR$_{1064}$	LR$_{355}$	LR$_{532}$	LR$_{1064}$	Cost function
0.50	-0.05	0.015	1.40	22.589	18.053	3.305	43.954	62.860	114.132	1.078
0.35	-0.10	0.020	1.45	23.941	19.032	4.306	41.378	61.939	105.708	1.037
0.35	-0.10	0.025	1.45	24.182	19.101	4.266	52.324	74.010	117.193	2.760
0.25	-0.20	0.030	1.60	21.472	18.594	6.423	38.733	54.839	94.683	1.897
0.25	-0.20	0.035	1.60	21.442	18.856	6.349	45.443	62.149	101.450	1.426
0.25	-0.20	0.040	1.60	21.435	19.109	6.261	52.956	70.141	108.397	2.368
0.25	0.10	0.045	1.60	22.957	17.647	4.986	45.191	58.417	106.283	1.317
0.25	0.10	0.050	1.60	23.079	17.814	4.932	52.224	65.980	113.890	1.629
0.20	-0.25	0.025	1.65	21.805	19.105	5.129	35.099	55.727	80.981	1.525
0.20	**-0.25**	**0.030**	**1.65**	**21.972**	**19.299**	**5.002**	**40.346**	**61.968**	**85.270**	**0.860**
0.20	-0.25	0.035	1.65	22.135	19.478	4.875	46.274	68.677	89.572	1.092
0.15	0.15	0.050	1.80	24.682	18.822	3.662	38.078	55.301	68.866	2.577
0.15	0.15	0.055	1.80	24.866	18.937	3.589	41.633	59.639	71.027	2.164

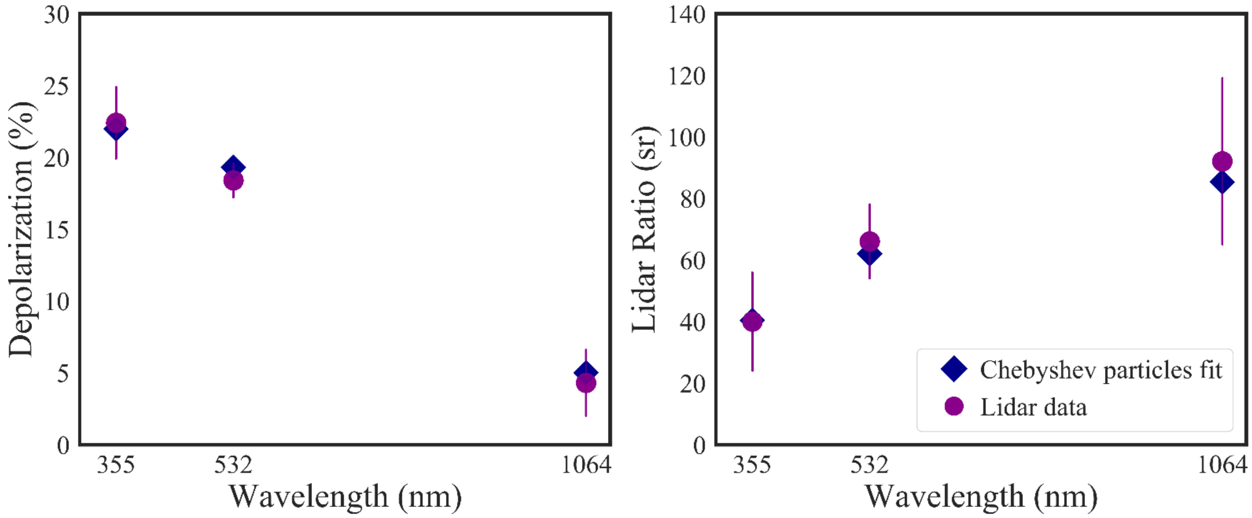

Figure S2. The reproduction of the measured PLDR and LR values, considering Chebyshev particles of second degree. Purple circles correspond to measurements performed on 22 August 2017, at Leipzig, Germany, while purple lines correspond to the measurement uncertainties. Blue diamonds correspond to simulations performed with the T-matrix code, assuming Chebyshev particles of second degree, for the values of deformation parameter u = - 0.25, mean geometric radius r_g = 0.2 μm and a wavelength-independent complex refractive index m = 1.65 + i0.03.

Table S3. The retrieved microphysical properties of Chebychev particles of fourth degree, along with their PLDR and LR values at 355, 532 and 1064 nm, that reproduce the PLDR and LR reported in Haarig et al., (2017). Only one solution was found.

Simulations – Chebyshev particles of 4^{th} degree										
r_g	u	mri	mrr	$PLDR_{355}$	$PLDR_{532}$	$PLDR_{1064}$	LR_{355}	LR_{532}	LR_{1064}	Cost function
0.55	-0.10	0.01	1.35	23.021	17.729	5.072	44.133	67.510	122.244	1.824

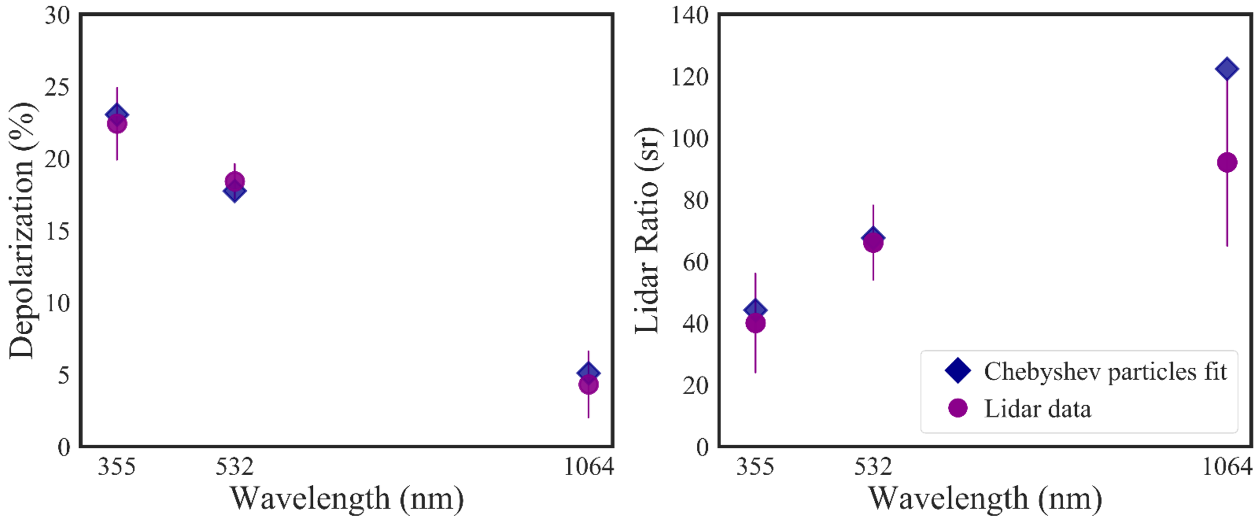

Figure S3. The reproduction of the measured PLDR and LR values, considering Chebyshev particles of fourth degree. Purple circles correspond to measurements performed on 22 August 2017, at Leipzig, Germany, while purple lines correspond to the measurement uncertainties. Blue diamonds correspond to simulations performed with the T-matrix code, assuming Chebyshev particles of fourth degree, for the values of deformation parameter u = - 0.1, mean geometric radius r_g = 0.55 μm and a wavelength-independent complex refractive index m = 1.35 + i0.01.

Table S4. The retrieved microphysical properties of near-spherical particles calculated, along with their PLDR and LR values at 355, 532 and 1064 nm, that reproduce the PLDR and LR reported in Hu et al., (2019). Also shown is the corresponding cost function of each solution. The solution that minimizes the cost function (Eq. 8 in the manuscript) is highlighted in blue.

				Measurements – Lille (31 August 2017)					
				PLDR$_{355}$	PLDR$_{532}$	PLDR$_{1064}$	LR$_{355}$	LR$_{532}$	
				28 ± 8	18 ± 3	5 ± 1	34 ± 12	58 ± 20	
				Simulations – Near-spherical particles					
r_g	ε_s	mri	mrr	PLDR$_{355}$	PLDR$_{532}$	PLDR$_{1064}$	LR$_{355}$	LR$_{532}$	Cost function
0.30	1.3	0.005	1.45	27.224	20.388	4.185	23.699	45.371	2.442
0.30	1.3	0.010	1.45	27.634	20.564	4.111	30.216	54.191	1.659
0.35	1.25	0.010	1.45	26.360	20.903	5.267	25.340	42.825	2.146
0.30	1.3	0.015	1.45	27.986	20.706	4.039	38.032	64.250	1.949
0.40	0.9	0.015	1.45	29.210	18.796	4.165	33.582	43.511	1.316
0.40	1.2	0.015	1.45	24.525	19.552	5.597	31.282	44.263	1.336
0.45	1.15	0.015	1.45	21.853	16.377	4.955	32.896	40.472	1.662
0.40	0.9	0.020	1.45	28.275	18.615	4.158	43.032	53.082	1.379
0.40	1.2	0.020	1.45	24.287	19.630	5.588	40.723	54.218	1.206
0.45	1.15	0.020	1.45	21.089	16.281	4.996	43.488	50.209	1.851
0.25	1.4	0.005	1.50	25.199	18.971	4.015	24.969	47.048	2.064
0.25	1.45	0.005	1.50	27.020	20.875	4.465	26.132	49.425	1.833
0.30	1.3	0.010	1.50	21.788	17.318	5.036	22.590	38.351	2.525
0.30	1.35	0.010	1.50	24.343	20.213	5.999	23.333	40.266	3.329
0.30	1.3	0.015	1.50	21.919	17.584	4.993	28.331	45.535	1.209
0.30	1.35	0.015	1.50	24.536	20.495	5.944	29.195	47.680	2.197
0.30	0.85	0.020	1.50	26.909	18.516	4.481	29.638	44.079	0.934
0.30	1.3	0.020	1.50	22.062	17.841	4.949	35.150	53.709	0.611
0.30	1.35	0.020	1.50	24.730	20.764	5.878	36.151	56.088	1.829
0.30	**0.85**	**0.025**	**1.50**	**26.865**	**18.643**	**4.438**	**36.307**	**51.896**	**0.512**
0.30	1.3	0.025	1.50	22.207	18.081	4.901	43.173	62.971	1.181
0.30	0.85	0.030	1.50	26.807	18.760	4.396	44.115	60.795	1.181
0.25	1.4	0.010	1.55	20.723	17.457	5.009	23.291	41.498	2.338
0.25	1.45	0.010	1.55	22.701	19.475	5.614	24.449	43.734	2.199
0.25	1.4	0.015	1.55	20.927	17.658	4.936	28.252	47.887	1.284
0.25	1.45	0.015	1.55	22.919	19.674	5.522	29.599	50.361	1.267

0.25	1.5	0.015	1.55	24.1923	20.997	5.914	30.589	52.070	2.228
0.25	1.4	0.020	1.55	21.1515	17.871	4.861	33.992	55.011	0.776
0.25	1.45	0.02	1.55	23.1466	19.885	5.422	35.550	57.725	0.957
0.25	1.4	0.025	1.55	21.3824	18.096	4.784	40.596	62.914	1.094

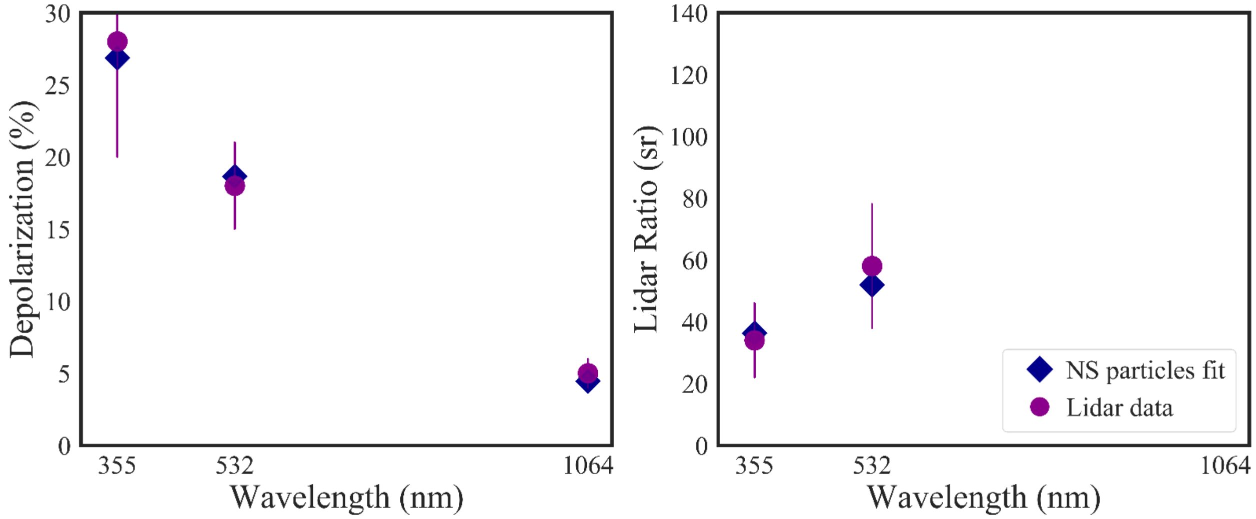

Figure S4. The reproduction of the measured PLDR and LR values, considering near-spherical particles. Purple circles correspond to measurements performed on 31 August 2017, at Lille, France, while purple lines correspond to the measurement uncertainties. Blue diamonds correspond to simulations performed with the T-matrix code, assuming near-spherical particles, for the values of mean axial ratio ε_s = 0.85, mean geometric radius r_g = 0.3 μm and a wavelength-independent complex refractive index m = 1.5 + i0.025.

Table S5. The retrieved microphysical properties of Chebyshev particles of second degree calculated, along with their PLDR and LR values at 355, 532 and 1064 nm, that reproduce the PLDR and LR reported in Hu et al., (2019). Also shown is the corresponding cost function of each solution. The solution that minimizes the cost function (Eq. 8 in the manuscript) is highlighted in blue.

Simulations-Chebyshev particles of 2^{nd} degree									
r_g	u	mri	mrr	$PLDR_{355}$	$PLDR_{532}$	$PLDR_{1064}$	LR_{355}	LR_{532}	Cost function
0.35	-0.10	0.010	1.45	23.088	18.892	4.371	24.778	42.457	2.056
0.35	-0.10	0.015	1.45	23.587	18.972	4.341	32.265	51.481	0.971
0.45	0.05	0.015	1.45	28.904	19.053	4.180	30.416	39.669	1.737
0.35	-0.10	0.020	1.45	23.941	19.032	4.306	41.378	61.939	1.274
0.45	0.05	0.020	1.45	27.796	18.656	4.181	40.472	49.009	1.212
0.30	-0.15	0.010	1.50	25.802	20.113	5.662	23.156	38.673	2.760
0.30	-0.15	0.015	1.50	25.676	20.321	5.616	28.859	45.770	1.620
0.30	-0.15	0.020	1.50	25.636	20.526	5.564	35.627	53.846	1.177
0.30	-0.15	0.025	1.50	25.638	20.726	5.474	43.599	62.987	1.839
0.25	-0.20	0.010	1.55	25.375	20.627	5.594	24.156	41.421	2.588
0.25	-0.20	0.015	1.55	25.634	20.807	5.511	29.168	47.788	1.647
0.25	-0.20	0.020	1.55	25.870	20.992	5.423	34.951	54.871	1.275
0.25	0.10	0.020	1.55	27.876	19.180	4.447	24.013	40.215	1.944
0.25	0.10	0.025	1.55	28.029	19.338	4.391	28.927	46.368	1.086
0.25	0.10	0.030	1.55	28.167	19.492	4.332	34.570	53.246	0.753
0.25	0.10	0.035	1.55	28.284	19.639	4.269	41.014	60.899	1.197
0.20	-0.25	0.005	1.60	27.733	19.926	4.443	23.233	43.627	2.045
0.20	-0.25	0.010	1.60	27.621	20.033	4.322	27.397	49.241	1.416
0.20	-0.25	0.015	1.60	27.532	20.138	4.203	32.218	55.355	1.186
0.20	-0.25	0.020	1.60	27.490	20.232	4.085	37.560	61.989	1.523
0.25	0.10	0.030	1.60	22.380	17.091	5.129	28.331	39.668	1.665
0.25	0.10	0.035	1.60	22.604	17.281	5.094	33.291	45.295	0.928
0.25	**0.10**	**0.040**	**1.60**	**22.797**	**17.468**	**5.033**	**38.894**	**51.532**	**0.726**
0.25	0.10	0.045	1.60	22.957	17.647	4.985	45.191	58.417	1.282
0.20	-0.25	0.010	1.65	21.578	18.405	5.497	22.049	39.853	2.724
0.20	-0.25	0.015	1.65	21.616	18.640	5.378	25.879	44.770	1.721
0.20	-0.25	0.020	1.65	21.673	18.854	5.256	30.279	50.091	1.024
0.20	-0.25	0.025	1.65	21.805	19.105	5.129	35.099	55.727	0.773
0.20	-0.25	0.030	1.65	21.972	19.299	5.002	40.346	61.968	1.074

0.15	0.15	0.040	1.85	23.577	18.201	4.460	28.149	40.754		1.583
0.15	0.15	0.045	1.85	23.691	18.323	4.386	30.838	44.033		1.236
0.15	0.15	0.050	1.85	23.796	18.438	4.310	33.703	47.494		1.050
0.15	0.15	0.055	1.85	23.887	18.544	4.234	36.750	51.131		1.054

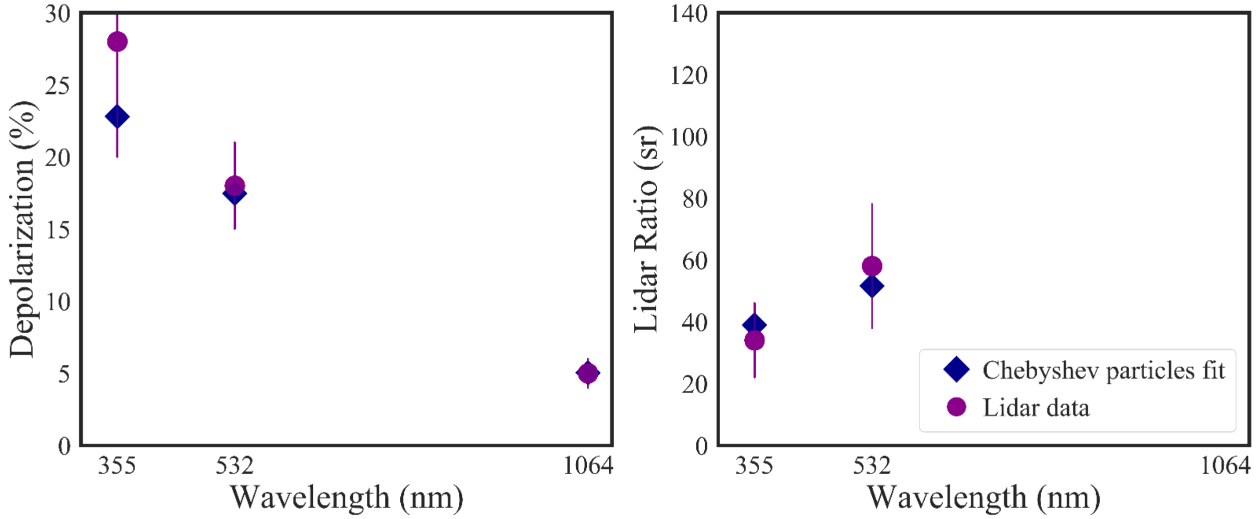

Figure S5. The reproduction of the measured PLDR and LR values, considering Chebyshev particles of second degree. Purple circles correspond to measurements performed on 31 August 2017, at Lille, France, while purple lines correspond to the measurement uncertainties. Blue diamonds correspond to simulations performed with the T-matrix code, assuming Chebyshev particles of second degree, for the values of deformation parameter u = 0.1, mean geometric radius r_g = 0.25 μm and a wavelength-independent complex refractive index m = 1.6 + i0.04.

Table S6. The retrieved microphysical properties of Chebyshev particles of fourth degree, along with their PLDR and LR values at 355, 532 and 1064 nm, that reproduce the PLDR and LR reported in Hu et al., (2019). Also shown is the corresponding cost function of each solution. The solution that minimizes the cost function (Eq. 8 in the manuscript) is highlighted in blue.

Simulations-Chebyshev particles of 4th degree									
r_g	u	mri	mrr	PLDR$_{355}$	PLDR$_{532}$	PLDR$_{1064}$	LR$_{355}$	LR$_{532}$	Cost function
0.50	-0.10	0.005	1.35	22.271	16.441	4.236	31.222	56.123	1.429
0.55	-0.10	0.005	1.35	23.105	17.572	5.082	28.315	50.004	0.786
0.55	-0.10	0.010	1.35	23.021	17.729	5.072	44.133	67.510	1.340
0.40	0.10	0.015	1.45	27.938	18.477	4.592	25.960	39.366	1.509
0.40	**0.10**	**0.020**	**1.45**	**27.387**	**18.480**	**4.551**	**34.838**	**49.319**	**0.426**
0.40	0.10	0.025	1.50	21.128	15.107	4.969	34.601	42.152	2.230
0.40	0.10	0.030	1.50	20.603	15.108	4.970	45.054	51.563	2.737

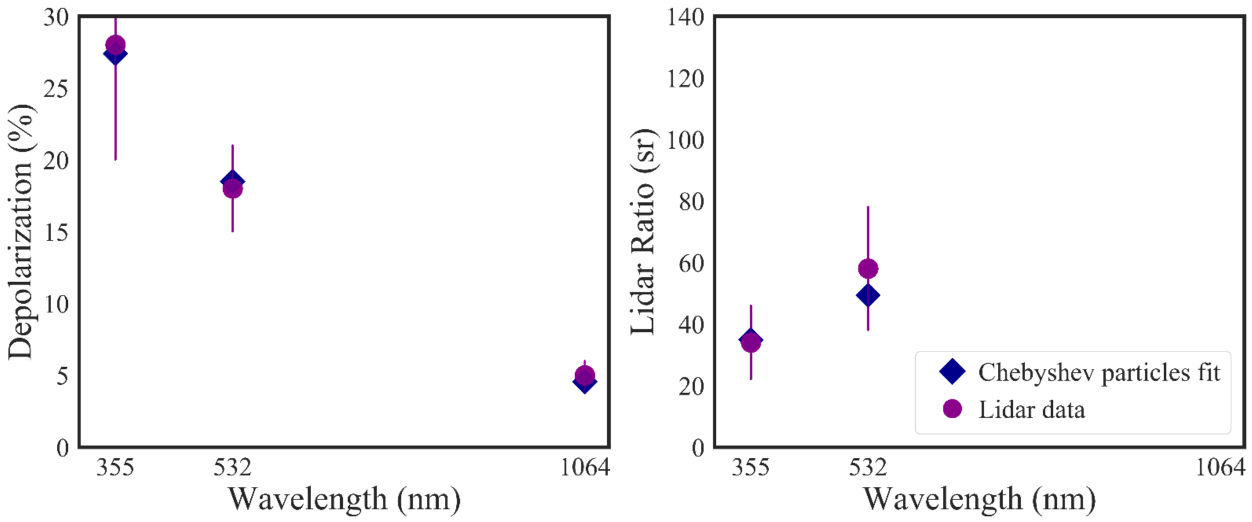

Figure S6. The reproduction of the measured PLDR and LR values, considering Chebyshev particles of fourth degree. Purple circles correspond to measurements performed on 31 August 2017, at Lille, France, while purple lines correspond to the measurement uncertainties. Blue diamonds correspond to simulations performed with the T-matrix code, assuming Chebyshev particles of fourth degree, for the values of deformation parameter u = 0.1, mean geometric radius r_g = 0.4 μm and a wavelength-independent complex refractive index m = 1.45 + i0.02.

Table S7. The retrieved microphysical properties of near-spherical particles, along with their PLDR and LR values at 355 and 532 nm, that reproduce the PLDR and LR reported in Ohneiser et al., (2020). Also shown is the corresponding cost function of each solution. The solution that minimizes the cost function (Eq. 8 in the manuscript) is highlighted in blue.

Measurements - Punta Arenas (8 January 2020)

PLDR$_{355}$	PLDR$_{532}$	LR$_{355}$	LR$_{532}$
23 ± 4.6	14 ± 1.4	83 ± 24.9	102 ± 20.4

Simulations - Near-spherical particles

r_g	ε_s	mri	mrr	PLDR$_{355}$	PLDR$_{532}$	LR$_{355}$	LR$_{532}$	Cost function
0.45	0.95	0.015	1.35	20.533	14.375	68.950	117.316	1.241
0.25	1.25	0.015	1.40	26.870	12.980	69.944	106.050	1.553
0.25	1.25	0.020	1.40	26.887	12.775	84.989	121.828	2.431
0.40	1.1	0.020	1.40	19.610	12.815	69.217	97.665	1.612
0.45	0.95	0.020	1.40	19.863	13.157	71.215	92.543	1.267
0.45	1.1	0.020	1.40	20.768	15.106	65.201	87.544	1.872
0.50	0.95	0.020	1.40	21.016	15.095	69.684	84.487	1.821
0.40	1.1	0.025	1.40	19.120	12.611	88.727	118.305	2.387
0.45	0.95	0.025	1.40	19.092	12.854	92.073	113.359	1.835
0.45	1.1	0.025	1.40	20.144	14.876	84.954	107.631	0.860
0.50	0.95	0.025	1.40	20.089	14.736	91.343	104.770	0.808
0.20	1.45	0.010	1.45	26.924	13.738	60.070	91.191	1.892
0.20	1.45	0.015	1.45	27.031	13.572	70.695	102.230	1.106
0.20	1.45	0.020	1.45	27.088	13.387	82.625	114.079	1.332
0.25	1.25	0.025	1.45	22.795	12.984	69.706	102.283	0.814
0.30	1.2	0.025	1.45	21.476	14.051	59.836	87.203	1.503
0.25	1.25	0.030	1.45	22.904	12.942	83.346	116.955	1.110
0.30	**1.2**	**0.030**	**1.45**	**21.471**	**14.072**	**73.113**	**101.938**	**0.271**
0.35	0.9	0.030	1.45	24.021	15.237	68.004	86.189	1.793
0.40	1.15	0.030	1.45	18.902	14.573	70.180	81.793	2.208
0.30	1.2	0.035	1.45	21.434	14.080	88.544	118.438	0.818
0.35	0.9	0.035	1.45	23.434	15.134	83.115	101.861	0.665
0.40	1.15	0.035	1.45	18.448	14.545	87.257	97.863	1.201
0.35	0.9	0.040	1.45	22.842	15.015	100.677	119.660	1.780
0.20	1.4	0.020	1.50	23.356	13.602	58.848	89.040	1.431
0.20	1.45	0.020	1.50	25.292	14.966	61.231	92.170	1.721

0.20	1.4	0.025	1.50	23.566	13.579	68.581	99.547	0.456
0.20	1.45	0.025	1.50	25.475	14.904	71.187	102.747	0.933
0.20	1.4	0.030	1.50	23.744	13.533	79.451	110.828	0.345
0.20	1.45	0.030	1.50	25.616	14.815	82.269	114.071	1.013
0.25	1.3	0.030	1.50	21.226	14.888	59.573	87.655	1.931
0.25	0.85	0.035	1.50	23.505	14.616	58.150	85.260	1.875
0.25	1.3	0.035	1.50	21.434	15.009	70.527	99.865	0.897
0.30	1.25	0.035	1.50	19.050	15.175	61.876	82.253	3.099
0.25	0.85	0.040	1.50	23.541	14.661	68.626	97.410	0.621
0.25	1.3	0.040	1.50	21.624	15.097	82.910	113.242	1.007
0.30	1.25	0.040	1.50	19.138	15.352	74.103	95.106	1.879
0.25	0.85	0.045	1.50	23.546	14.690	80.509	110.775	0.452
0.15	0.75	0.030	1.55	27.353	13.055	63.062	90.626	2.303
0.20	1.4	0.030	1.55	20.489	14.088	59.107	88.491	1.661
0.15	0.75	0.035	1.55	27.463	12.938	70.785	98.602	1.785
0.20	1.4	0.035	1.55	20.749	14.162	68.125	98.458	0.640
0.15	0.75	0.040	1.55	27.536	12.818	79.172	106.924	1.767
0.20	1.4	0.040	1.55	20.982	14.213	78.106	109.115	0.376
0.15	0.75	0.045	1.55	27.569	12.678	88.228	115.622	2.368
0.20	1.4	0.045	1.55	21.199	14.237	89.061	120.459	1.060
0.25	0.85	0.050	1.55	18.422	13.365	65.307	88.740	2.124
0.25	0.85	0.055	1.55	18.496	13.476	75.748	100.377	1.190
0.15	0.75	0.040	1.60	27.022	14.633	61.547	91.0133	2.001
0.15	0.75	0.045	1.60	27.182	14.577	68.600	98.7133	1.357
0.15	0.75	0.050	1.60	27.301	14.496	76.214	106.769	1.129
0.15	0.75	0.055	1.60	27.386	14.399	84.395	115.146	1.409
0.15	0.75	0.040	1.55	27.536	12.818	79.172	106.924	1.767

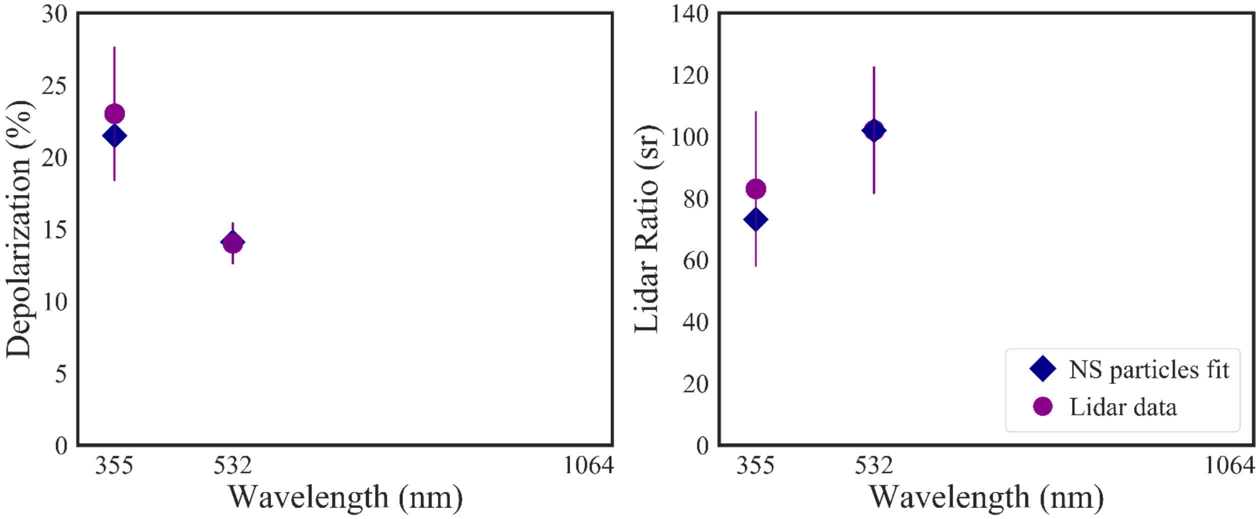

Figure S7. The reproduction of the measured PLDR and LR values, considering near-spherical particles. Purple circles correspond to measurements performed on 8 January 2020, at Punta Arenas, Chile, while purple lines correspond to the measurement uncertainties. Blue diamonds correspond to simulations performed with the T-matrix code, assuming near-spherical particles, for the values of mean axial ratio ε_s = 1.2, mean geometric radius r_g= 0.3 μm and a wavelength-independent complex refractive index m = 1.45 + i0.03.

Table S8. The retrieved microphysical properties of Chebychev particles of the second degree, along with their PLDR and LR values at 355 and 532 nm, that reproduce the PLDR and LR reported in Ohneiser et al., (2020). Also shown is the corresponding cost function of each solution. The solution that minimizes the cost function (Eq. 8 in the manuscript) is highlighted in blue

Simulations-Chebyshev particles of 2nd degree

r_g	u	mri	mrr	PLDR$_{355}$	PLDR$_{532}$	LR$_{355}$	LR$_{532}$	Cost function
0.40	-0.05	0.020	1.40	20.090	13.277	66.484	97.663	1.153
0.40	-0.05	0.025	1.40	19.813	13.047	86.104	118.240	1.59
0.40	0.05	0.035	1.45	22.385	15.166	82.266	95.045	0.828
0.40	0.05	0.040	1.45	21.555	14.941	101.548	112.991	1.395
0.20	0.10	0.030	1.50	27.517	13.750	59.517	90.605	2.198
0.20	0.10	0.035	1.50	27.547	13.692	69.021	101.521	1.341
0.20	0.10	0.040	1.50	27.545	13.606	79.666	113.328	1.381
0.25	-0.15	0.040	1.55	18.754	15.254	60.971	83.462	3.262
0.20	0.10	0.045	1.55	24.027	14.140	65.164	97.931	0.613
0.20	**0.10**	**0.050**	**1.55**	**24.130**	**14.157**	**74.722**	**108.887**	**0.297**
0.20	0.10	0.055	1.55	24.197	14.151	85.247	120.608	0.919
0.15	-0.25	0.025	1.60	23.345	12.886	59.601	87.295	2.041
0.15	-0.25	0.030	1.60	23.395	12.791	67.061	94.899	1.284
0.15	-0.25	0.035	1.60	23.436	12.690	75.143	102.756	0.986
0.20	0.10	0.055	1.60	20.475	13.911	64.504	92.894	1.056
0.15	-0.25	0.035	1.65	20.722	13.836	60.370	88.164	1.545
0.15	-0.25	0.040	1.65	20.953	13.810	67.281	95.492	0.717
0.15	-0.25	0.045	1.65	21.094	13.768	74.976	103.061	0.306
0.15	-0.25	0.050	1.65	21.267	13.673	83.039	111.062	0.394
0.15	-0.25	0.055	1.65	21.397	13.591	91.758	119.209	1.042
0.15	-0.25	0.045	1.70	18.466	14.451	62.057	88.638	2.212
0.15	-0.25	0.050	1.70	18.770	14.460	68.548	95.691	1.386
0.15	-0.25	0.055	1.70	19.045	14.454	75.748	102.914	0.932

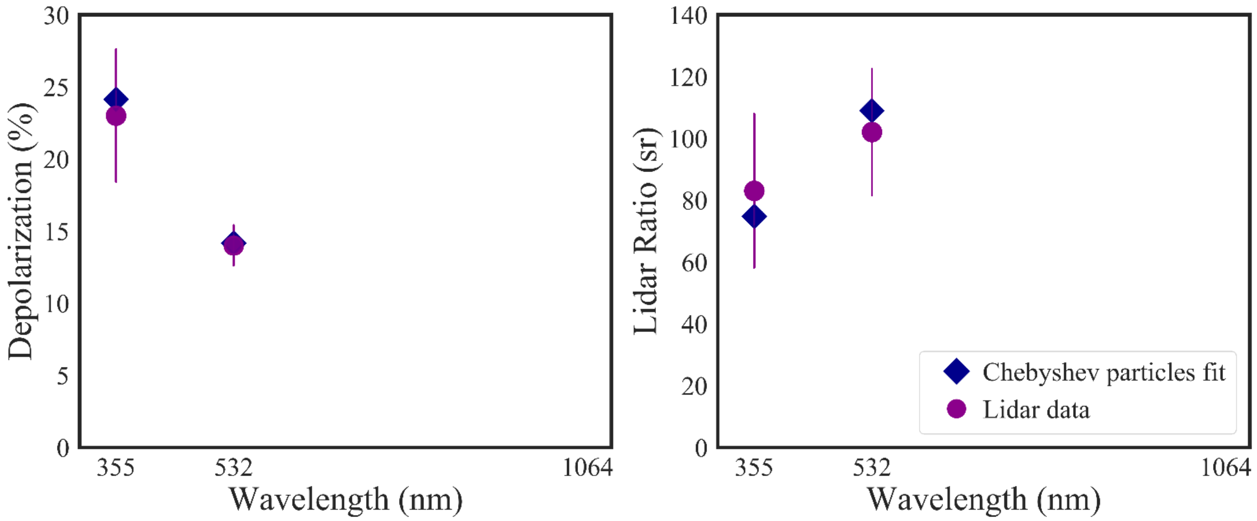

Figure S8. The reproduction of the measured PLDR and LR values, considering Chebyshev particles of second degree. Purple circles correspond to measurements performed on 8 January 2020, at Punta Arenas, Chile, while purple lines correspond to the measurement uncertainties. Blue diamonds correspond to simulations performed with the T-matrix code, assuming Chebyshev particles of second degree, for the values of deformation parameter $u = 0.1$, mean geometric radius $r_g = 0.2$ μm and a wavelength-independent complex refractive index $m = 1.55 + i0.05$.

Table S9. The retrieved microphysical properties of Chebychev particles of the fourth degree, along with their PLDR and LR values at 355 and 532nm, that reproduce the PLDR and LR reported in Ohneiser et al., (2020). Also shown is the corresponding cost function of each solution. The solution that minimizes the cost function (Eq. 8 in the manuscript) is highlighted in blue

Simulations-Chebyshev particles of 4th degree								
r_g	u	mri	mrr	PLDR_{355}	PLDR_{532}	LR_{355}	LR_{532}	Cost function
0.40	-0.10	0.010	1.35	19.954	12.879	58.858	92.032	2.259
0.40	-0.10	0.015	1.35	19.974	12.941	81.473	114.518	1.385
0.40	0.05	0.015	1.35	24.898	13.684	70.044	122.151	1.468
0.45	-0.10	0.015	1.35	21.261	15.066	74.416	105.070	0.864
0.30	0.10	0.020	1.40	24.960	13.527	64.104	100.577	0.877
0.45	0.05	0.020	1.40	19.388	12.880	60.810	84.889	2.754
0.30	0.10	0.025	1.40	24.878	13.277	81.276	118.818	1.118
0.50	**0.05**	**0.025**	**1.40**	**20.156**	**14.390**	**80.062**	**96.941**	**0.535**
0.50	0.05	0.030	1.40	19.255	13.932	107.122	120.988	2.470
0.35	0.10	0.040	1.50	18.668	13.196	71.794	82.782	2.307
0.40	0.10	0.045	1.50	19.076	15.003	89.782	90.135	1.653

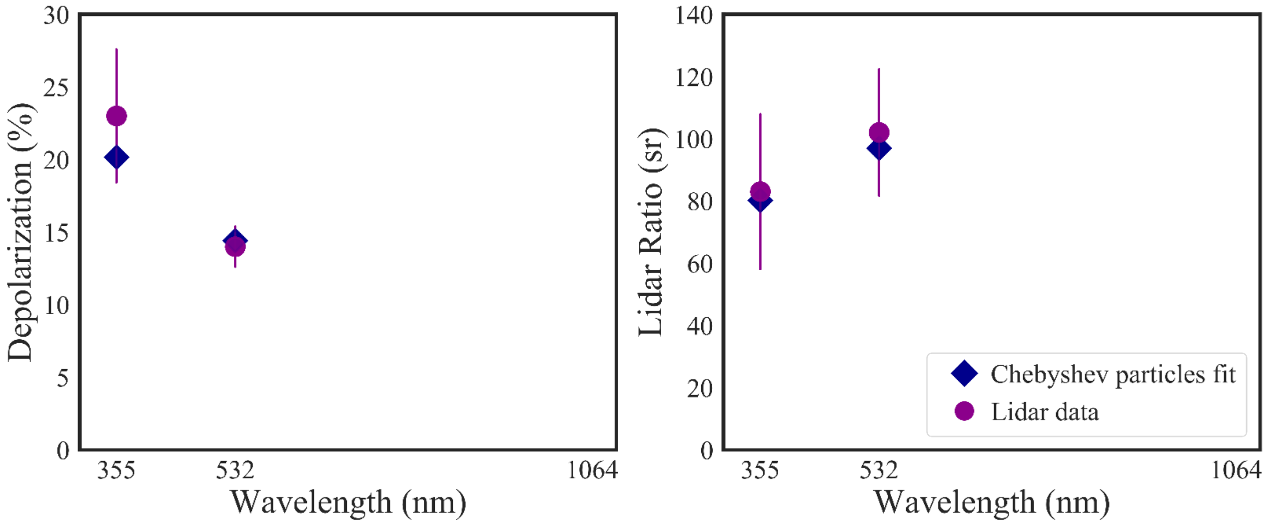

Figure S9. The reproduction of the measured PLDR and LR values, considering Chebyshev particles of fourth degree. Purple circles correspond to measurements performed on 8 January 2020, at Punta Arenas, Chile, while purple lines correspond to the measurement uncertainties. Blue diamonds correspond to simulations performed with the T-matrix code, assuming Chebyshev particles of fourth degree, for the values of deformation parameter u = 0.05, mean geometric radius r_g= 0.5 μm and a wavelength-independent complex refractive index m = 1.4 + i0.025.

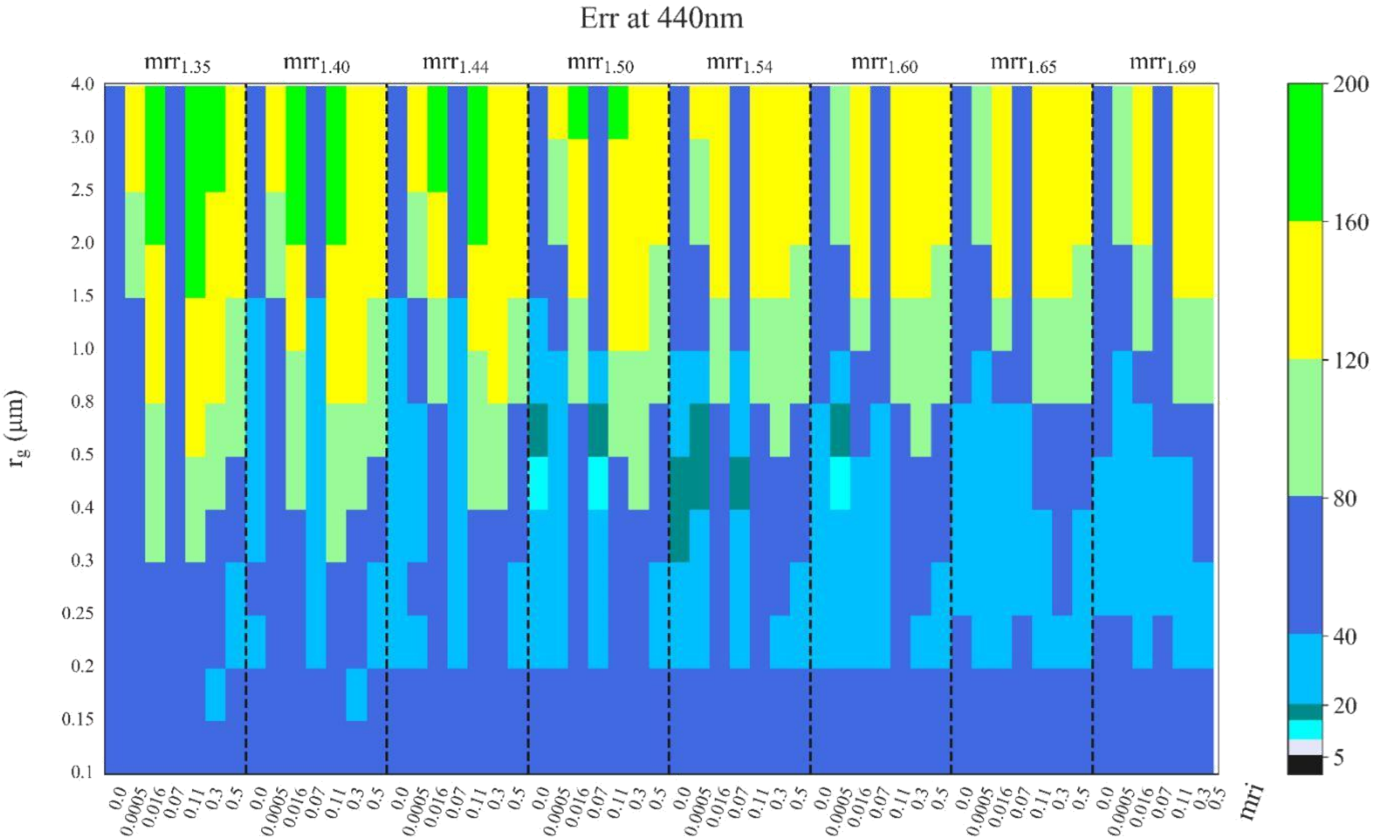

Figure S10. The residual error (Err) of fitting the phase functions at 440 nm of the near-spherical particles presented in the manuscript, with the phase functions calculated with the AERONET non-spherical model, for radius and complex refractive index shown in y- and x-axis, respectively.

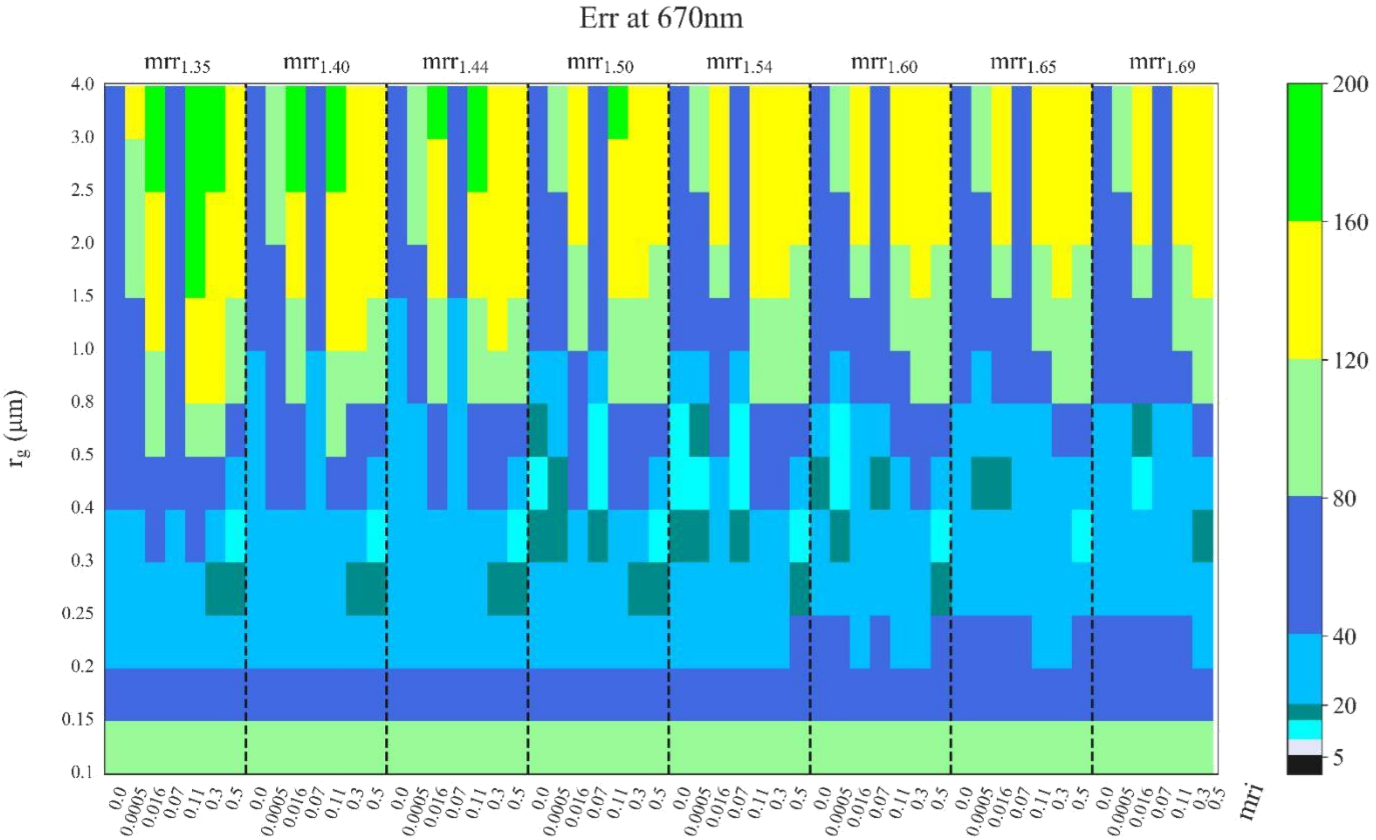

Figure S11. The residual error (Err) of fitting the phase functions at 670 nm of the near-spherical particles presented in the manuscript, with the phase functions calculated with the AERONET non-spherical model, for radius and complex refractive index shown in y- and x-axis, respectively.

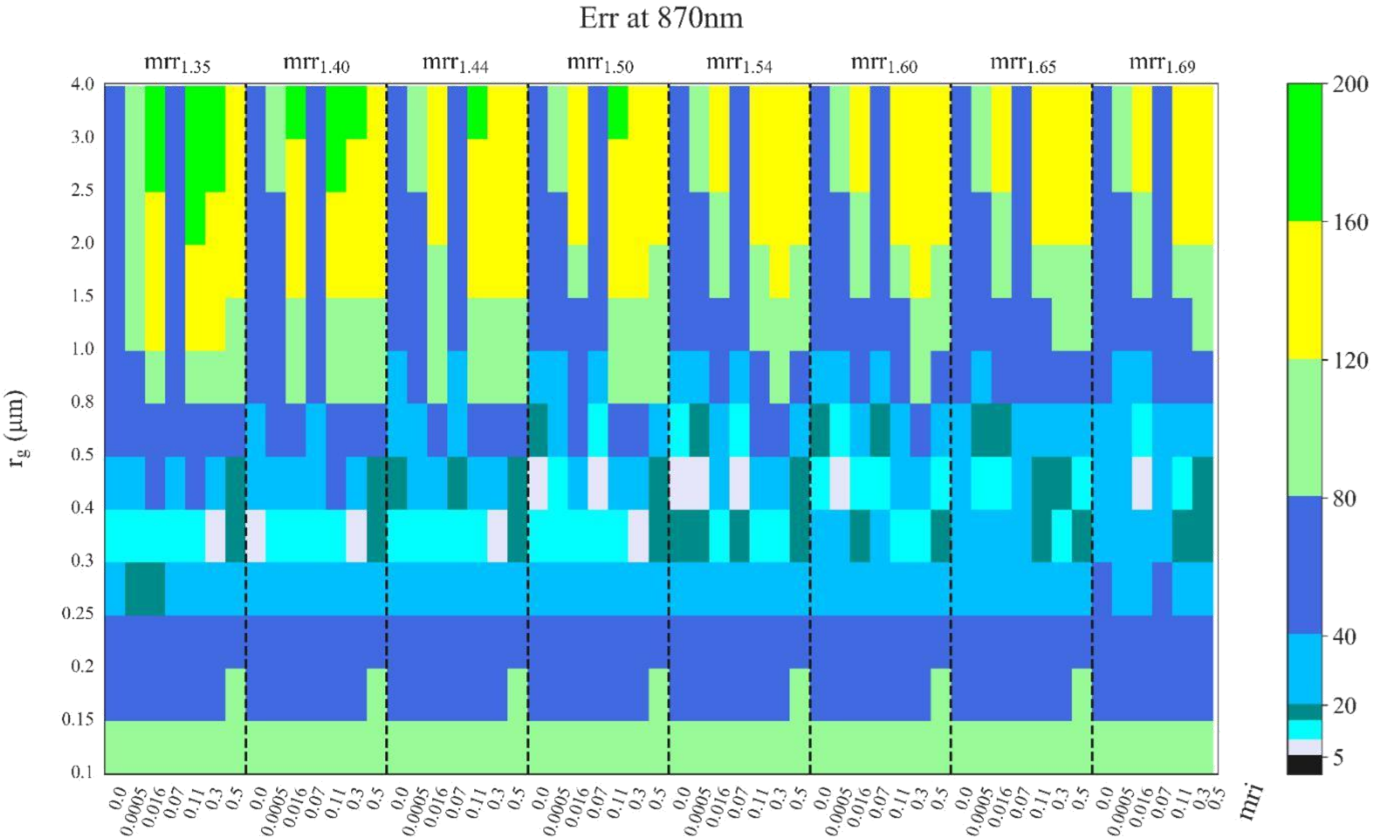

Figure S12. The residual error (Err) of fitting the phase functions at 870 nm of the near-spherical particles presented in the manuscript, with the phase functions calculated with the AERONET non-spherical model, for radius and complex refractive index shown in y- and x-axis, respectively

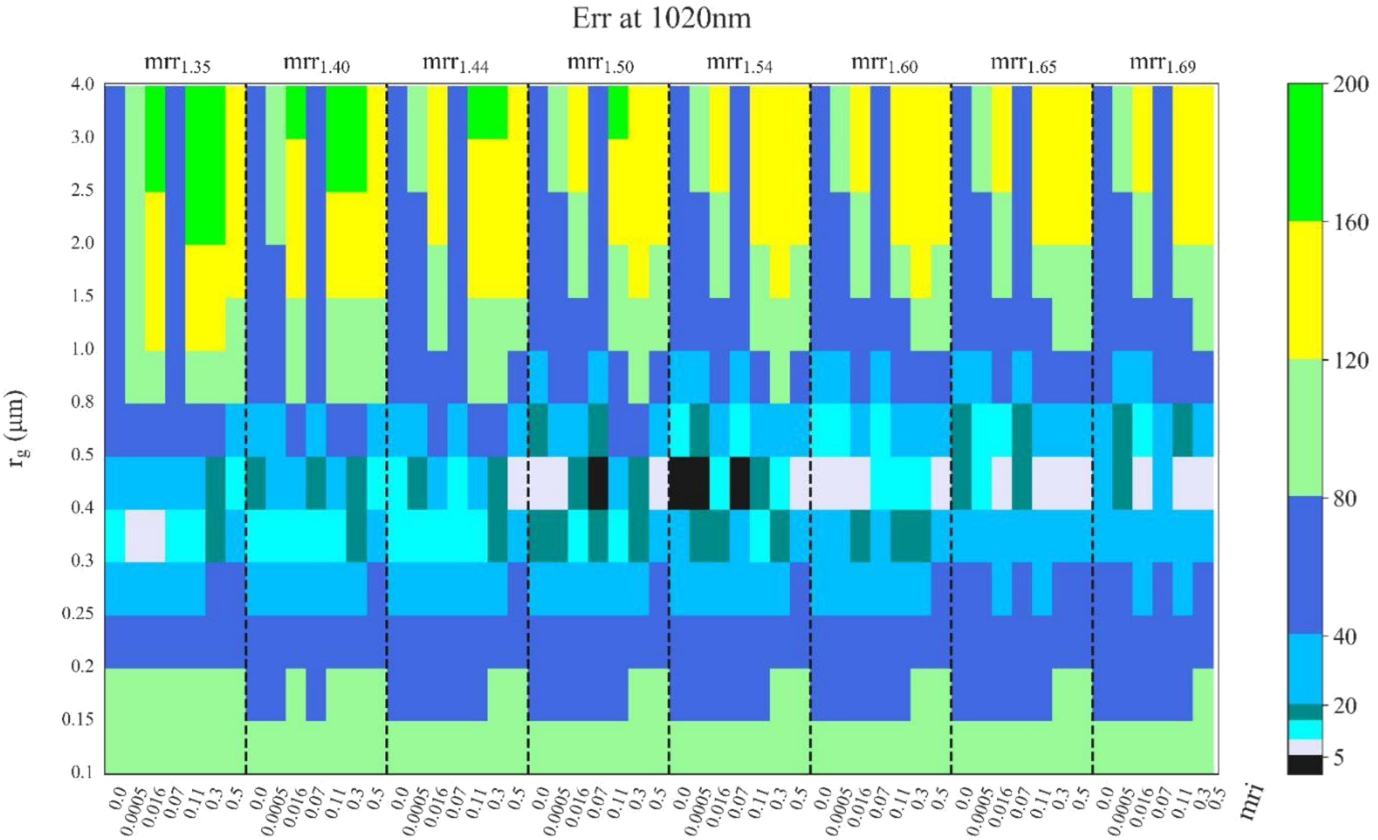

Figure S13. The residual error (Err) of fitting the phase functions at 1020 nm of the near-spherical particles presented in the manuscript, with the phase functions calculated with the AERONET non-spherical model, for radius and complex refractive index shown in y- and x-axis, respectively

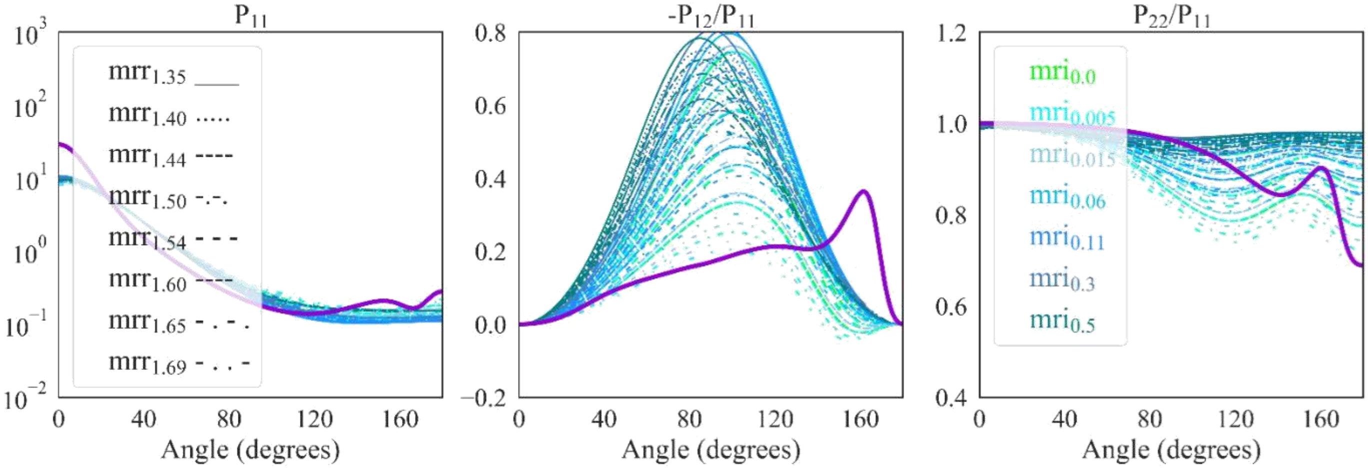

Figure S14. The elements of the scattering matrix at λ = 440nm. Left: P$_{11}$ (phase function), middle: -P$_{12}$/P$_{11}$ (degree of linear polarization), right: P$_{22}$/P$_{11}$. Purple lines in the plots: calculations considering the near-spherical particle properties derived for the stratospheric smoke particles from the Canadian fires, with mean axial ratio ε_s = 1.3, mono-modal, log-normal size distribution with mean geometric radius r_g = 0.25 μm, geometric standard deviation σ_g = 0.4, and complex refractive index m = 1.55 – i0.03. Blue lines in the plots: calculations using the AERONET non-spherical model, mono-modal, log-normal size distributions with r_g = 0.1 μm and refractive indices of mrr = 1.35, 1.40, 1.44, 1.50, 1.54, 1.60, 1.65, 1.69 for the real part (different line styles in the plot) and mri = 0.0, 0.005, 0.015, 0.06, 0.11, 0.3, 0.5 for the imaginary part (different line colors in the plot).

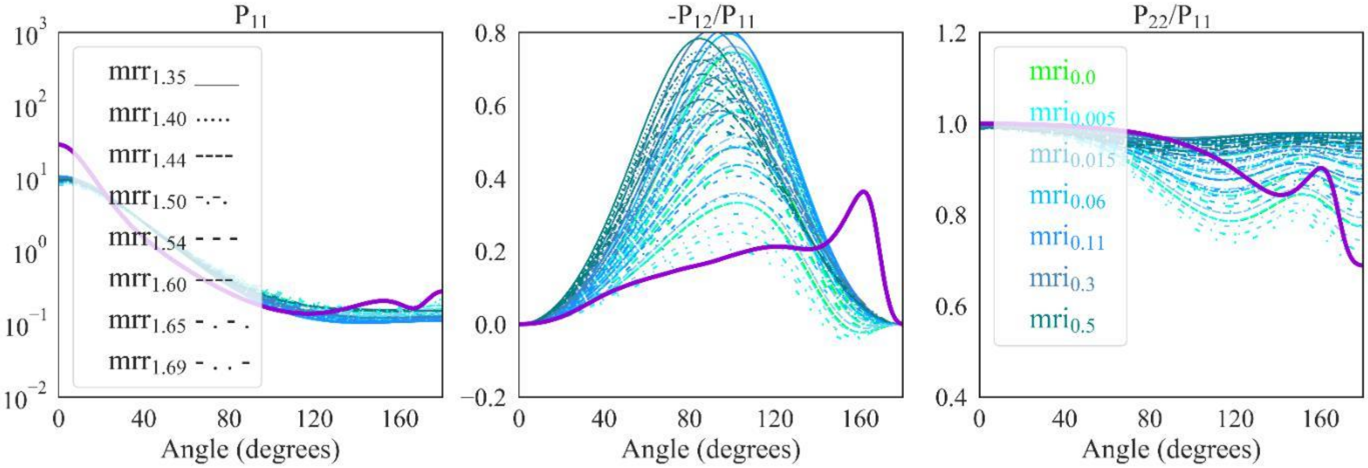

Figure S15. Same as Fig. S14, with the calculations using the AERONET non-spherical model, performed for mono-modal log-normal size distributions with mean geometric radius r_g = 0.15 μm.

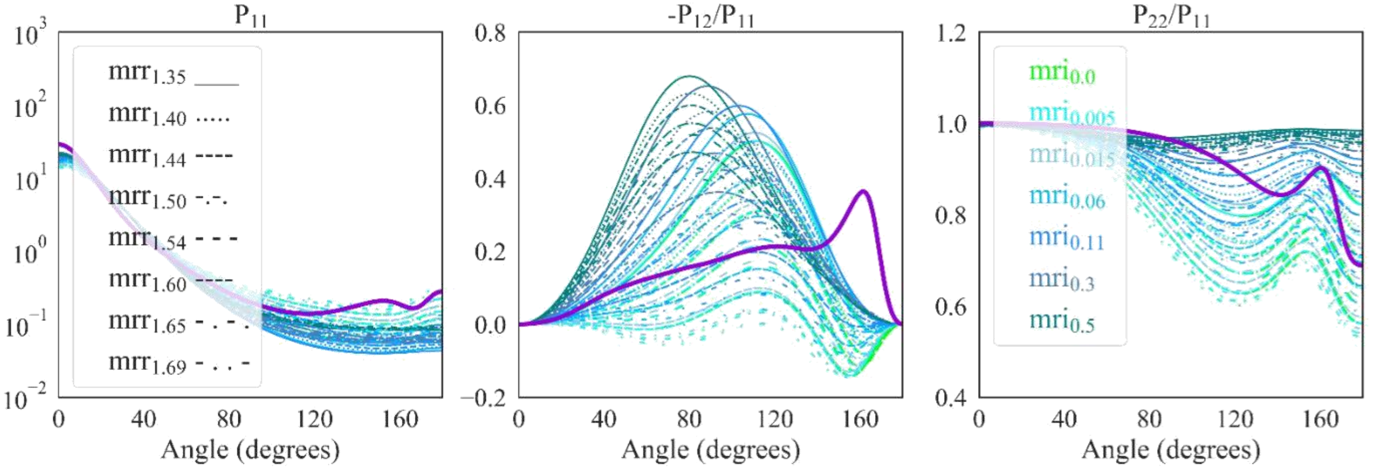

Figure S16. Same as Fig. S14, with the calculations using the AERONET non-spherical model, performed for mono-modal log-normal size distributions with mean geometric radius r_g = 0.2 μm

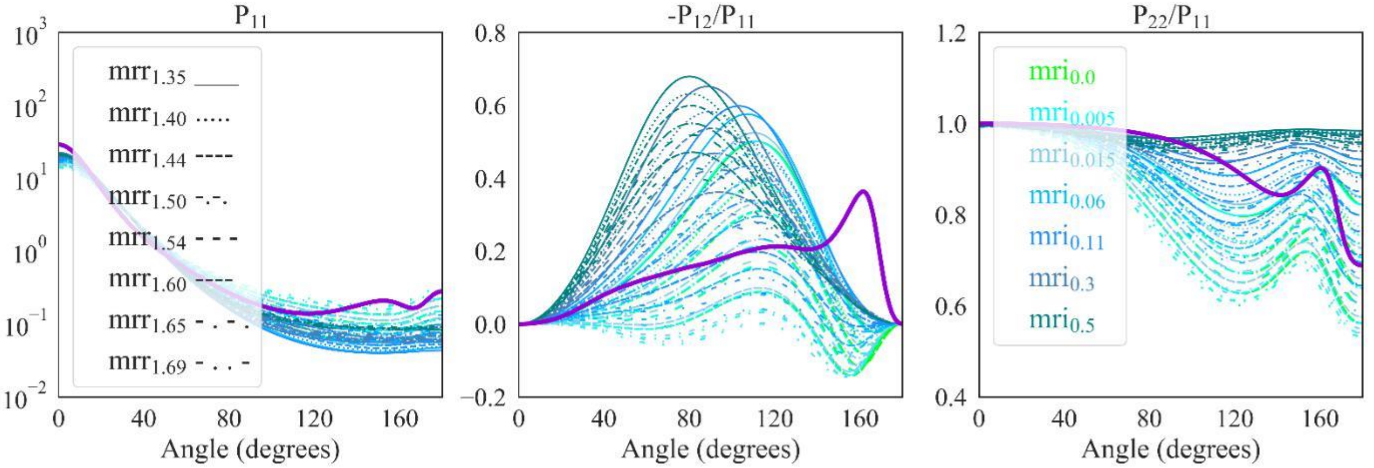

Figure S17. Same as Fig. S14, with the calculations using the AERONET non-spherical model, performed for mono-modal log-normal size distributions with mean geometric radius r_g = 0.25 μm

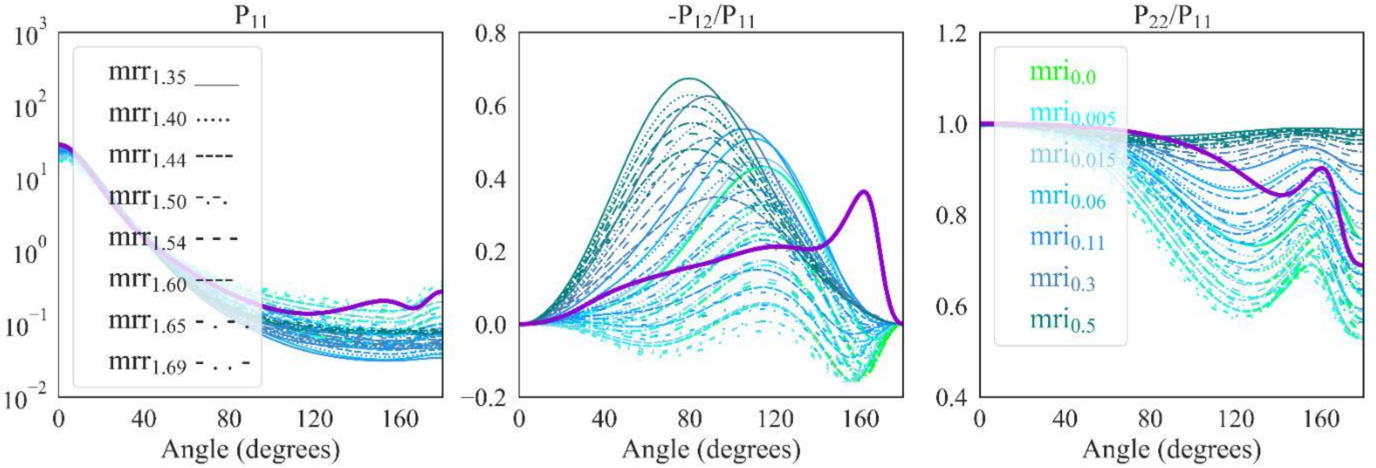

Figure S18. Same as Fig. S14, with the calculations using the AERONET non-spherical model, performed for mono-modal log-normal size distributions with mean geometric radius r_g = 0.3 μm.

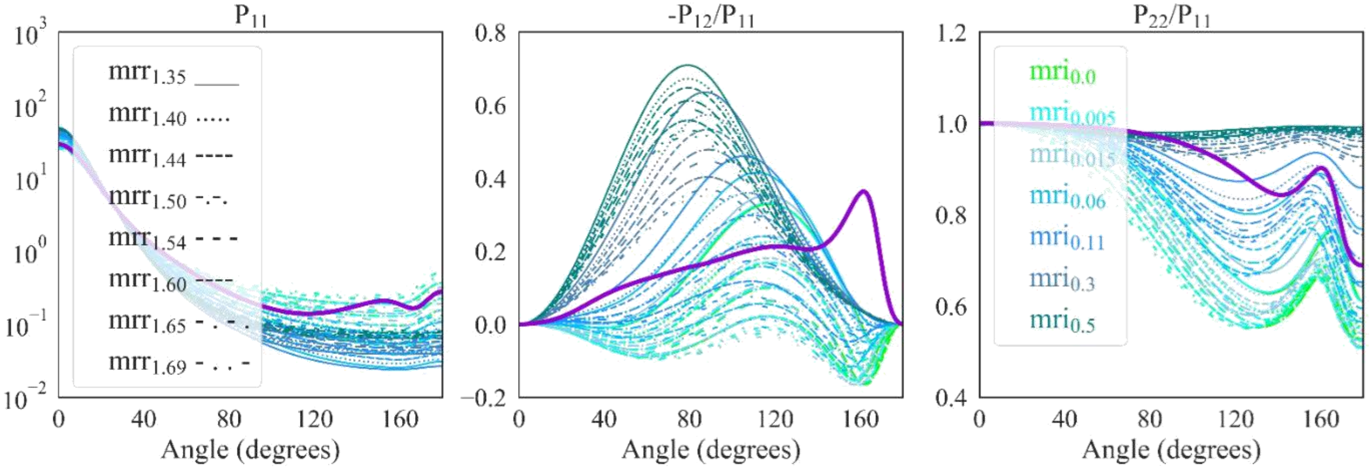

Figure S19. Same as Fig. S14, with the calculations using the AERONET non-spherical model, performed for mono-modal log-normal size distributions with mean geometric radius r_g = 0.4 μm.

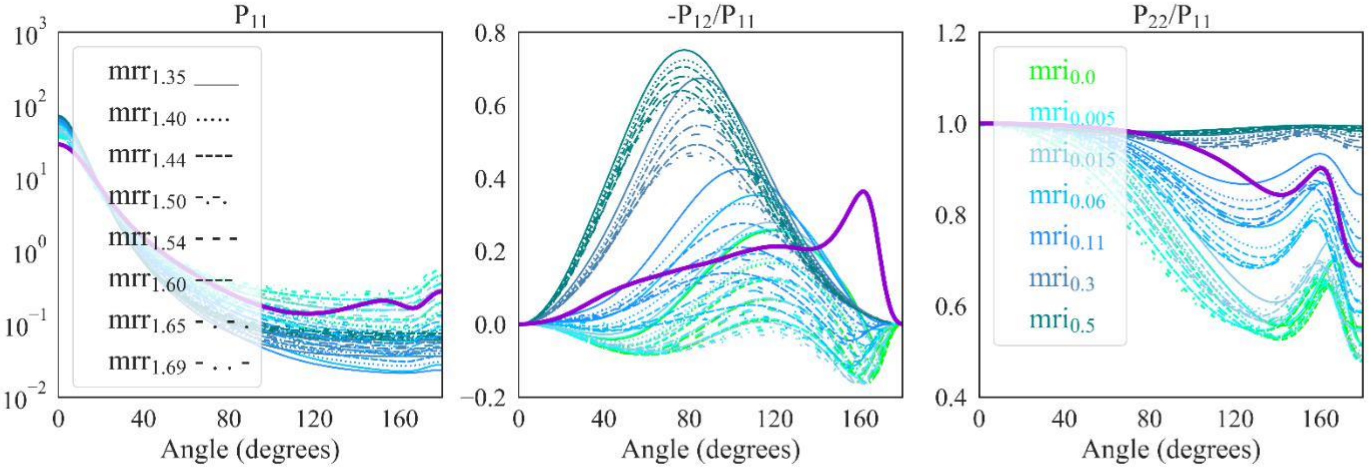

Figure S20. Same as Fig. S14, with the calculations using the AERONET non-spherical model, performed for mono-modal log-normal size distributions with mean geometric radius r_g = 0.5 μm.

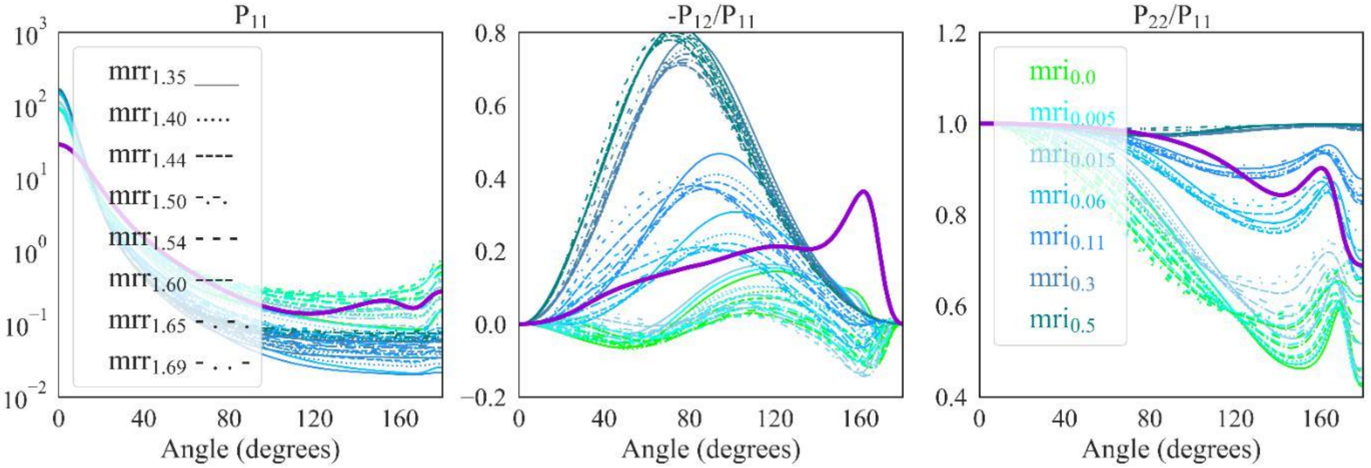

Figure S21. Same as Fig. S14, with the calculations using the AERONET non-spherical model, performed for mono-modal log-normal size distributions with mean geometric radius r_g = 0.8 μm.

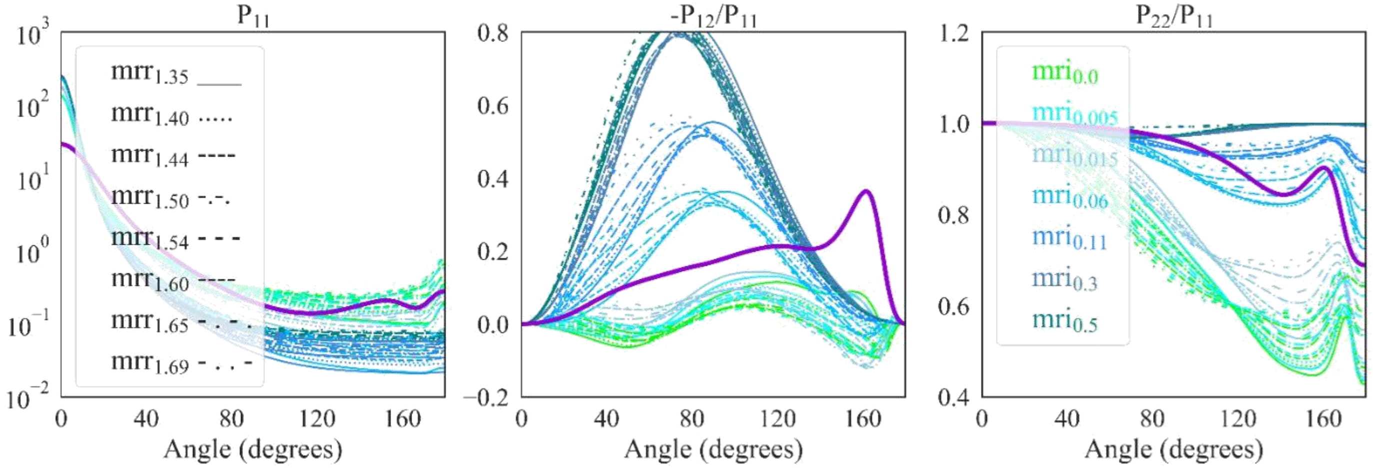

Figure S22. Same as Fig. S14, with the calculations using the AERONET non-spherical model, performed for mono-modal log-normal size distributions with mean geometric radius r_g = 1.0 μm.

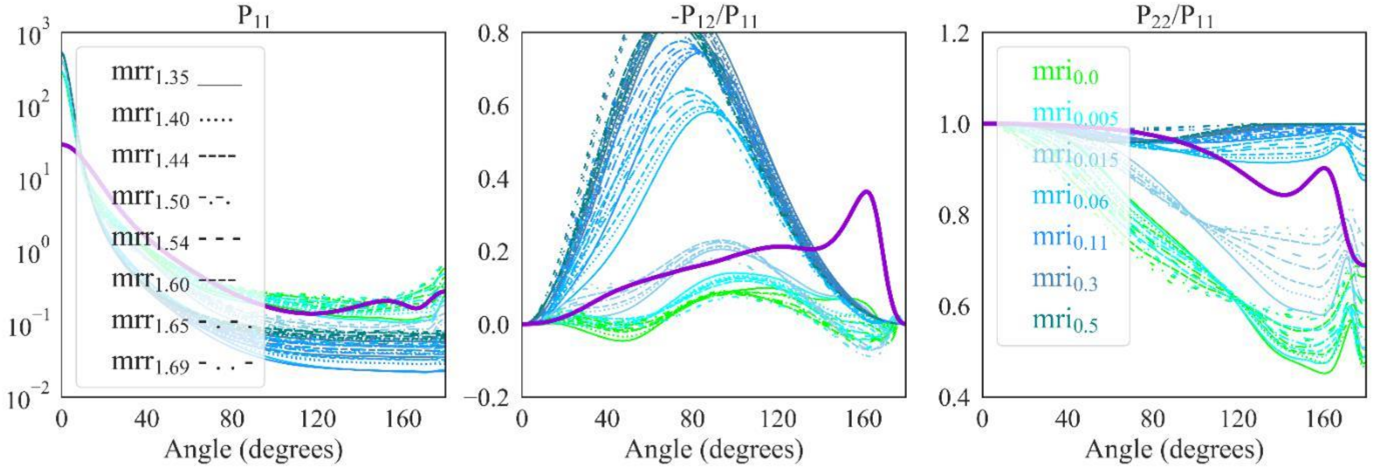

Figure S23. Same as Fig. S14, with the calculations using the AERONET non-spherical model, performed for mono-modal log-normal size distributions with mean geometric radius r_g = 1.5 μm.

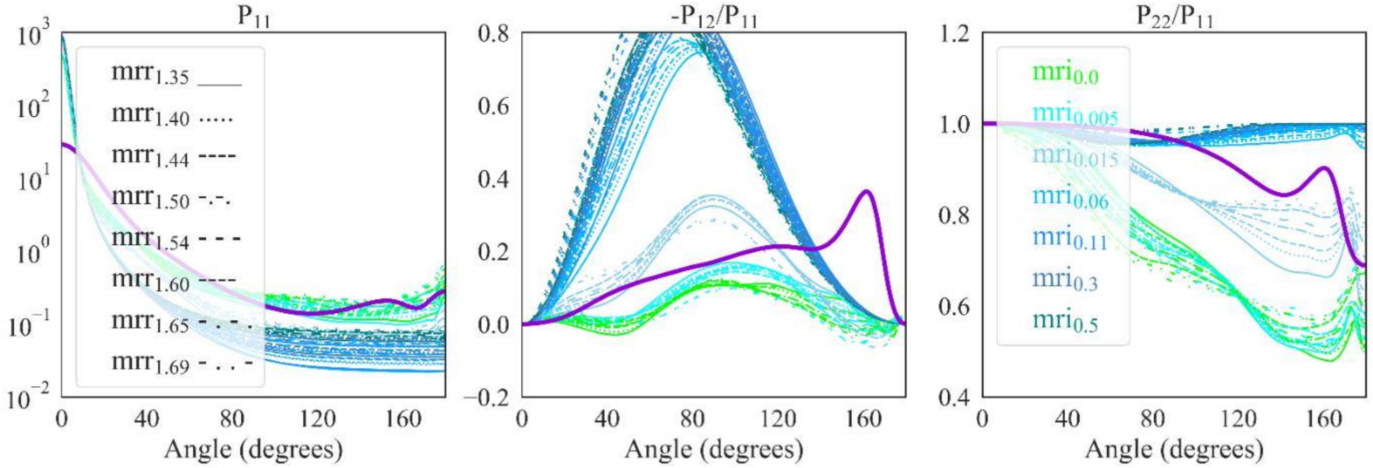

Figure S24. Same as Fig. S14, with the calculations using the AERONET non-spherical model, performed for mono-modal log-normal size distributions with mean geometric radius r_g = 2.0 μm.

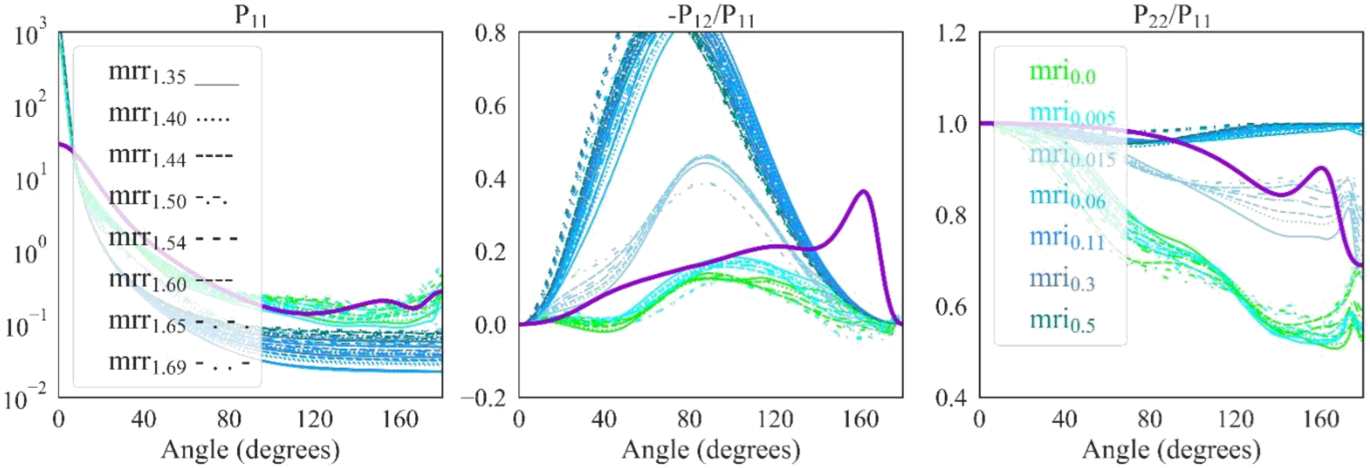

Figure S25. Same as Fig. S14, with the calculations using the AERONET non-spherical model, performed for mono-modal log-normal size distributions with mean geometric radius r_g = 2.5 µm.

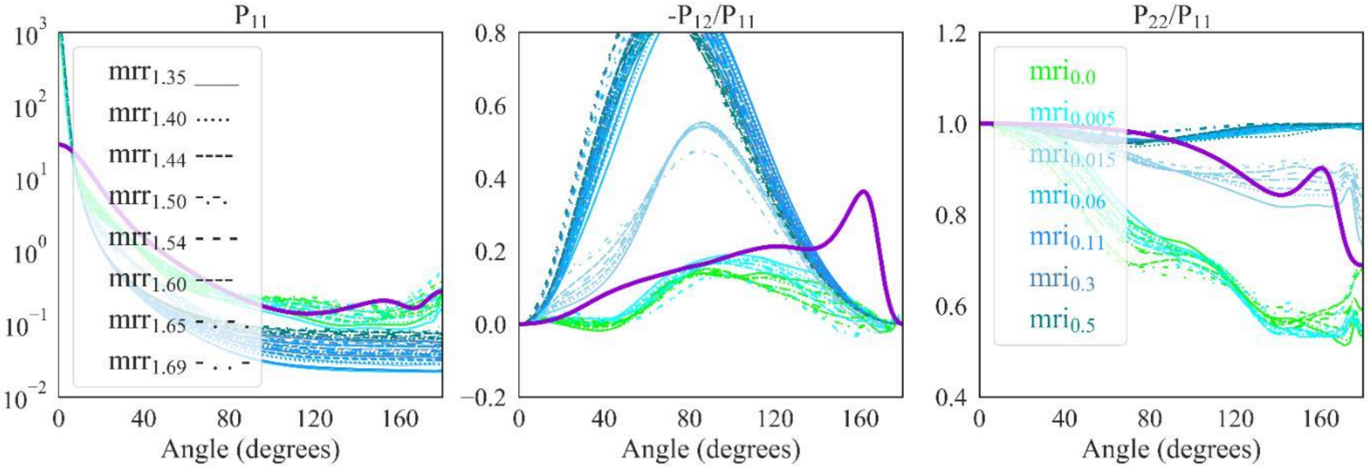

Figure S26. Same as Fig. S14, with the calculations using the AERONET non-spherical model, performed for mono-modal log-normal size distributions with mean geometric radius r_g = 3.0 µm.

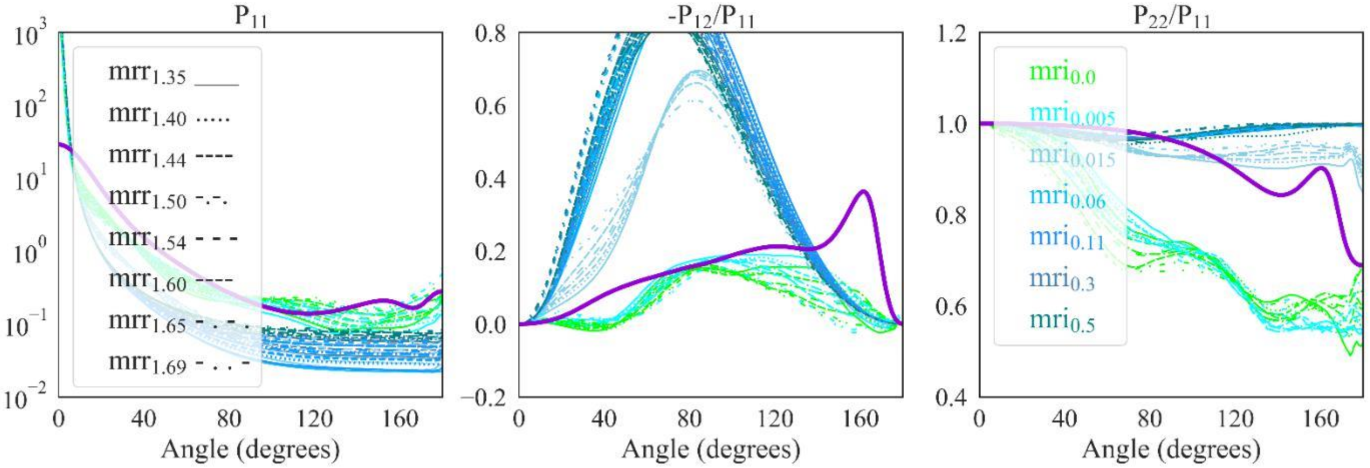

Figure S27. Same as Fig. S14, with the calculations using the AERONET non-spherical model, performed for mono-modal log-normal size distributions with mean geometric radius r_g = 4.0 μm.

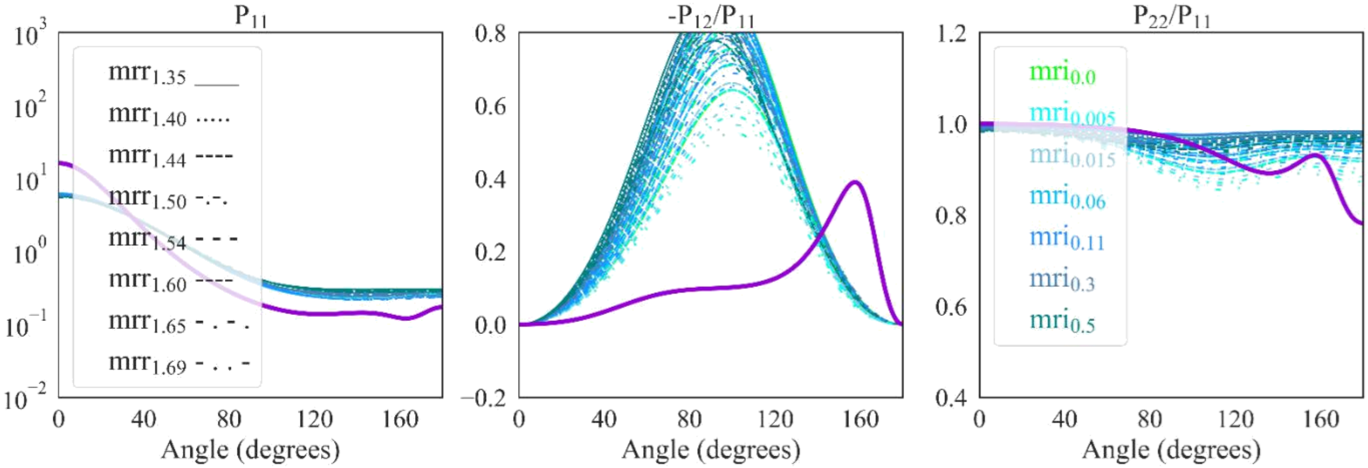

Figure S28. The elements of the scattering matrix at λ = 670 nm. Left: P_{11} (phase function), middle: $-P_{12}/P_{11}$ (degree of linear polarization), right: P_{22}/P_{11}. Purple lines in the plots: calculations considering the near-spherical particle properties derived for the stratospheric smoke particles from the Canadian fires, with mean axial ratio ε_s = 1.3, mono-modal, log-normal size distribution with mean geometric radius r_g = 0.25 μm, mean geometric standard deviation σ_g = 0.4, and complex refractive index m = 1.55 – i0.03. Blue lines in the plots: calculations using the AERONET non-spherical model, mono-modal, log-normal size distributions with r_g = 0.1 μm and refractive indices of mrr = 1.35, 1.40, 1.44, 1.50, 1.54, 1.60, 1.65, 1.69 for the real part (different line styles in the plot) and mri = 0.0, 0.005, 0.015, 0.06, 0.11, 0.3, 0.5 for the imaginary part (different line colors in the plot).

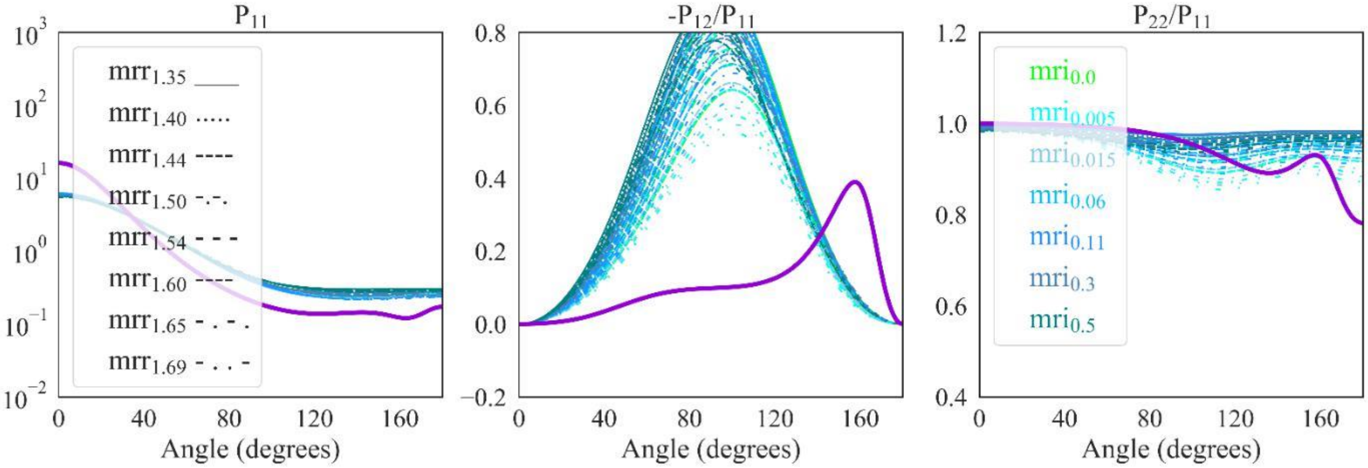

Figure S29. Same as Fig. S28, with the calculations using the AERONET non-spherical model, performed for mono-modal log-normal size distributions with mean geometric radius r_g = 0.15 μm

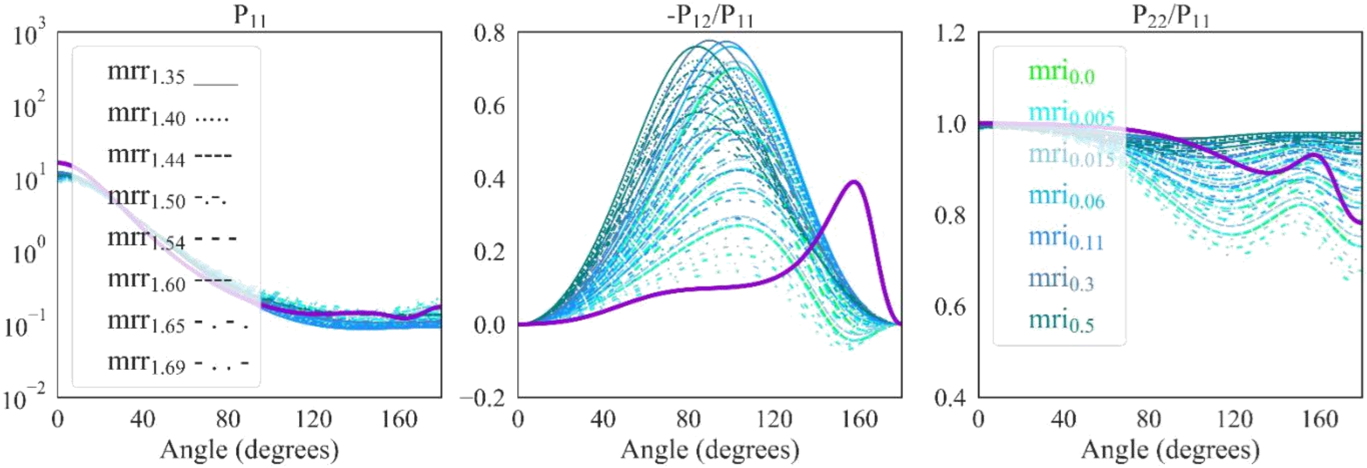

Figure S30. Same as Fig. S28, with the calculations using the AERONET non-spherical model, performed for mono-modal log-normal size distributions with mean geometric radius r_g = 0.2 μm.

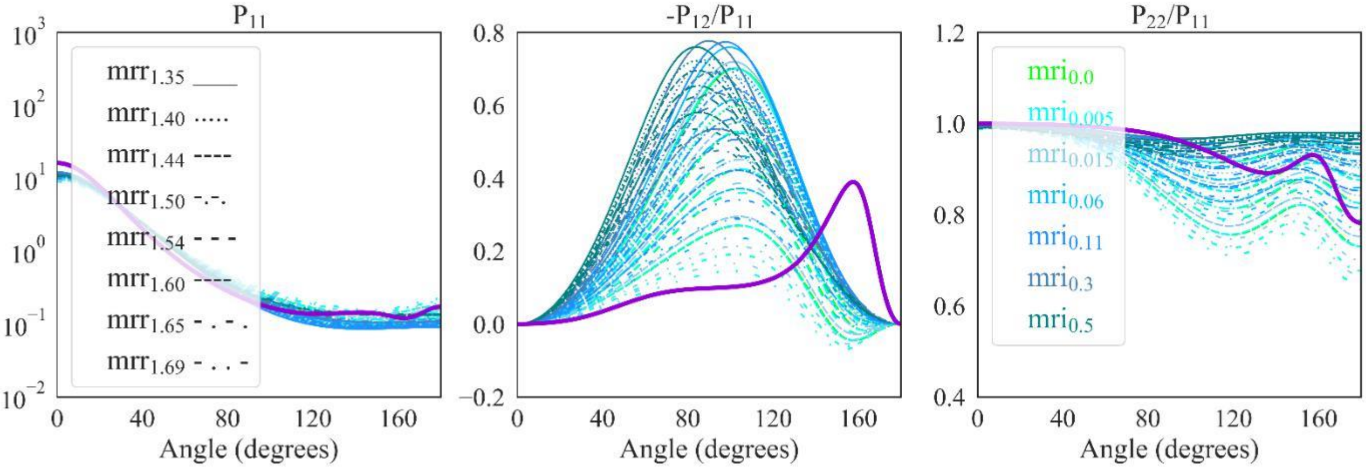

Figure S31. Same as Fig. S28, with the calculations using the AERONET non-spherical model, performed for mono-modal log-normal size distributions with mean geometric radius r_g = 0.25 μm.

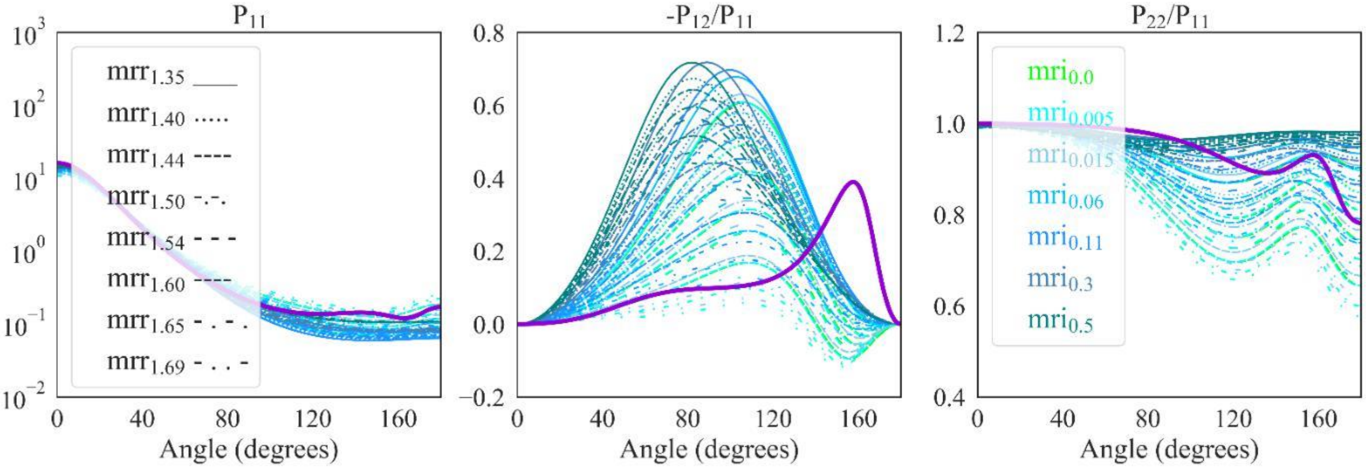

Figure S32. Same as Fig. S28, with the calculations using the AERONET non-spherical model, performed for mono-modal log-normal size distributions with mean geometric radius r_g = 0.3 μm.

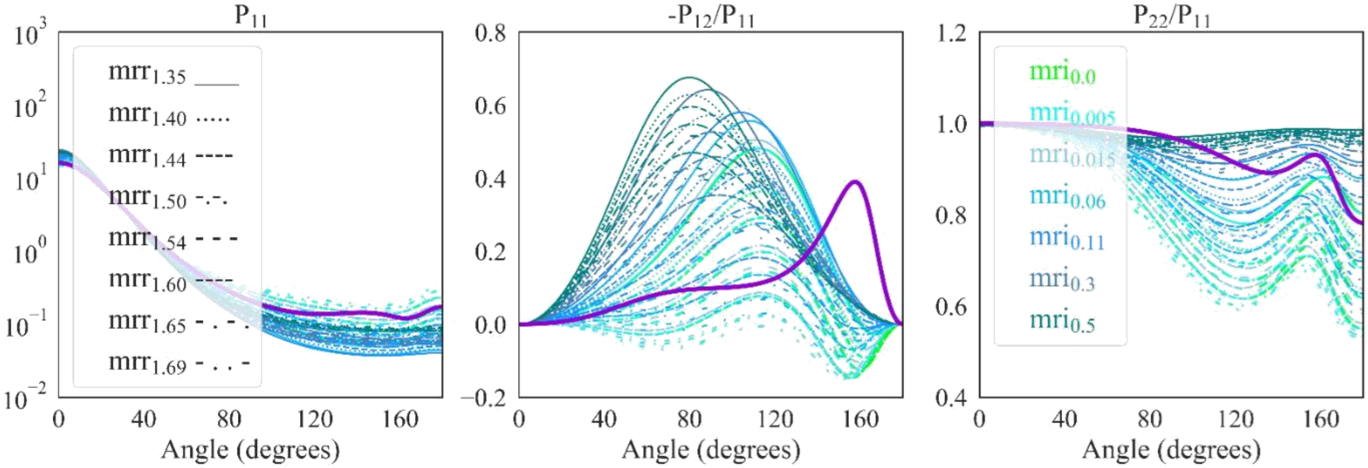

Figure S33. Same as Fig. S28, with the calculations using the AERONET non-spherical model, performed for mono-modal log-normal size distributions with mean geometric radius r_g = 0.4 μm.

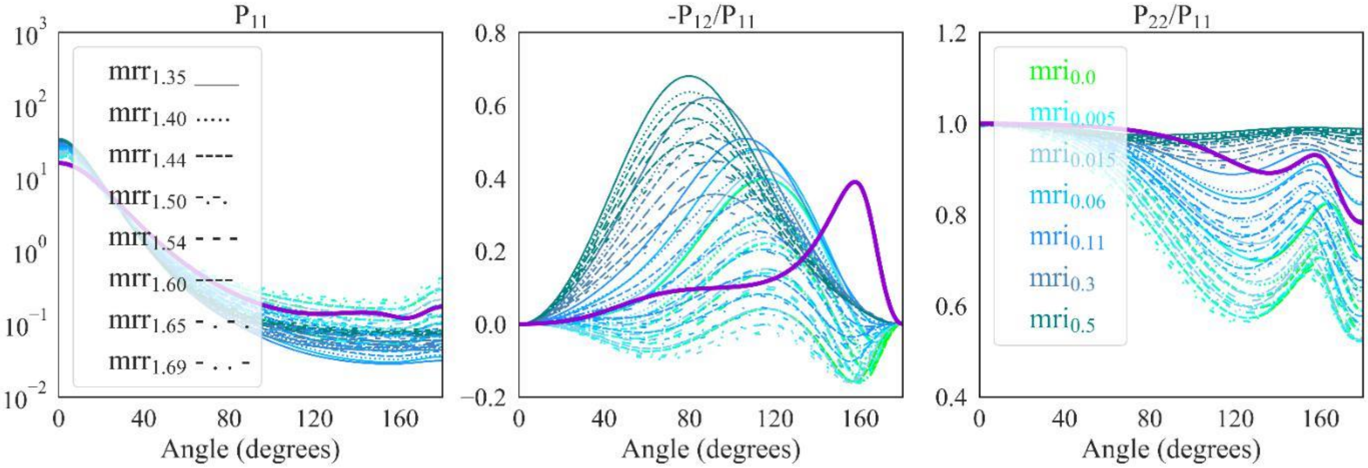

Figure S34. Same as Fig. S28, with the calculations using the AERONET non-spherical model, performed for mono-modal log-normal size distributions with mean geometric radius r_g = 0.5 μm.

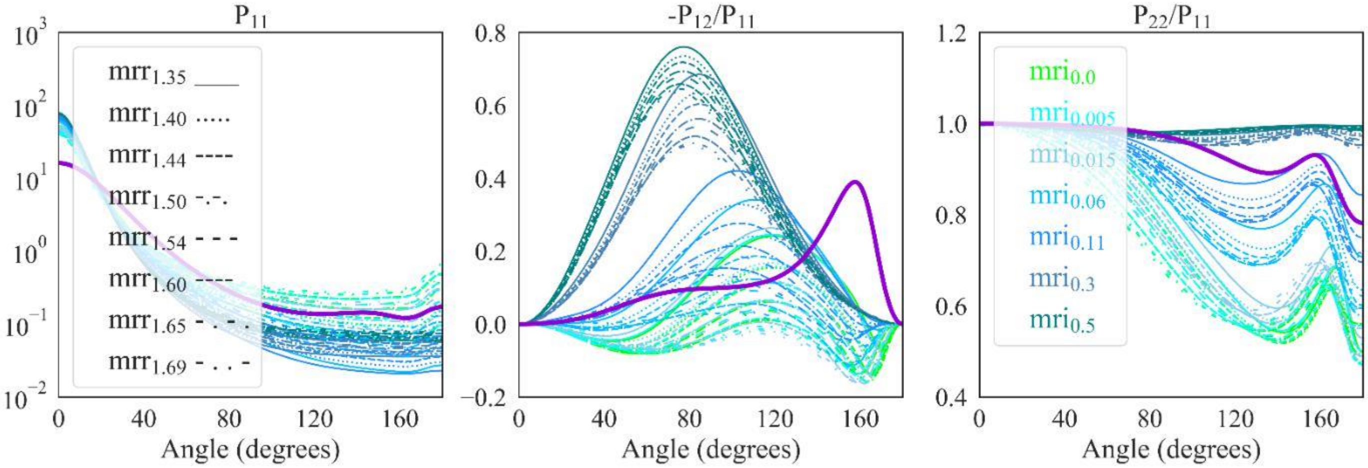

Figure S35. Same as Fig. S28, with the calculations using the AERONET non-spherical model, performed for mono-modal log-normal size distributions with mean geometric radius r_g = 0.8 μm.

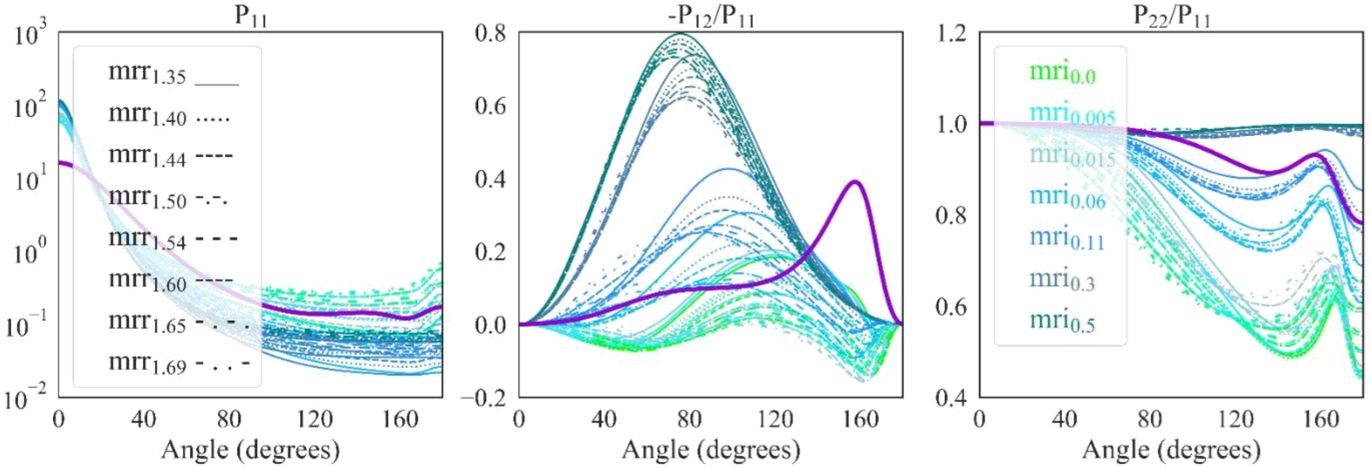

Figure S36. Same as Fig. S28, with the calculations using the AERONET non-spherical model, performed for mono-modal log-normal size distributions with mean geometric radius r_g = 1.0 μm.

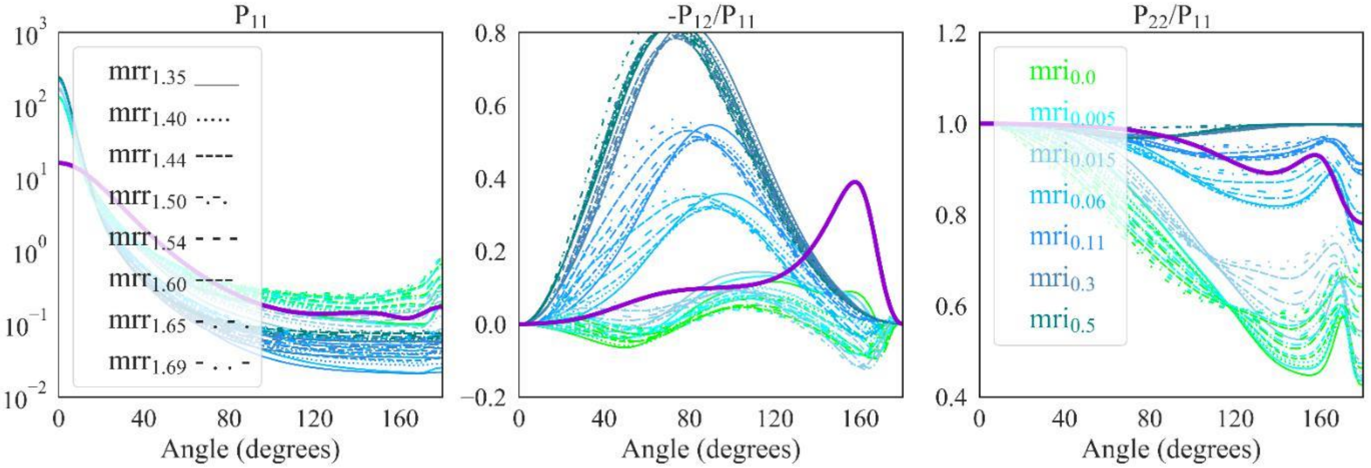

Figure S37. Same as Fig. S28, with the calculations using the AERONET non-spherical model, performed for mono-modal log-normal size distributions with mean geometric radius r_g = 1.5 μm.

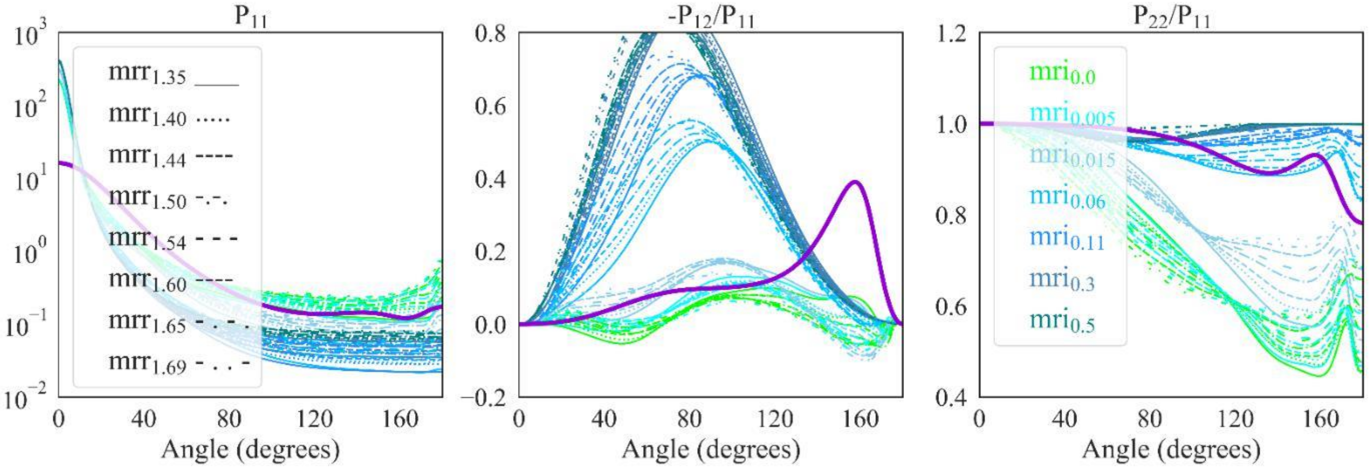

Figure S38. Same as Fig. S28, with the calculations using the AERONET non-spherical model, performed for mono-modal log-normal size distributions with mean geometric radius r_g = 2.0 μm.

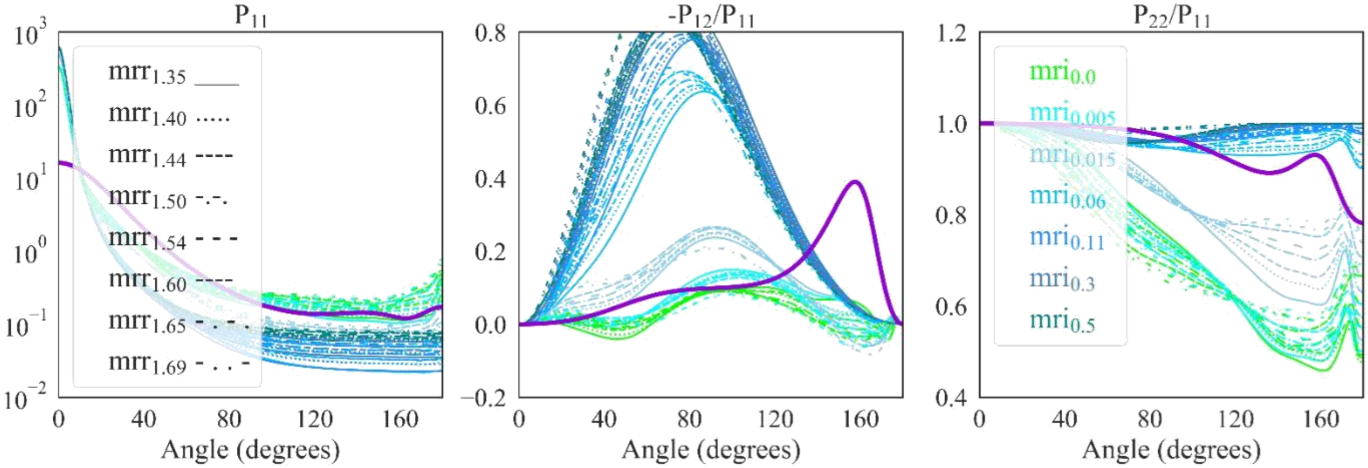

Figure S39. Same as Fig. S28, with the calculations using the AERONET non-spherical model, performed for mono-modal log-normal size distributions with mean geometric radius r_g = 2.5 μm.

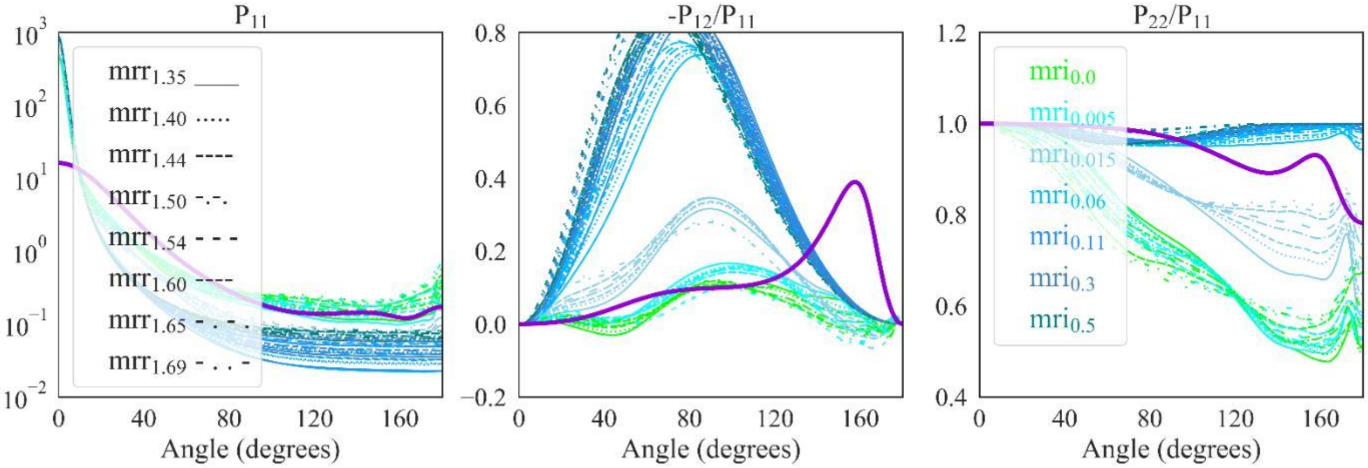

Figure S40. Same as Fig. S28, with the calculations using the AERONET non-spherical model, performed for mono-modal log-normal size distributions with mean geometric radius r_g = 3.0 μm.

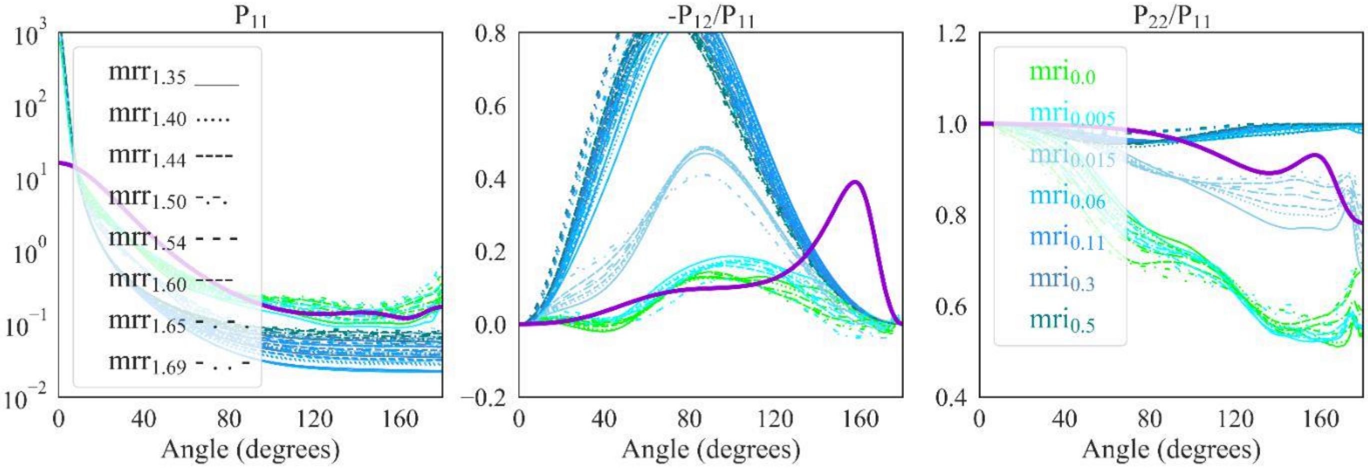

Figure S41. Same as Fig. S28, with the calculations using the AERONET non-spherical model, performed for mono-modal log-normal size distributions with mean geometric radius r_g = 4.0 µm.

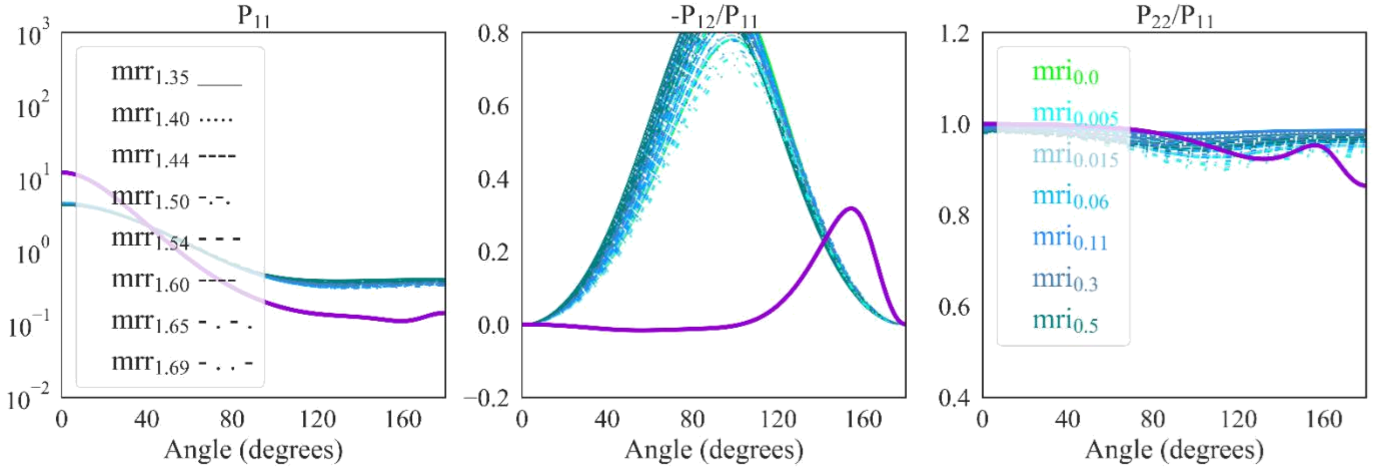

Figure S42. The elements of the scattering matrix at λ = 870 nm. Left: P11 (phase function), middle: -P12/P11 (degree of linear polarization), right: P22/P11. Purple lines in the plots: calculations considering the near-spherical particle properties derived for the stratospheric smoke particles from the Canadian fires, with mean axial ratio ε_s = 1.3, mono-modal, log-normal size distribution with mean geometric radius r_g = 0.25 μm, mean geometric standard deviation σ_g = 0.4, and complex refractive index m = 1.55 – i0.03. Blue lines in the plots: calculations using the AERONET non-spherical model, mono-modal, log-normal size distributions with r_g = 0.1μm and refractive indices of mrr = 1.35, 1.40, 1.44, 1.50, 1.54, 1.60, 1.65, 1.69 for the real part (different line styles in the plot) and mri = 0.0, 0.005, 0.015, 0.06, 0.11, 0.3, 0.5 for the imaginary part (different line colors in the plot).

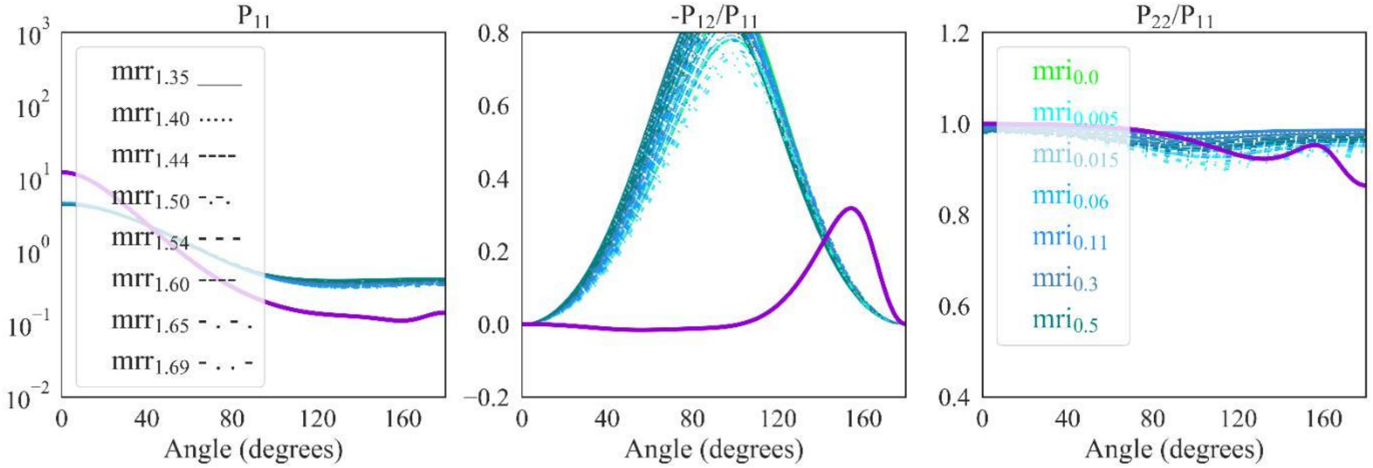

Figure S43. Same as Fig. S42, with the calculations using the AERONET non-spherical model, performed for mono-modal log-normal size distributions with mean geometric radius r_g = 0.15 μm.

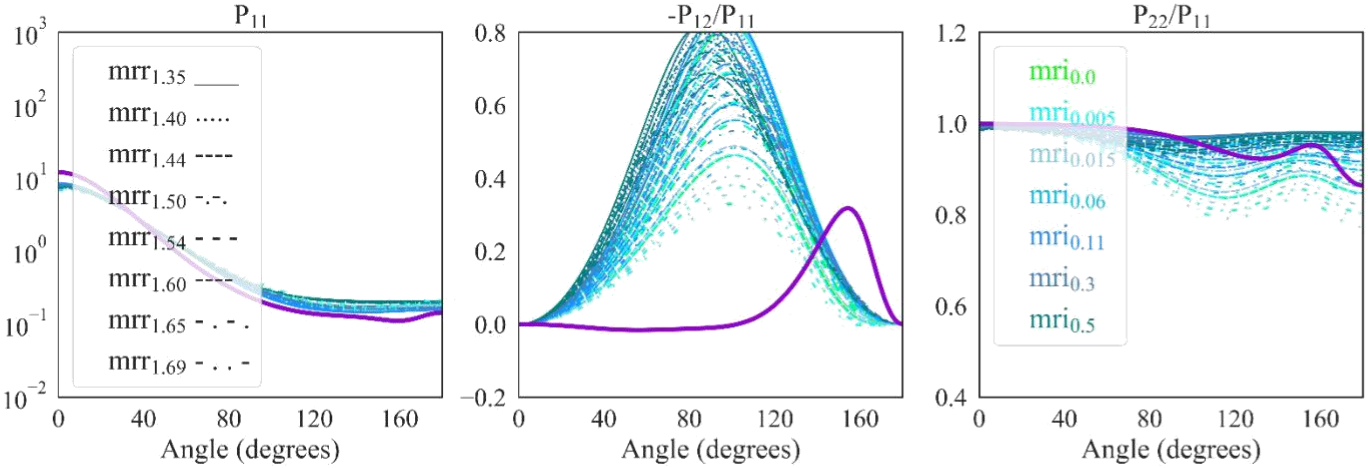

Figure S44. Same as Fig. S42, with the calculations using the AERONET non-spherical model, performed for mono-modal log-normal size distributions with mean geometric radius r_g = 0.2 μm.

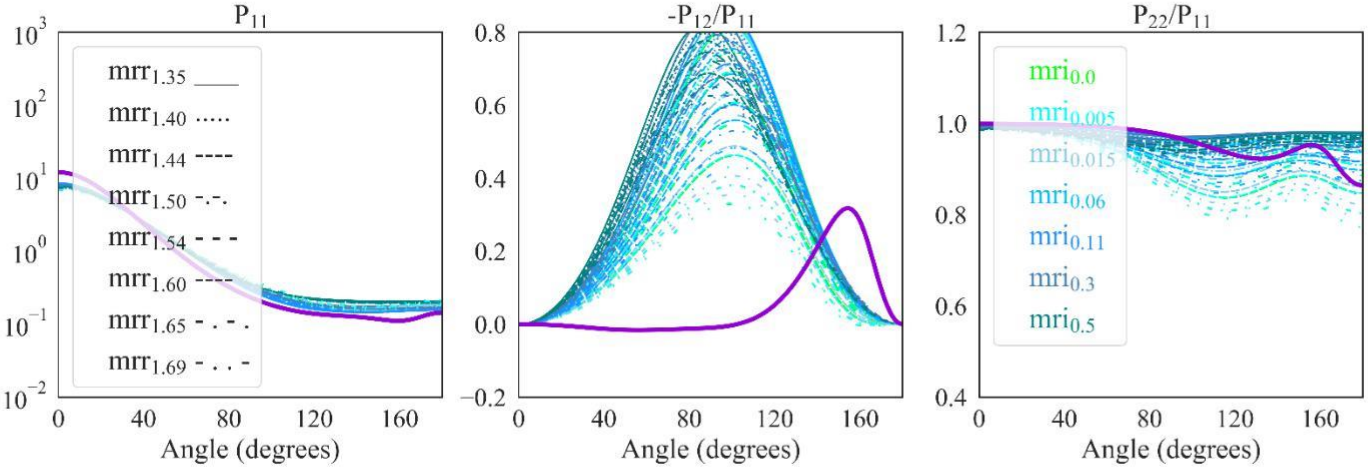

Figure S45. Same as Fig. S42, with the calculations using the AERONET non-spherical model, performed for mono-modal log-normal size distributions with mean geometric radius r_g = 0.25 μm.

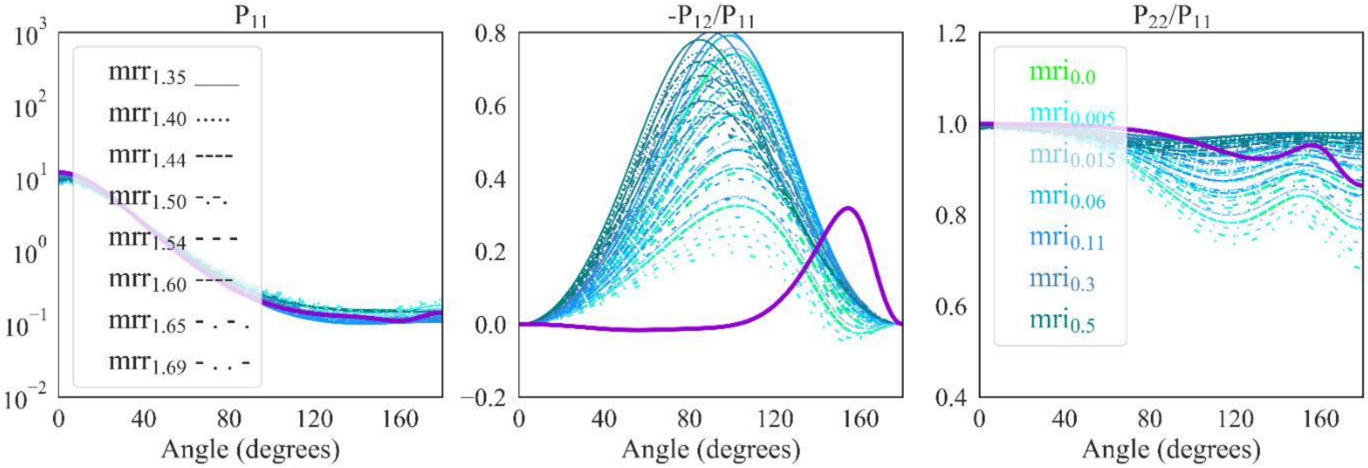

Figure S46. Same as Fig. S42, with the calculations using the AERONET non-spherical model, performed for mono-modal log-normal size distributions with mean geometric radius r_g = 0.3 μm.

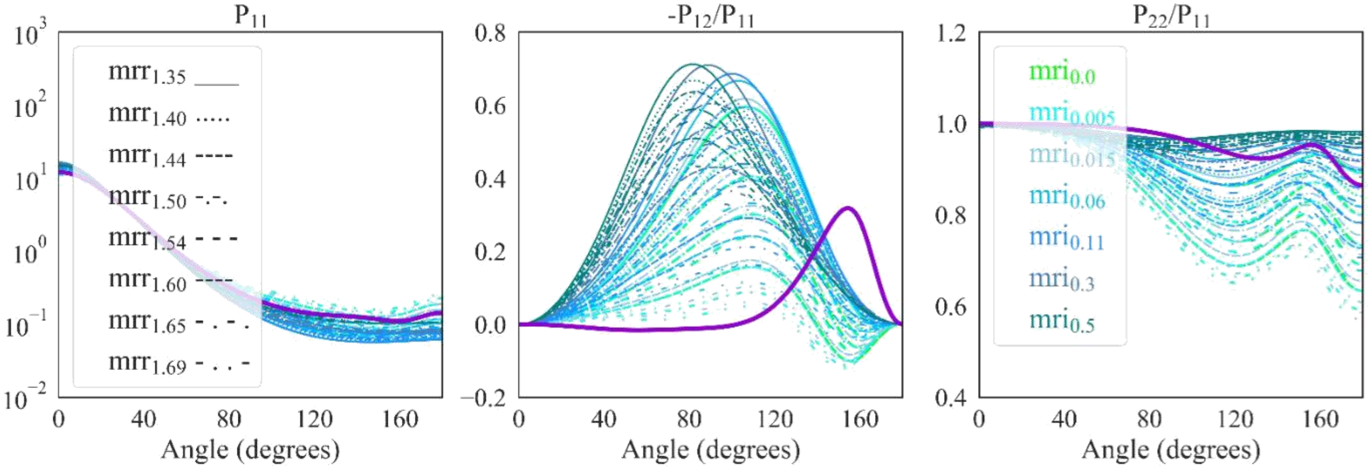

Figure S47. Same as Fig. S42, with the calculations using the AERONET non-spherical model, performed for mono-modal log-normal size distributions with mean geometric radius r_g = 0.4 μm.

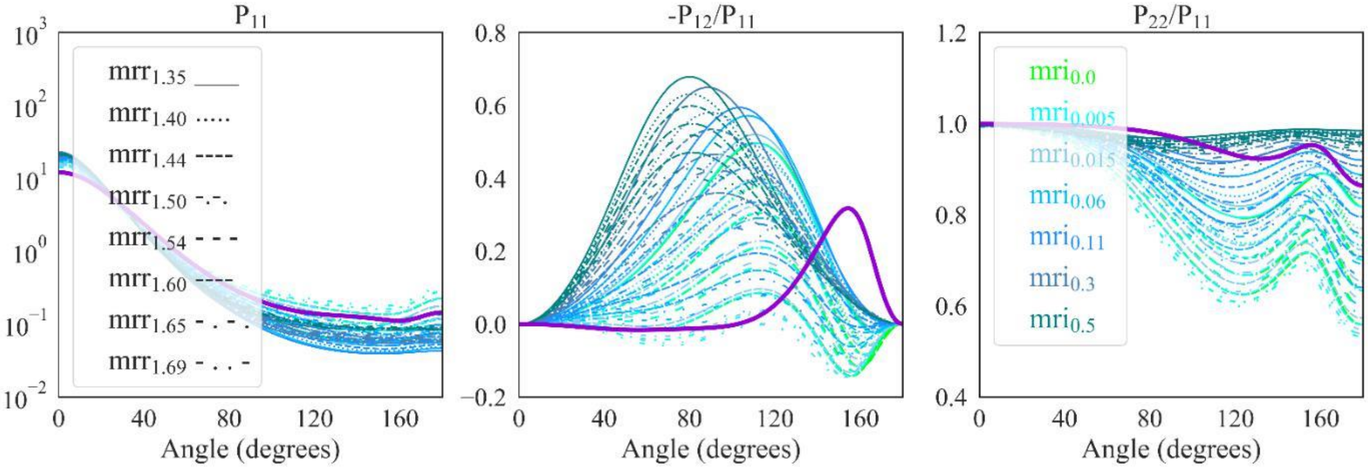

Figure S48. Same as Fig. S42, with the calculations using the AERONET non-spherical model, performed for mono-modal log-normal size distributions with mean geometric radius r_g = 0.5 μm.

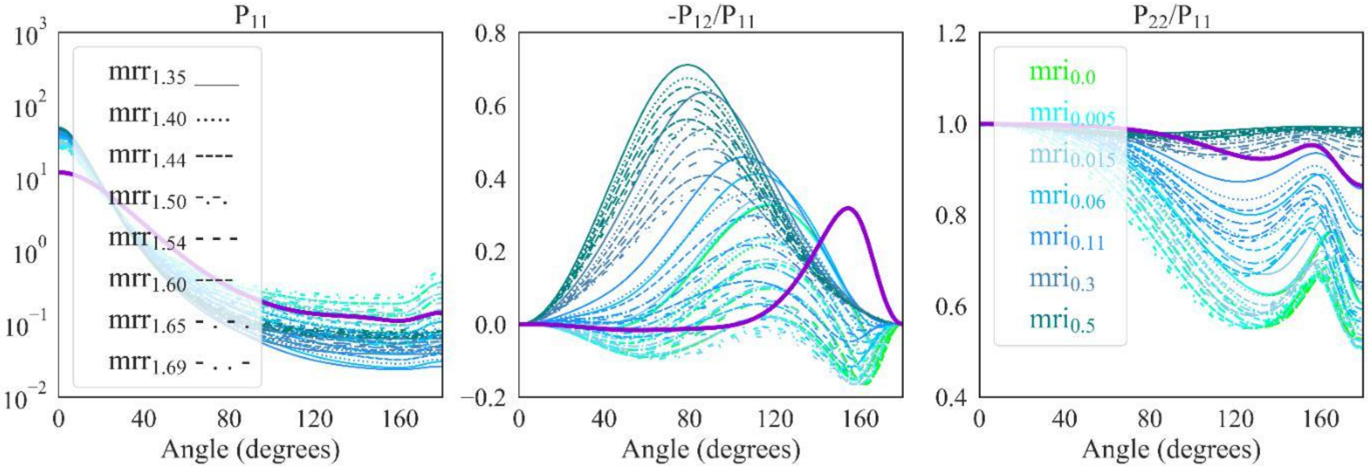

Figure S49. Same as Fig. S42, with the calculations using the AERONET non-spherical model, performed for mono-modal log-normal size distributions with mean geometric radius r_g = 0.8 μm.

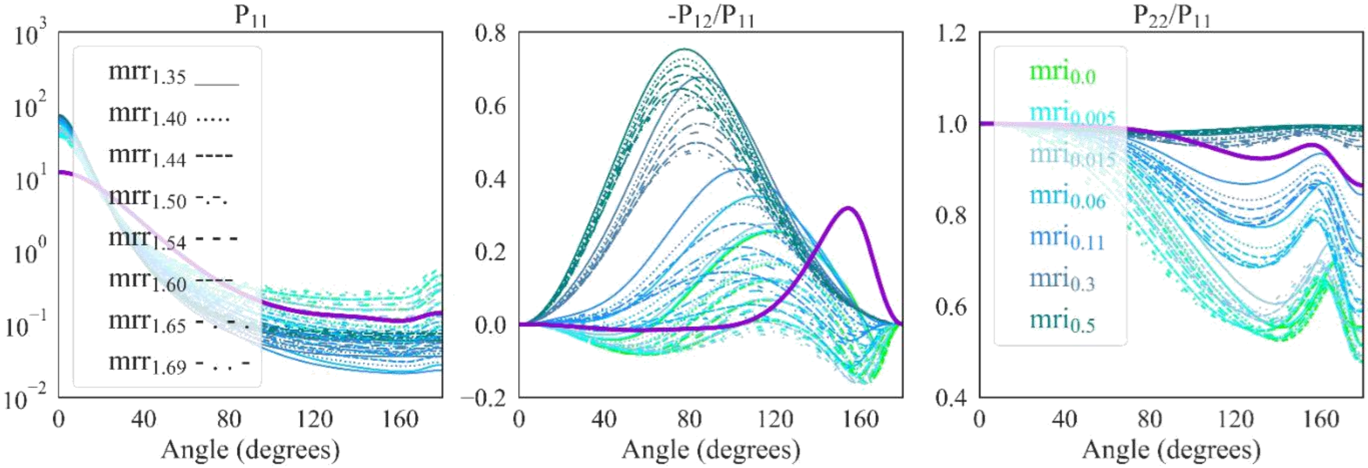

Figure S50. Same as Fig. S42, with the calculations using the AERONET non-spherical model, performed for mono-modal log-normal size distributions with mean geometric radius r_g = 1.0 μm.

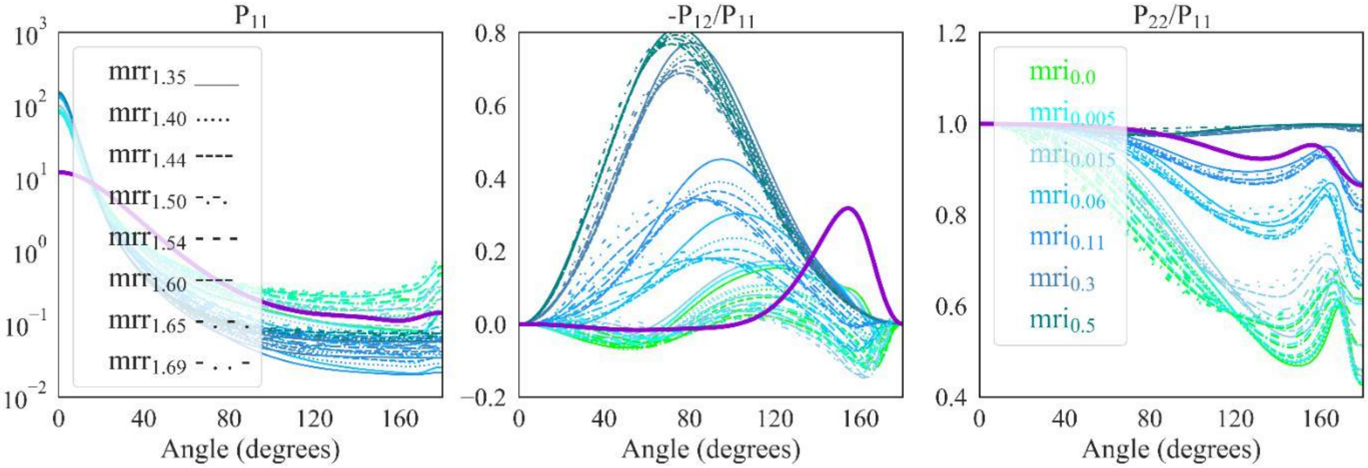

Figure S51. Same as Fig. S42, with the calculations using the AERONET non-spherical model, performed for mono-modal log-normal size distributions with mean geometric radius r_g = 1.5 μm.

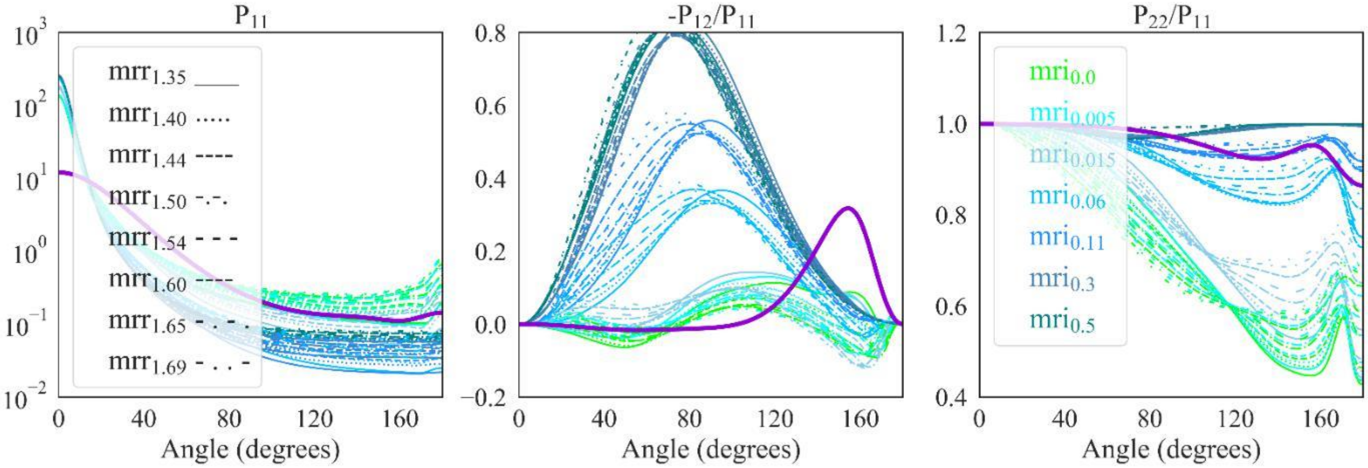

Figure S52. Same as Fig. S42, with the calculations using the AERONET non-spherical model, performed for mono-modal log-normal size distributions with mean geometric radius r_g = 2.0 μm.

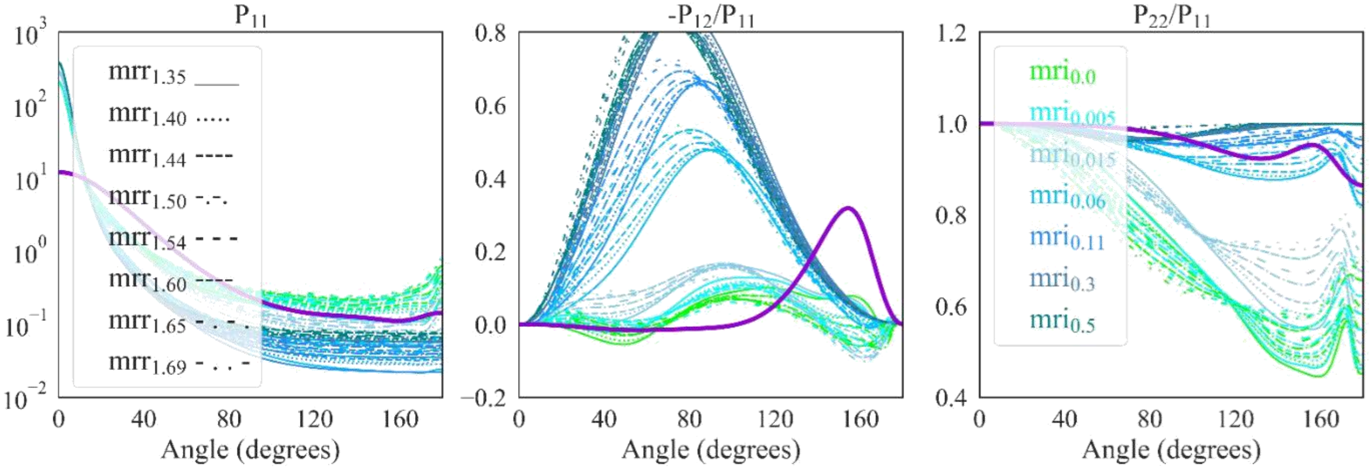

Figure S53. Same as Fig. S42, with the calculations using the AERONET non-spherical model, performed for mono-modal log-normal size distributions with mean geometric radius r_g = 2.5 μm.

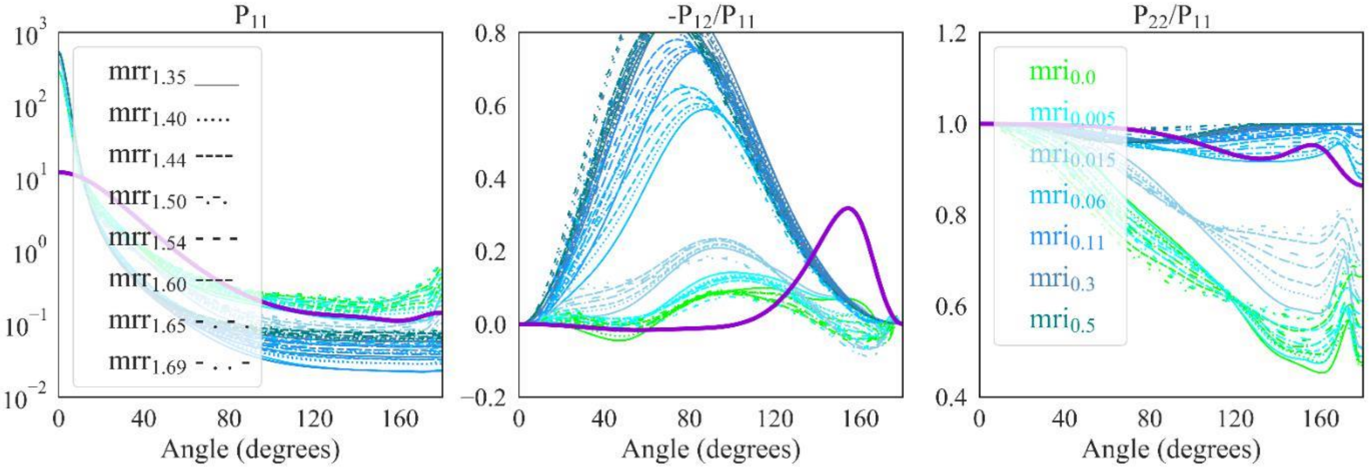

Figure S54. Same as Fig. S42, with the calculations using the AERONET non-spherical model, performed for mono-modal log-normal size distributions with mean geometric radius r_g = 3.0 μm.

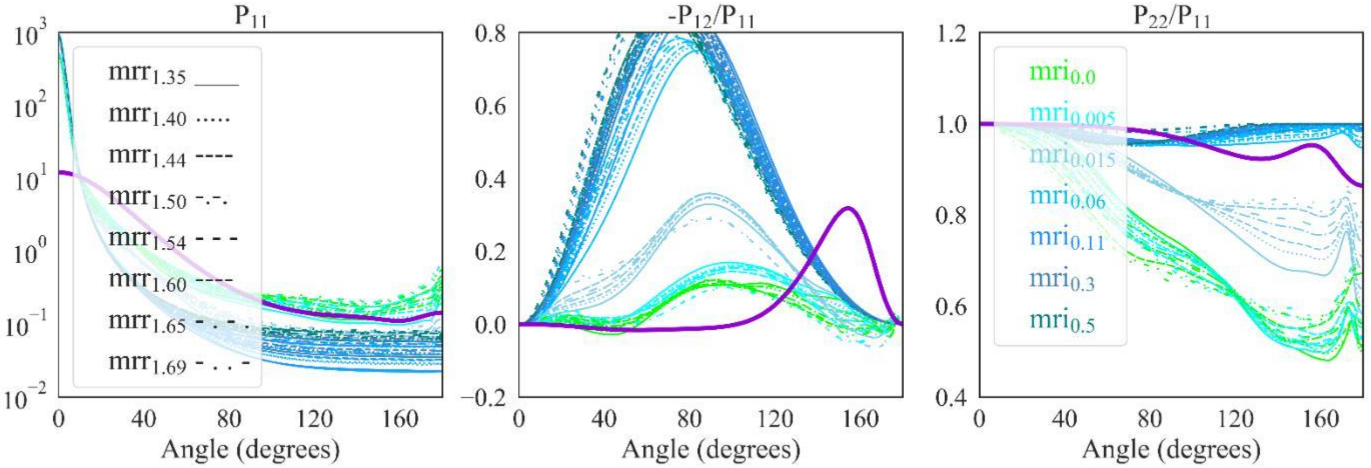

Figure S55. Same as Fig. S42, with the calculations using the AERONET non-spherical model, performed for mono-modal log-normal size distributions with mean geometric radius r_g = 4.0 μm.

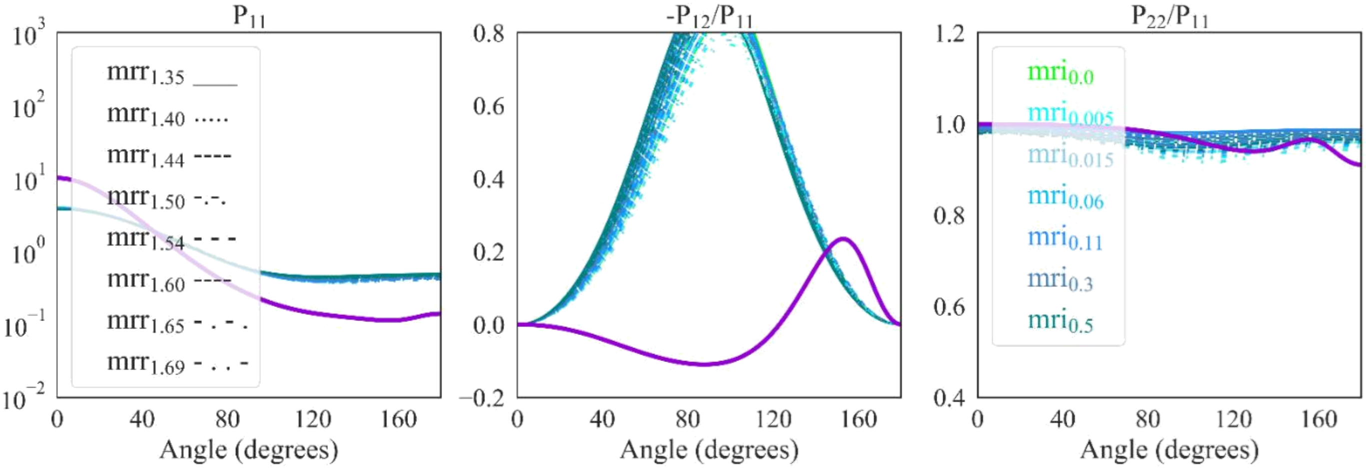

Figure S56. The elements of the scattering matrix at λ = 1020 nm. Left: P11 (phase function), middle: -P12/P11 (degree of linear polarization), right: P22/P11. Purple lines in the plots: calculations considering the near-spherical particle properties derived for the stratospheric smoke particles from the Canadian fires, with mean axial ratio ε_s= 1.3, mono-modal, log-normal size distribution with mean geometric radius r_g = 0.25 μm, mean geometric standard deviation σ_g = 0.4, and complex refractive index m = 1.55 – i0.03. Blue lines in the plots: calculations using the AERONET non-spherical model, monomodal, log-normal size distributions with r_g = 0.1 μm and refractive indices of mrr = 1.35, 1.40, 1.44, 1.50, 1.54, 1.60, 1.65, 1.69 for the real part (different line styles in the plot) and mri = 0.0, 0.005, 0.015, 0.06, 0.11, 0.3, 0.5 for the imaginary part (different line colors in the plot).

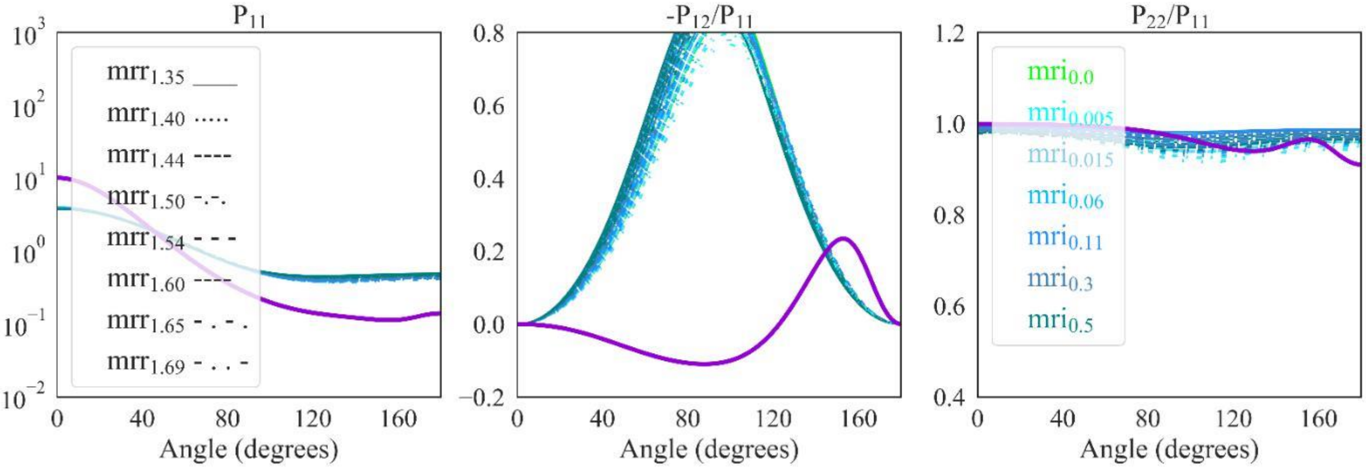

Figure S57. Same as Fig. S56, with the calculations using the AERONET non-spherical model, performed for mono-modal log-normal size distributions with mean geometric radius r_g = 0.15 μm.

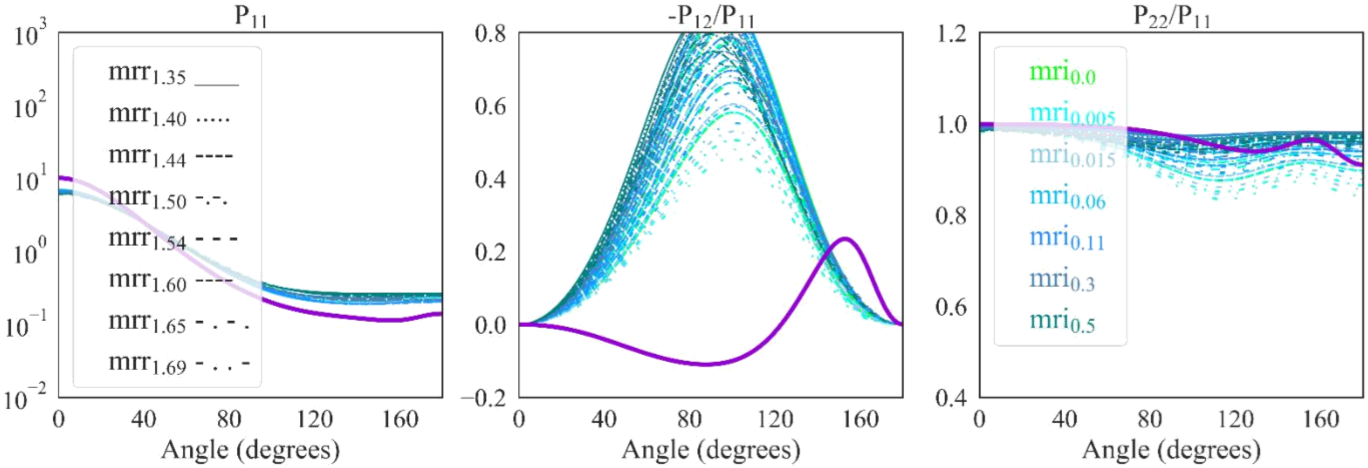

Figure S58. Same as Fig. S56, with the calculations using the AERONET non-spherical model, performed for mono-modal log-normal size distributions with mean geometric radius r_g = 0.2 μm.

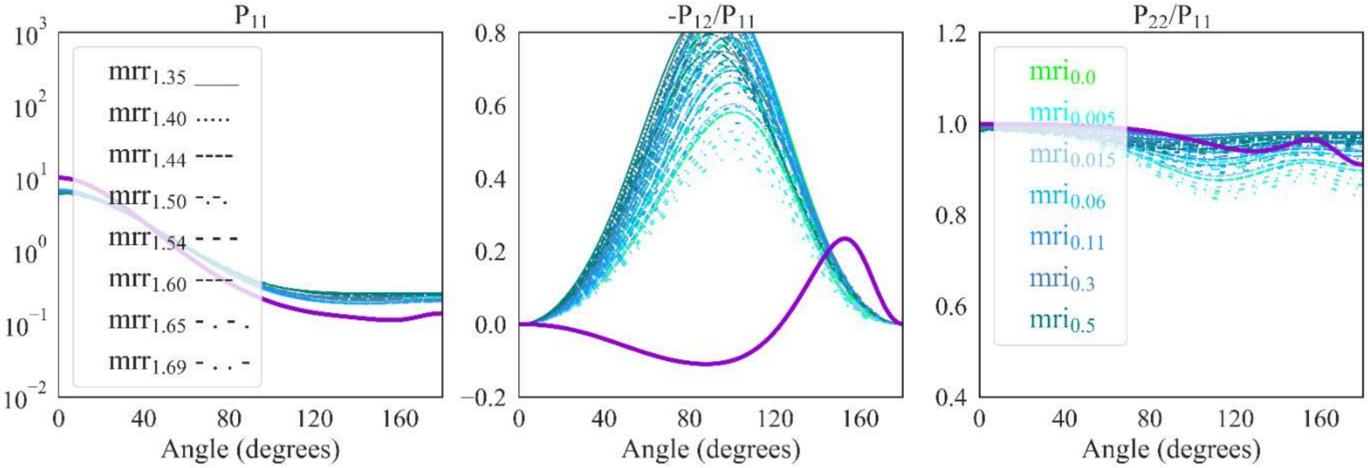

Figure S59. Same as Fig. S56, with the calculations using the AERONET non-spherical model, performed for mono-modal log-normal size distributions with mean geometric radius r_g = 0.25 μm.

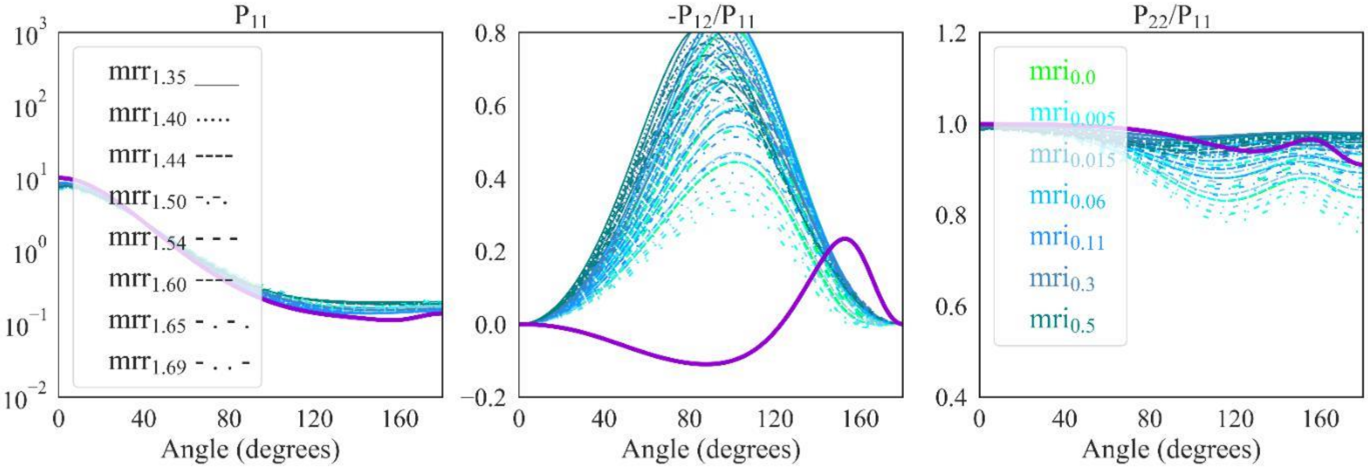

Figure S60. Same as Fig. S56, with the calculations using the AERONET non-spherical model, performed for mono-modal log-normal size distributions with mean geometric radius r_g = 0.3 μm.

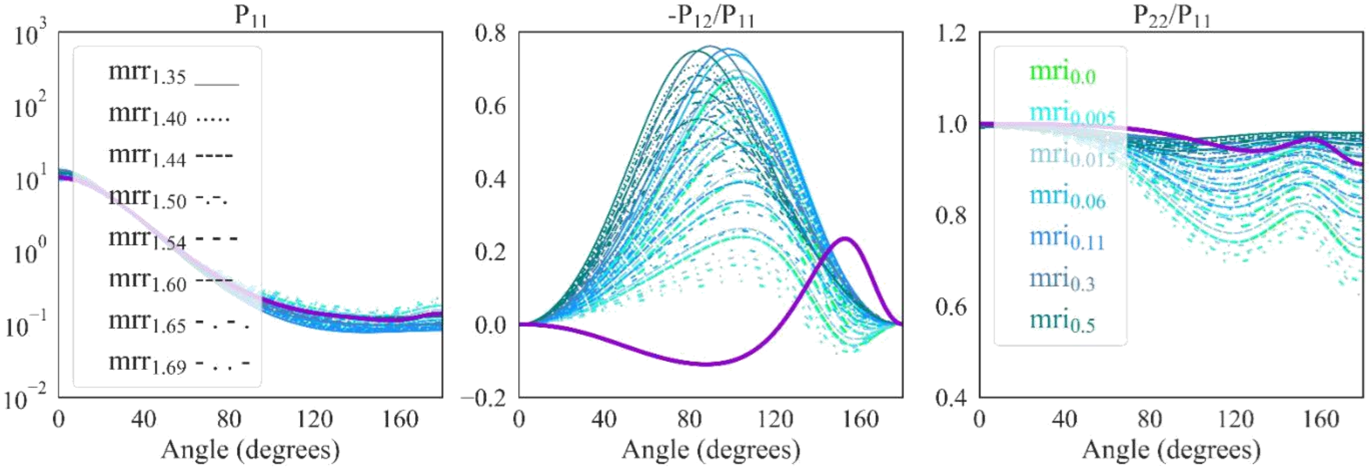

Figure S61. Same as Fig. S56, with the calculations using the AERONET non-spherical model, performed for mono-modal log-normal size distributions with mean geometric radius r_g = 0.4 μm.

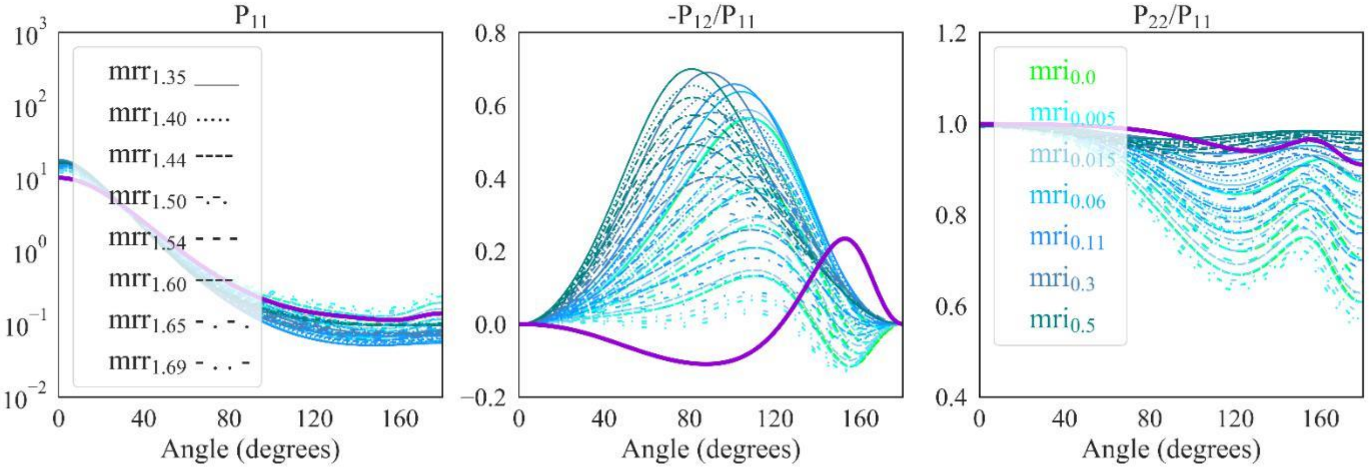

Figure S62. Same as Fig. S56, with the calculations using the AERONET non-spherical model, performed for mono-modal log-normal size distributions with mean geometric radius r_g = 0.5 μm.

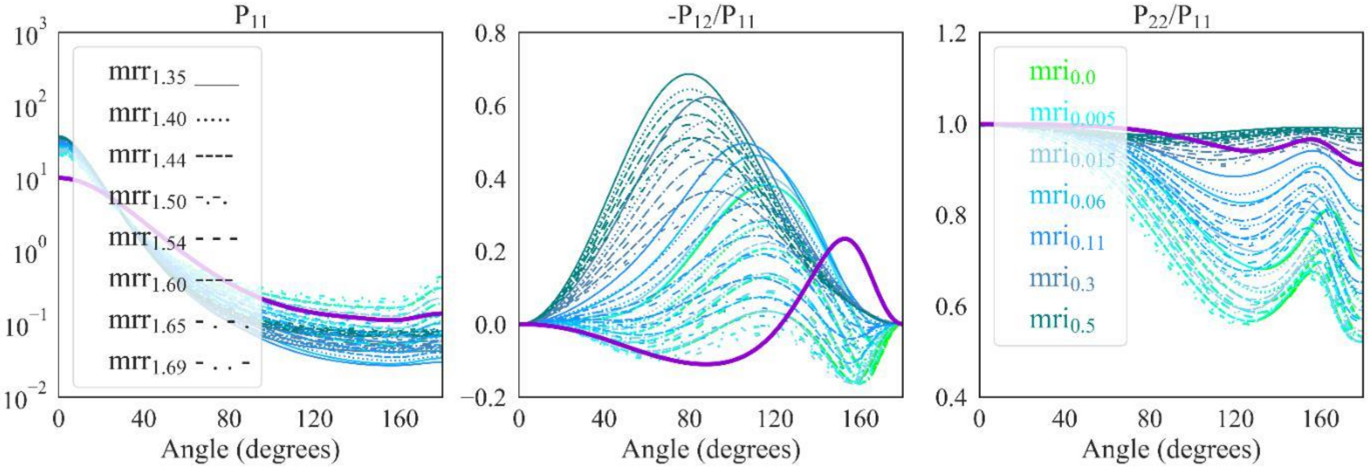

Figure S63. Same as Fig. S56, with the calculations using the AERONET non-spherical model, performed for mono-modal log-normal size distributions with mean geometric radius r_g = 0.8 μm.

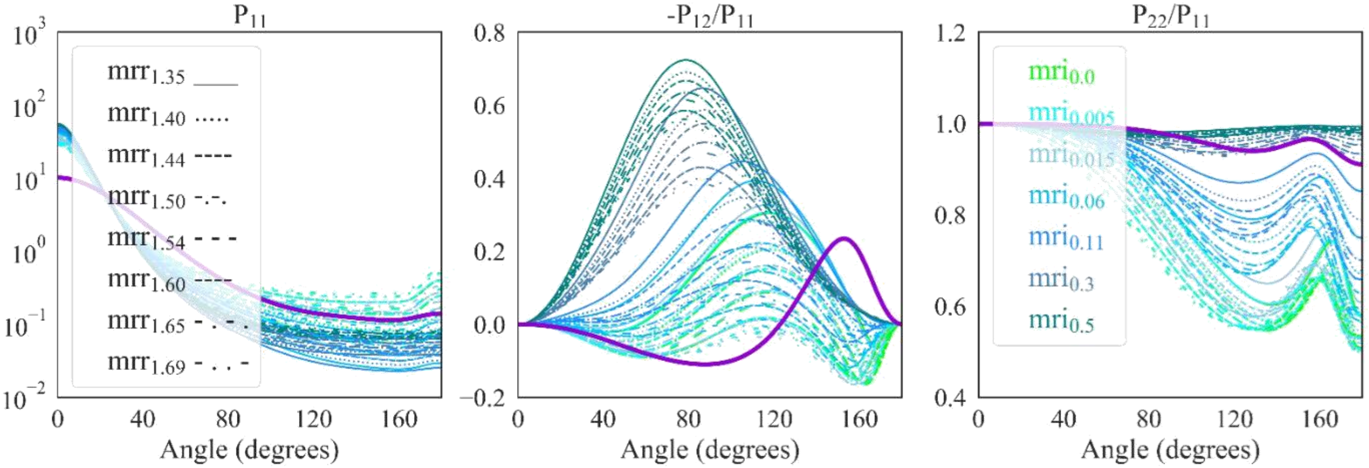

Figure S64. Same as Fig. S56, with the calculations using the AERONET non-spherical model, performed for mono-modal log-normal size distributions with mean geometric radius r_g = 1.0 μm.

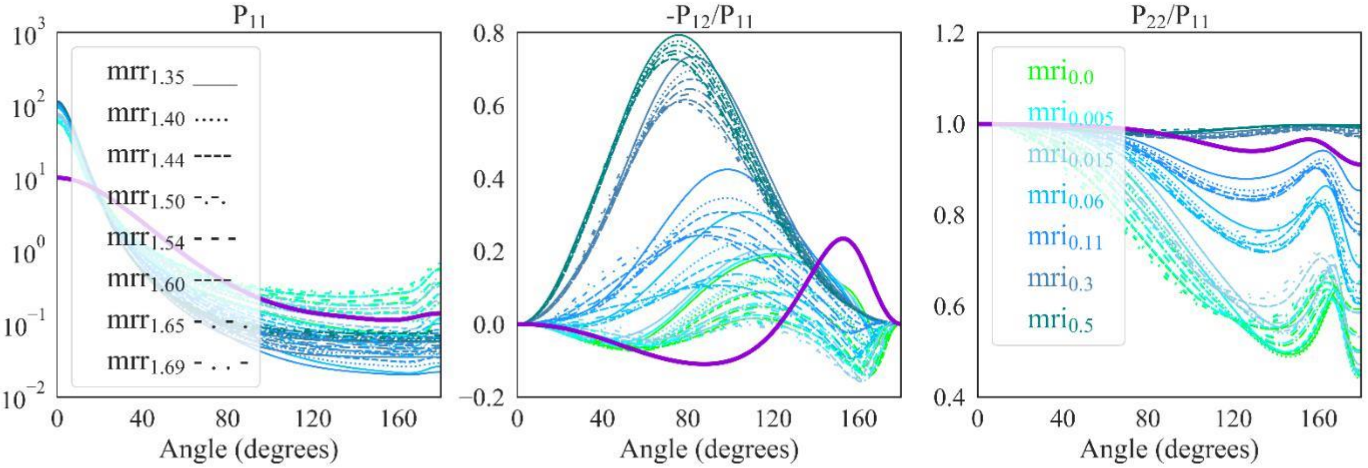

Figure S65. Same as Fig. S56, with the calculations using the AERONET non-spherical model, performed for mono-modal log-normal size distributions with mean geometric radius r_g = 1.5 μm.

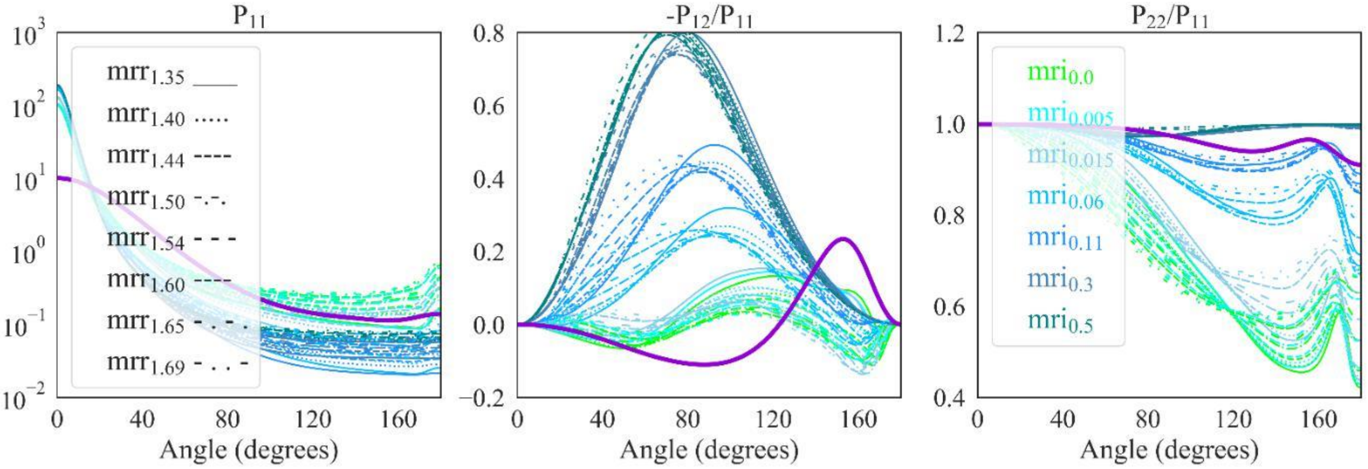

Figure S66. Same as Fig. S56, with the calculations using the AERONET non-spherical model, performed for mono-modal log-normal size distributions with mean geometric radius r_g = 2.0 μm.

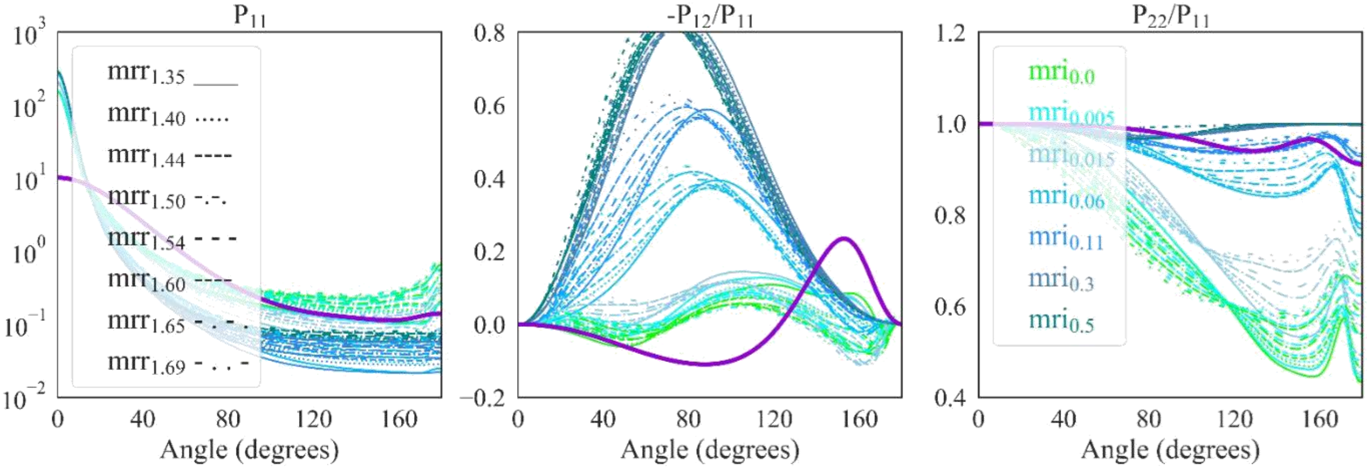

Figure S67. Same as Fig. S56, with the calculations using the AERONET non-spherical model, performed for mono-modal log-normal size distributions with mean geometric radius r_g = 2.5 μm.

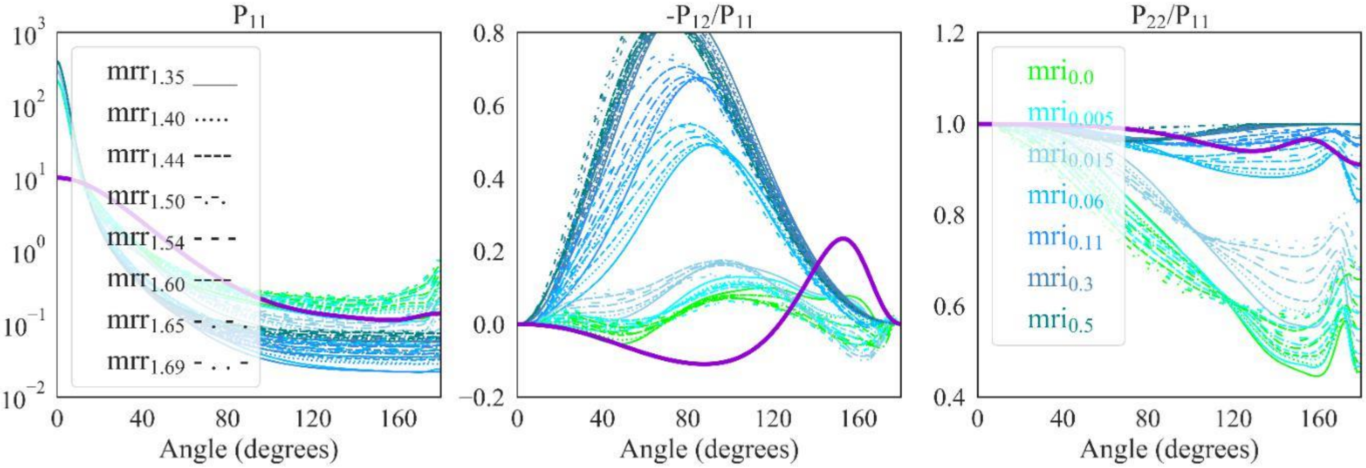

Figure S68. Same as Fig. S56, with the calculations using the AERONET non-spherical model, performed for mono-modal log-normal size distributions with mean geometric radius r_g = 3.0 μm.

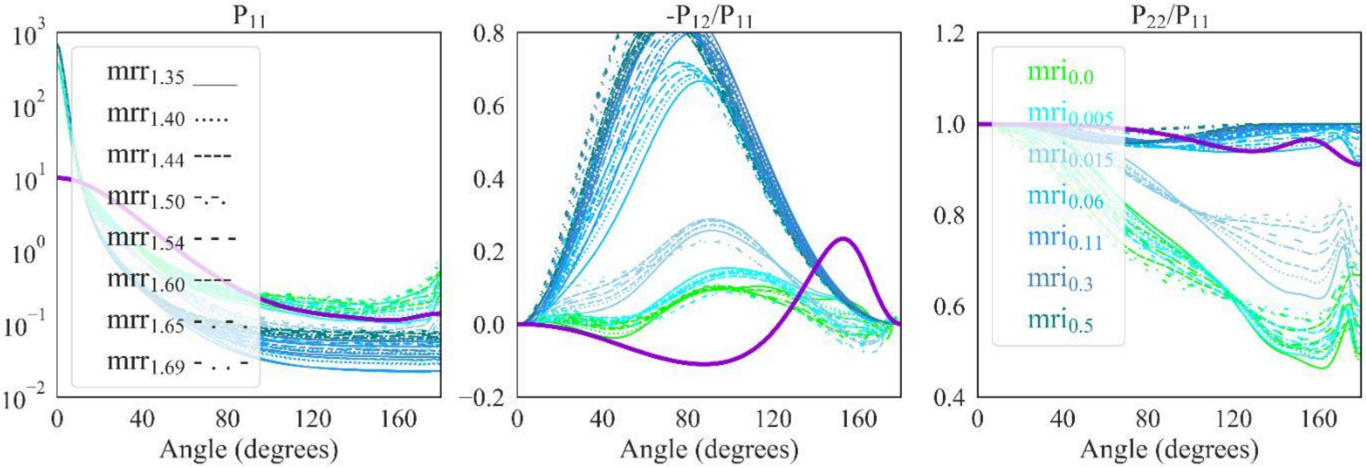

Figure S69. Same as Fig. S56, with the calculations using the AERONET non-spherical model, performed for mono-modal log-normal size distributions with mean geometric radius r_g = 4.0 μm.